Suche nach elektroschwacher Erzeugung einzelner Top-Quarks mit dem CDF-Experiment in Proton-Antiproton-Kollisionen bei 1.96 TeV Schwerpunktsenergie

Thorsten Walter

Zur Erlangung des akademischen Grades eines
DOKTORS DER NATURWISSENSCHAFTEN
von der Fakultät für Physik der
Universität Karlsruhe(TH)

genehmigte

Dissertation

von

Dipl. Phys. Thorsten Walter
aus Bad Bergzabern

Tag der mündlichen Prüfung: 17. Juni 2005

Referent: Prof. Dr. Th. Müller, Institut für Experimentelle Kernphysik

Korreferent: Prof. Dr. M. Feindt, Institut für Experimentelle Kernphysik

Zusammenfassung

Das CDF Experiment befindet sich am Tevatron Proton-Antiproton Ring in der Nähe von Chicago. Die erreichte Schwerpunktsenergie in Proton-Antiproton Kollisionen beträgt 1.96 Teraelektronenvolt. In dieser Arbeit wurde ein Datensatz, der einer integrierten Luminosität von 162 pb^{-1} entspricht, verwendet. Dieser Datensatz wurde von 2002 bis September 2003 gesammelt. Im sogenannten Run I des Tevatronbeschleunigers wurde das Top-Quark entdeckt, welches am Tevatron hauptsächlich durch die Starke Wechselwirkung paarweise erzeugt wird. Neben dieser Top-Antitop-Quark Paarproduktion sagt das Standardmodell der Teilchenphysik auch die elektroschwache Produktion einzelner Top-Quarks voraus. Für diesen Produktionsmechanismus gibt es noch keine experimentelle Evidenz. Am Tevatron dominieren zwei Produktionskanäle für die Produktion einzelner Top-Quarks, (1) der t-Kanal oder die W-gluon Fusion und (2) der s-Kanal oder die W^* Produktion. Der Wirkungsquerschnitt für diese elektroschwache Top-Quark Produktionskanäle ist proportional zum Quadrat des CKM Matrixelements $|V_{tb}|$. Die Messung des Wirkungsquerschnittes erlaubt somit im Prinzip eine direkte Messung von $|V_{tb}|$ ohne weitere Annahmen bezüglich der Zahl der Quark-Familien.

Die verwendete integrierte Luminosität von 162 pb^{-1} reicht leider nicht aus um den Wirkungsquerschnitt für die Erzeugung einzelner Top-Quarks zu messen, beziehungsweise experimentelle Evidenz für diesen Produktionskanal zu finden. In dieser Arbeit werden deshalb obere Grenzen für die Produktionswirkungsquerschnitte bestimmt. Diese oberen Grenzen für die Wirkungsquerschnitte testen Modelle jenseits des Standardmodells, die eine erhöhte Produktionsrate voraussagen. In dieser Arbeit werden Ereignisse selektiert, welche durch die Signatur von einem W Boson und 2 Kalorimeter-Jets charakterisiert sind. In dieser Analyse werden nur die Zerfallsmoden $W \to e\nu_e$ und $W \to \mu\nu_\mu$ betrachtet. Um die Untergründe zum Top-Quark Signal zu unterdrücken und somit eine Signalanreicherung zu erreichen, wird zusätzlich mindestens ein identifizierter Bottom-Jet verlangt. Um obere Grenzen für den s- und den t-Kanal Produktionsmechanisum zu bestimmen, wird der vorselektierte Datensatz in zwei Teildatensätze gemäss der Zahl der identifizierten Bottom-Jets aufgeteilt (genau ein Bottom-Jet oder genau zwei Bottom-Jets). Für die t-Kanal Produktion erwartet man im Mittel einen identifizierbaren Bottom-Jet, wohingegen in s-Kanal Ereignissen zwei nachweisbare Bottom-Jets erwartet werden.

Im Folgenden werden zwei separate Suchen nach "Single Top" Produktion durchgeführt. Für die erste Suche wird im Wesentlichen die invariante Masse aus Bottom-Jet, Elekton- bzw. Myon-Kandidat und dem Neutrino-Kandidaten gebildet und verlangt, dass diese Größe in einem Fenster von ± 35 GeV/c^2 um die Top-Quarkmasse liegt. Dadurch kann ein signifikanter Anteil der verbliebenen Untergrundereignisse aus den Teildatensätzen entfernt werden. Im Datensatz mit genau einem identifizierten Bottom-Jet wird zusätzlich noch gefordert, dass der Transversalimpuls eines Jets 30 GeV/c übersteigt. Um nun obere Grenzen für den Wirkungsquerschnitt zu berechnen, wird eine gebinnte Likelihood Funktion benutzt, welche aus zwei Faktoren besteht: (1) einer Likelihood Funktion basierend auf der Verteilung von $Q \cdot \eta$ für den Datensatz mit genau einem Bottom-Jet und (2) der Gesamtzahl der beobachteten Ereignisse mit genau zwei identifizierten Bottom-Jets. Hierbei ist Q die Landung des identifizierten Leptons aus dem W Boson Zerfall in Einheiten der Elektronenladung e und η ist die Pseudorapidität des nicht-Bottom-Jets. Zur Bestimmung der oberen Grenzen der Wirkungsquerschnitte für s- bzw. t-Kanal Single Top-Quark Produktion wird die Likelihood Funktion berechnet. Systematische Unsicherheiten werden durch zusätzliche Parameter in die Likelihood-Funktion eingebunden. Diese Parameter modellieren den Effekt der jeweiligen Fehlerquelle. Diese Unsicherheiten werden schliesslich ausintegriert, so dass die Likelihood-Funktion letztendlich nur vom Signalwirkungsquerschnitt abhängt. Diese Funktion wird anschliessend bis zum 95% Konfidenzniveau integriert und somit die obere Grenze auf den Wirkungsquerschnitt bestimmt. Für die Bestimmung der oberen Grenze für die t-Kanal Produktion wurde der s-Kanal im Rahmen der Unsicherheiten auf die Standardmodell Vorhersage eingeschränkt und umgekehrt. Die so gefundenen oberen Grenzen für die elektroschwache Single Top-Quark Produktion sind 13.6 pb für die s-Kanal Produktion und 10.1 pb für den t-Kanal. Dies sind die bisher niedrigsten veröffentlichten oberen Grenzen für diese Produktionskanäle.

Um nun den Produktionsmechanismus der elektroschwachen Single Top-Quark Produktion entdecken zu können, ist es essentiell, die Untergründe zu reduzieren. Hierfür ist es notwendig eine hohe Signifikanz $\rho = N_{\text{sig}}/\sqrt{N_{\text{back}}}$ zu erreichen. N_{sig} bezeichnet die Zahl der Signalereignisse und N_{back} die Zahl der erwarteten Untergrundereignisse. In einer zweiten Analyse wurde eine iterative Diskriminanzanalyse verwendet um die Signifikanz zu erhöhen. Der für die Diskriminanzanalyse verwendete Algorithmus ist eine quadratische Erweiterung einer Fisher Diskriminanten welcher zweimalig angewendet wird. Dieser Algorithmus wird auf den Subdatensatz, der durch genau einen identifizierten Bottom-Jet definiert ist, angewendet. Mithilfe dieser multivariaten Methode gelingt es die Signifikanz ρ für die erwarteten t-Kanalereignisse um 34% gegenüber der schnittbasierten Analyse zu steigern. Trotz dieser Steigerung verbessern sich die oberen Grenzen auf den s- und t-Kanal Wirkungsquerschnitt nicht. Für den s-Kanal ergibt sich die obere Grenze zu 17.2 pb und 11.0 pb für den t-Kanal. Diese Grenzen wurden analog zur schnittbasierten Suche bestimmt, allerdings wird

in dieser Analyse die resultierende Diskriminante in acht Bins für die Likelihood-Funktion verwendet. Die Anwendung dieses Algorithmus verringert die zur Entdeckung benötigte Luminosität drastisch. Kombiniert man die s- and t-Kanal Ereignisse, so ist eine 3σ Evidenz mit einer integrierten Luminosität von $1.8\,\mathrm{fb}^{-1}$ erreichbar. Legt man hingegen die erreichte Signifikanz der schnittbasierten Suche zu Grunde, so erwartet man hier eine integrierten Luminosität $3.0\,\mathrm{fb}^{-1}$ für eine 3σ Evidenz.

Search for Electroweak Single Top Quark Production with CDF in Proton-Antiproton Collisions at $\sqrt{s} = 1.96$ TeV

Thorsten Walter

Zur Erlangung des akademischen Grades eines
DOKTORS DER NATURWISSENSCHAFTEN
von der Fakultät für Physik der
Universität Karlsruhe(TH)

genehmigte

Dissertation

von

Dipl. Phys. Thorsten Walter
aus Bad Bergzabern

Tag der mündlichen Prüfung: 17. Juni 2005

Referent: Prof. Dr. Th. Müller, Institut für Experimentelle Kernphysik

Korreferent: Prof. Dr. M. Feindt, Institut für Experimentelle Kernphysik

Preface

The CDF experiment is located at the Tevatron proton-antiproton collider in the vicinity of Chicago. The center of mass energy of the proton-antiproton collisions in Run II is 1.96 TeV. A data set corresponding to an integrated luminosity of 162 pb^{-1} was used in this thesis. The data was collected in the period starting from early 2002 until September 2003.

One of the major achievements in Tevatron Run I was the discovery of the top quark. The top quark is dominantly produced in top-antitop quark pairs by the strong interaction. Within the Standard Model of elementary particle physics, top quarks are also predicted to be produced singly involving the electroweak interaction. This electroweak production mode offers the opportunity to measure the Cabbibo-Kobayashi-Maskawa (CKM) matrix element $|V_{tb}|$ directly since the production cross section is proportional to $|V_{tb}|^2$. Assuming three quark generation the unitary of the CKM Matrix implies $|V_{tb}| \approx 1$. However, if their are more than three quark generations, $|V_{tb}|$ could in principle be any positive number smaller than one. A direct measurement is in principle independent on the assumption of three generations and can thus probe the unitary of the CKM matrix. Apart from that single top quark production is a significant background process to the production of a potential Higgs boson in the mass range of 90 GeV/c^2 to 130 GeV/c^2 produced in the WH channel.

Two processes significantly contribute to single top production at the Tevatron, (1) the s-channel or W^* process and (2) the t-channel or $W-$gluon fusion process. Single top quark production has not yet been observed and the luminosity collected in Run II is not yet sufficient to measure the production cross section. Therefore, in this analysis upper limits on the production cross sections for the s- and t-channel processes are calculated. These limits probe models that predict enhanced single top quark production due to physics beyond the Standard Model [1].

After a brief introduction to the phenomenology of electroweak single top quark production, the CDF experiment is described. In chapter three the reconstruction algorithms used in this analysis are introduced. In the following chapter the event yield for single top quark production is calculated with an improved signal modeling using the MadEvent Monte Carlo program. Only the decays $W \to e\nu_e$ and $W \to \mu\nu_\mu$ are considered. This analysis focuses on events

where exactly two jets have been identified. At least one of the two jets has to be originating from a bottom quark. In chapter five the expected number of background events originating from top-antitop pair production and processes where no top quarks are involved are presented. In the following chapter the analysis techniques used in this analysis are presented. To extract the single top contents of the data sample a likelihood function is used. To increase to s-channel sensitivity the sample is divided in the exactly one identified bottom jet sample, and a subsample where two bottom jets have been identified. To increase the significance of the single top signal in a second approach an iterated discriminant analysis is used. In the seventh chapter a cut based single top search will be presented. Limits on s- and t-channel production will be calculated based on the data set of 162 pb^{-1}. In the following chapter a separate single top search using an iterated discriminant will be presented. Here the significance of the t-channel signal was increased by the use of eight observables. These observables will be introduced and limits will be calculated using this technique. Perspectives for future analyses with an increased amount of available integrated luminosity are presented before the final conclusion is drawn.

Contents

List of Figures

List of Tables

Chapter 1

Electroweak Single Top Quark Production within the Standard Model

The Standard Model of Elementary Particles Physics describes the fundamental particles of matter and their interactions except gravity. The Standard Model provides a very elegant theoretical framework using quantum fields to describe the interactions[2, 3, 4].

The Standard Model has been very successful in predicting a vast variety of properties of particles and interactions in the energy regime explored by high energy colliders up to now. Single Top Production is predicted within this model, but is not yet discovered. In this chapter a summary of the Standard Model which focuses on electroweak Single Top Quark Production will be presented.

1.1 The Standard Model of Elementary Particle Physics

All matter in the Standard Model is composed of particles with spin $s = \frac{1}{2}$, the leptons and quarks. Up to now there are six different quark flavors known, up(u), down(d), strange(s), charm(c), bottom(b) and top(t). To describe elementary particles, quantum numbers are used, e.g. the electromagnetic charge q or the spin s. The quarks have an additional quantum number, the color, which can be of three types. Since color is not seen in nature, the quarks must be confined into colorless particles, which are classified into baryons and mesons. The baryons are made of three quarks, as for instance the proton, $p \sim uud$. The mesons are made of a quark-antiquark pair like pions, $\pi^+ \sim u\bar{d}$. There are also six particles which do not have strong interaction, the leptons. These are the electron, the muon and the tau and the corresponding neutral neutrinos. All fundamental particles

are ordered in families or generations based on weak interactions. The left handed partners form isospin doublets. Table 1.1 displays the three generations of fundamental particles.

name	symbol	el. charge	mass
up	u	$\frac{2}{3}$	$(1.5-4)$ MeV
down	d	$-\frac{1}{3}$	$(4-8)$ MeV
electron	e	-1	511 keV
e-neutrino	ν_e	0	< 3 eV
charm	c	$\frac{2}{3}$	$(1.15-1.35)$ GeV
strange	s	$-\frac{1}{3}$	$(80-130)$ MeV
muon	μ	-1	106 MeV
μ-neutrino	ν_μ	0	< 190 keV
top	t	$\frac{2}{3}$	174.3 ± 5.1 GeV
bottom	b	$-\frac{1}{3}$	$(4.1-4.4)$ GeV
tau	τ	-1	1.777 GeV
τ-neutrino	ν_τ	0	< 18.2 MeV

Table 1.1: The fundamental spin-$\frac{1}{2}$ particles.The electric charge is in units of the electron charge [5].

Three of the four fundamental forces, the electromagnetic force, the weak and the strong force are described by the Standard Model. Gravitation is not yet included in this concept and described by the Theory of General Relativity. The three forces described by the Standard Model are transmitted by specific particles. As the theories of the forces are gauge theories, the transmitting particles are called gauge bosons. Table 1.2 summarizes the properties of the gauge bosons for each force. In a gauge theory the Lagrange function, that describes a physical system, is invariant under local gauge transformations. According to the Noether theorem such an invariance implies a conserved current, to which the charges of the force correspond. Only particles that carry the charge of a force can interact via this force. The charges of the weak force are called weak hypercharges, and the color charges are assigned to the strong force.

Two charged particles interact by the emission and reabsorption of a gauge boson. Such a process is described by a Feynman diagram. The diagram gives a visualization of the physical process in the momentum space. The Feynman rules provide a prescription of how to translate the diagram into a formula to calculate the transition amplitude $\mathcal{M}$. From this the cross section of the process

Force	boson name	symbol	el. charge	spin	mass
Strong	gluon	g	0	1	0
Electromagnetic	photon	γ	0	1	0
Weak	W-boson	W^+	+1	1	80.425 ± 0.10
		W^-	-1	1	80.425 ± 0.10
	Z-boson	Z^0	0	1	91.188 ± 0.007

Table 1.2: Properties of the gauge bosons. The electric charge is in units of the electron charge, the mass is in units of GeV/c^2 [6].

can be derived by integrating over all initial and final states, the phase space. The diagram for electron-electron scattering via the exchange of a virtual photon is shown in figure 1.1.

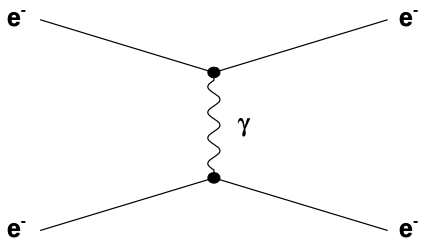

Figure 1.1: Feynman diagram for electron-electron scattering. At the left hand side are the two incoming electrons. At the right hand side of the diagram are the final state electrons. The coupling of the electrons to the photon depends on the vertices, shown in the diagram by the dots. The force is transmitted by the photon, which is described by its propagator.

An important factor concerning electroweak processes and quarks is the Cabibbo-Kobayashi-Maskawa mixing matrix [7, 8]. Experimental evidence was found that the mass eigenstates are not equivalent to the flavor eigenstates. By convention the mass eigenstates s, d and the flavor eigenstates s', d', which participate in the weak interaction, are connected according to:

$$\begin{pmatrix} d \\ s \end{pmatrix} = \begin{pmatrix} \cos\theta_C & \sin\theta_C \\ -\sin\theta_C & \cos\theta_C \end{pmatrix} \begin{pmatrix} d' \\ s' \end{pmatrix}$$

The so-called Cabibbo-angle θ_C is about 13^o. Considering three generations it leads to the Cabibbo-Kobayashi-Maskawa mixing matrix (CKM-Matrix).

$$\begin{pmatrix} d' \\ s' \\ b' \end{pmatrix} = \begin{pmatrix} V_{ud} & V_{us} & V_{ub} \\ V_{cd} & V_{cs} & V_{cb} \\ V_{td} & V_{ts} & V_{tb} \end{pmatrix} \begin{pmatrix} d \\ s \\ b \end{pmatrix}$$

The single elements $V_{q_1q_2}$ of the matrix have to be determined experimentally and are proportional to the coupling of two quarks q_1, q_2 to a W-boson, see figure 1.2. The 90% confidence limits on the magnitude of the elements of the complete matrix are [6]:

$$\begin{pmatrix} (0.9742 & to & 0.9757) & (0.219 & to & 0.226) & (0.002 & to & 0.005) \\ (0.219 & to & 0.225) & (0.9734 & to & 0.9749) & (0.037 & to & 0.043) \\ (0.004 & to & 0.014) & (0.035 & to & 0.043) & (0.9990 & to & 0.9993) \end{pmatrix}$$

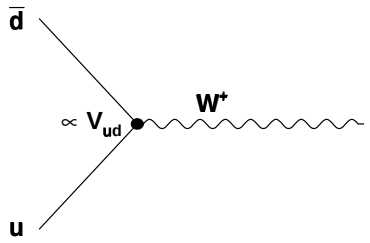

Figure 1.2: Diagram for the coupling of an up and a down quark to a W-boson

With the Lagrangian of the electroweak theory the masses of the quarks and the gauge bosons cannot be explained. As the gauge fields have to be invariant under local or global transformations, the local gauge invariance forces the gauge bosons to be massless. Any mass term in the Lagrangian would destroy the local gauge invariance. The solution for this dilemma is to introduce an additional scalar field, the Higgs-field [9]. With this method the Lagrangian remains invariant under gauge transformation, but the ground state is interacting with this background field, which generates the masses of the gauge bosons. The fermions get their masses also via interaction with the Higgs-field, the coupling is called Yukawa-coupling.

1.2 Top quark production in the Standard Model

Within the Standard Model the dominant production process for top quarks at the Tevatron Collider is the top pair production via the strong interaction. This production mode was discovered by the Tevatron experiments CDF and D0 in 1995 [10, 11] . Within the Standard Model top quarks are predicted to be produced singly via the electroweak interactions. In such interactions a $Wt\bar{b}$ vertex is involved in the production and in the decay of the top quark. This process has not yet been observed.

1.2.1 Top Quark Pair Production

In this section the top quark pair production in proton-antiproton collisions will be briefly described. The leading order perturbation theory Feynman graphs of $t\bar{t}$ production are given in figure 1.3. In $p\bar{p}$ collisions at the Tevatron two

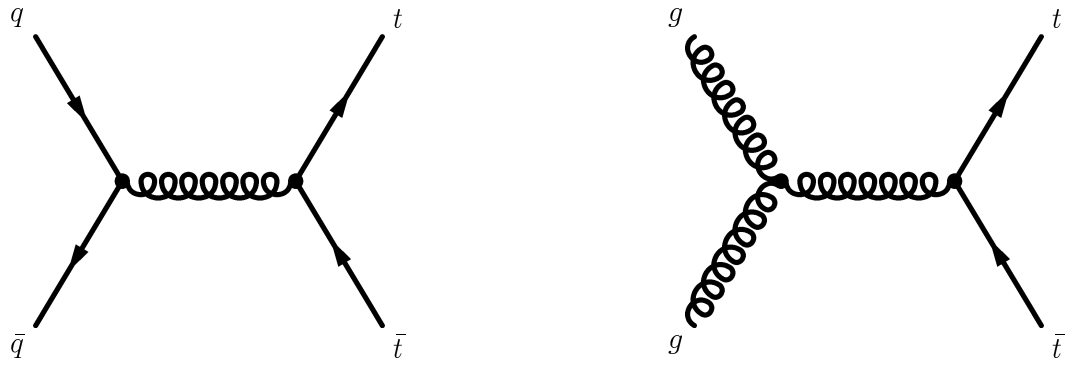

Figure 1.3: The leading order $t\bar{t}$ production Feynman diagrams

production mechanisms are dominant. One is the production via the quark antiquark annihilation, the other is the gluon fusion process. In next-to leading order calculations the annihilation contributes about 85% and the gluon fusion about 15% to the $t\bar{t}$ cross section which is predicted to be about 6.7 pb [13, 14] at the Tevatron assuming a top quark mass of 175 GeV/c^2. The uncertainty of this prediction is about 15% due to the chosen set of parton distribution function parameterizations of the proton (PDF) and the uncertainty in choosing the interaction scale Q^2 for $t\bar{t}$ events.

1.2.2 Single Top Quark Production

While the main part of top quarks at the Tevatron with $\sqrt{s} = 1.98$ TeV are produced via top-pair production, there are also three significant electroweak production modes for single top quarks.

These production modes differ in the virtuality Q^2 of the involved W boson. Q^2 denotes here the negative square of the W boson four-momentum q. The production modes ordered by their predicted cross section at the Tevatron are:

- **t-channel or W-gluon Fusion**
- **s-channel or W* production**
- **associated production**

The first two production modes are labeled by the relevant Mandelstam variables t and s involved in the transition matrix elements $\mathcal{M}$. In t-channel production the W boson is spacelike ($-Q^2 = q^2 = t < 0$), whereas in s-channel production it is timelike ($-Q^2 = q^2 = s \geq (m_t + m_b)^2 > 0$). The third production mode does not fit in this name scheme. Here an on-shell (or a almost on-shell) W boson is produced in conjunction with the top quark. The production cross section of this process is quite small at the Tevatron.
There are also other production modes involving $Wt\bar{d}$ or $Wt\bar{s}-$vertices, but these processes are strongly suppressed by tiny CKM matrix elements. The contribution of such processes to the total cross section is about 1% and thus negligible at the Tevatron.

Protons and antiprotons colliding at the Tevatron are composite particles. The proton is made of three valence quarks (uud), held together via an exchange of virtual gluons. These gluons can split into an quark-antiquark pair, the seaquarks. This leads to the situation, that the momentum of the proton is shared by all three valence quarks, sea-quarks and gluons. The fraction of the momentum, carried by each quark and gluon, is described by parton distribution functions [15]. Figure 1.4 shows the CTEQ5M parton distribution for the scale $Q^2 = (200\ \text{GeV})^2$. These parton distribution functions (PDF) are necessary since the matrix elements are based on partons as initial states. Therefore, these PDF have to be folded with the partonic cross sections to calculate the measurable cross section in $p\bar{p}$ collisions.

The W-gluon fusion process or t-channel production is predicted by the Standard Model to possess a cross section of 1.980 ± 0.12(NLOscale) pb at the Tevatron [16]. The uncertainty due to the top quark mass is about 10%, the typical uncertainty due to the choice of the PDF parametrization is 5%. In this analysis a total uncertainty of 13% is assumed [17]. The leading and an example of next-to-leading order Feynman diagrams are shown in figure 1.5. In the leading order case the initial state bottom quark is taken from the sea quarks of the proton or antiproton. In next-to-leading order the bottom quark, that couples to the virtual W boson and thus produces the top quark, is produced by gluon splitting. Here an incoming gluon out of the proton splits in into a $b\bar{b}$ pair. One of these bottom quarks then couples to a virtual W boson and produces the top quark. The remaining bottom quark from the gluon splitting has in most

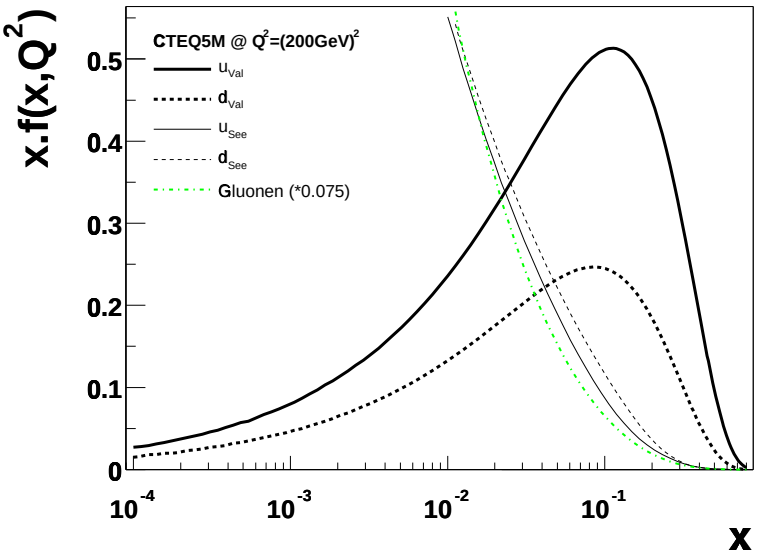

Figure 1.4: The CTEQ5M parton distribution function at Q=200 GeV.

cases low transverse momentum and high rapidity. In $p\bar{p}$ collisions the shown $ug \rightarrow dt\bar{b}$ process contributes $\approx$ 77% to the W-gluon production rate. The remaining 23% proceed via $\bar{d}g \rightarrow \bar{u}t\bar{b}$. The expression W-gluon fusion or Wg production originates from this diagram. Not only at the Tevatron, but also at the LHC this diagram is a major contributor to the t-channel production cross section.

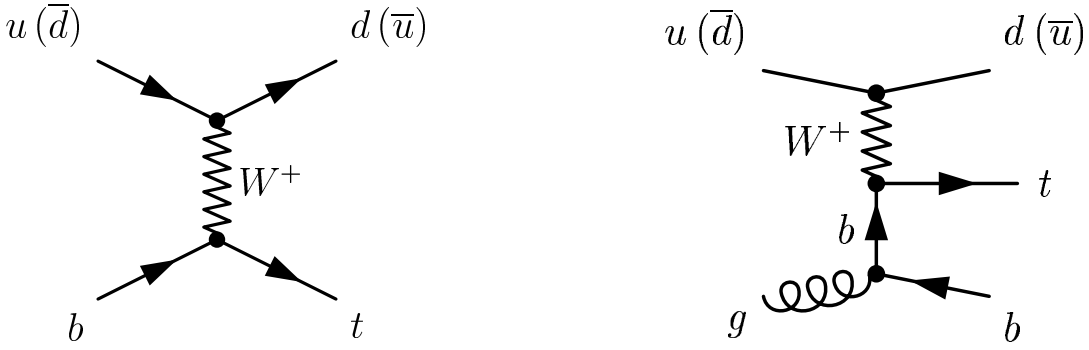

Figure 1.5: Examples of LO and NLO Wg-Fusion processes

The s-channel process shown in figure 1.6 has a predicted Standard Model cross section of 0.88±0.05(NLOscale) pb [18]. Here the uncertainties due to PDF and top quark mass are 5% and 10%, respectively. Throughout this analysis a total error of 13% on this prediction is assumed [17]. In the s-channel the two initial quarks annihilate to a highly virtual W-boson, which produces a top quark and a bottom quark. In contrast to the t-channel production, where

the $t\bar{b}$ pair forms a color octet state, it builds a color-singlet state in the s-channel production since the pair originates from a W boson. Therefore, the two processes are separately gauge invariant and cannot interfere.

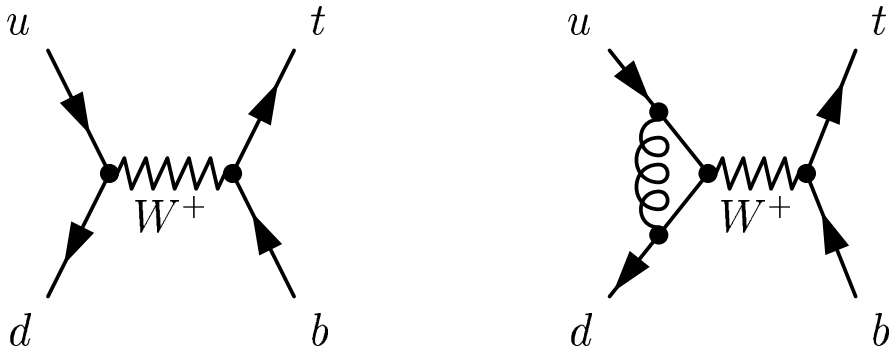

Figure 1.6: Examples of LO and NLO s-channel processes

The production cross section for the associated single top production is 0.094 ± 0.015 pb at the Tevatron. The leading order Feynman diagram is depicted in figure 1.7. In contrast to the s- and the t-channel productions here are two W bosons among the final state partons after the top decay. One originating from the top decay and one from the top production vertex. Thus in leading order, this process can be experimentally distinguished from the s- and t-channel production by reconstructing the W bosons. While associated production is not relevant at the Tevatron, it will significantly contribute to single top production at the LHC.

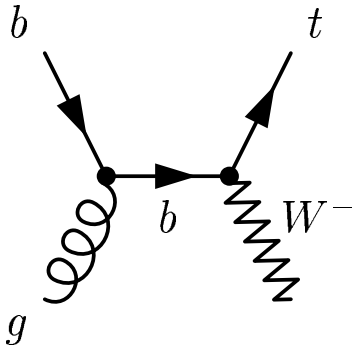

Figure 1.7: Example of an associated production process

In the s- and t-channel production the top quarks are produced 100% polarized along the direction of the down quark (anti-down quark) in the top rest

frame [19, 20]. This is due to the fact that the W boson couples only to left-handed fermions. This polarization can be measured since top quarks decay before the typical time scale for hadronization is reached. Hadronization describes the transition from partons to hadrons and in this stage information such as polarization is typically lost.

Generally speaking the Standard Model prediction for the electroweak single top quark production is about 40% of the top-antitop pair production cross-section. The major contributor to this value is the t-channel production. This process is gluon initiated. The s-channel cross section makes up about half of the t-channel cross section. This process is dominantly initiated by quark antiquark interactions at the Tevatron.

In Run I at the Tevatron the CDF and the D0 collaboration searched for electroweak single top quark production [21, 22, 23, 24]. The published 95% confidence level limits set by the CDF experiment are 13 pb on t-channel production and 18 pb on the s-channel production cross section. A combined search yielded an inclusive single top quark production cross section limit of 14 pb. The upper limits reported by the D0 collaboration are 22 pb for the t-channel and 17 pb for the s-channel production.

Chapter 2

The Experiment

The *Fermi National Accelerator Laboratory*, abbreviated Fermilab, is located in Batavia, Illinois. Batavia itself is located in the Western vicinity of Chicago in the State of Illinois. More than 2,500 scientists from throughout the world use Fermilab's facilities to carry out research in high-energy physics and Astrophysics. An aerial photo of the Fermilab area is shown in Figure 2.1.

Figure 2.1: Aerial shot of the Fermilab area. The grey circle in the back is the inner maintenance road of the Tevatron, the one in the front indicates the outer maintenance road of the main injector and the recycler.

2.1 The Accelerators

To reach the center-of-mass energies achieved at Fermilab, a whole chain of accelerators is needed. The last stage of the acceleration takes place in the *Tevatron*, a collider with a circumference of about six kilometers. Here, the protons and antiprotons reach an energy of nearly 1 TeV. During Run II, the two beams collide with a center-of-mass energy of 1.96 TeV.

An important quantity characterizing a collider is *luminosity*. Luminosity $\mathcal{L}$ is the product of incident beam flux with the mean target or beam density. The event rate for a particular type of event with the cross-section σ is given by the product $\mathcal{L} \cdot \sigma$. The typical luminosity for Run Ib was $\mathcal{L} = 1.6 \times 10^{31}$ cm^{-2}s^{-1}. During Run Ia and Ib from 1992 to 1996, the *Collider Detector at Fermilab*, CDF, collected a data set of 110 pb^{-1} *integrated luminosity* that was used for top-quark analyses.

For Run II, the accelerators were upgraded. The *main ring* was replaced by the *main injector* and a new antiproton storage ring, the *recycler*, was built. These two improvements should allow to increase the instantaneous luminosity up to $\mathcal{L} = 20 \times 10^{31}$cm^{-2}s^{-1}.The plan for Run II is to deliver an integrated luminosity of 4.4 fb^{-1} to 8.5 fb^{-1} [25]. Table 2.1 summarizes the collider characteristics in Run Ib and the goals for Run II.

Run	Ib/c(1993-1995)	II(goals)
Colliding bunches	(6×6)	(36×36)
Energy [GeV]	900	980
Antiproton Bunches	6	36
β^* [cm]	35	35
Bunch Length(rms) [cm]	60	37
Bunch Spacing [ns]	~ 3500	396
Interactions / Crossing	2.5	2.3
Typical Luminosity [cm^{-2}s^{-1}]	1.6×10^{31}	$8.6 - 16.1 \times 10^{31}$

Table 2.1: Operational performance of the Tevatron in Run I and goals for Run II [26, 25].

Run II started in June 2001. Unfortunately, the instantaneous luminosities achieved by the Tevatron within the first two years of Run II did not fully meet the design goals, but after several improvements to the acceleration process the instantaneous luminosity has reached the Run II design goals. Figure 2.2 shows the instantaneous luminosities of the stores in Run II. Figure 2.3 depicts the

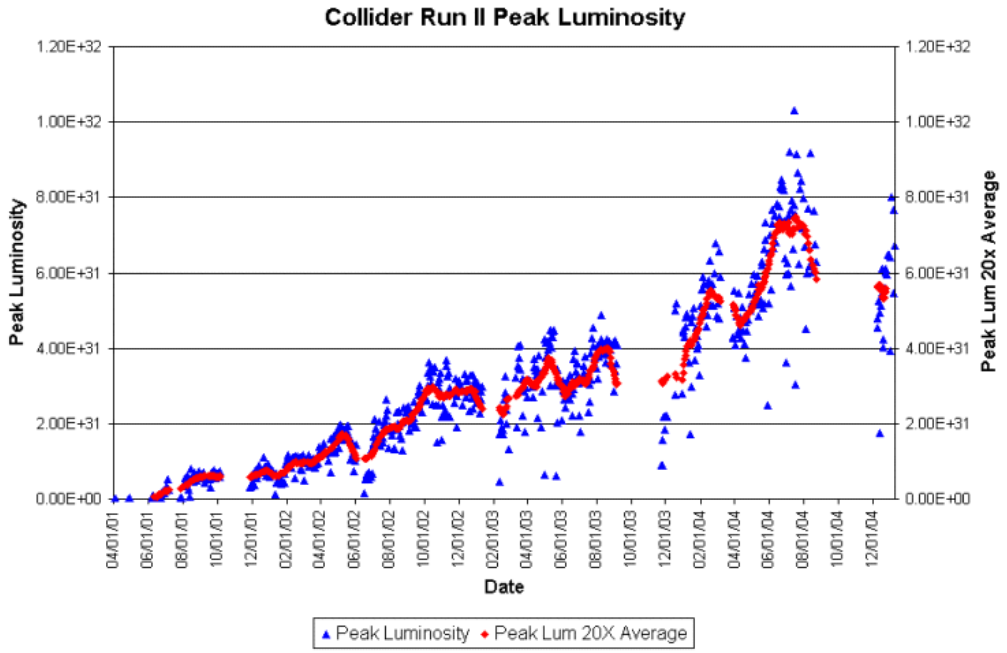

Figure 2.2: Initial luminosity per store in $\mathrm{cm}^{-2}\mathrm{s}^{-1}$.

increase of the integrated luminosity delivered by the Tevatron since the start of Run II.

2.2 The Collider Detector at Fermilab in Run II

CDF and D0 are two multipurpose detectors located in the interaction points of the Tevatron ring. One of the outstanding physics results achieved in Run I was the discovery of the top quark in 1995 by these two collaborations [10, 11] .

CDF is a general purpose solenoidal detector. It combines charged particle tracking with calorimetry and muon detection. The detector has both azimuthal and forward-backward symmetry. The CDF experiment is built and maintained by a collaboration of more than 50 institutions in eleven countries. The only German institute in the collaboration is the *Institut für Experimentelle Kernphysik* in Karlsruhe.

Some components of the CDF detector and the data acquisition system have been upgraded for Run II to deal with the increased instantaneous luminosities. In addition to this the coverage and capabilities of the existing subdetectors have been extended. A more detailed description of the CDF II detector can be found in its technical design report [27]. The Run I detector is described in detail elsewhere [28, 29].

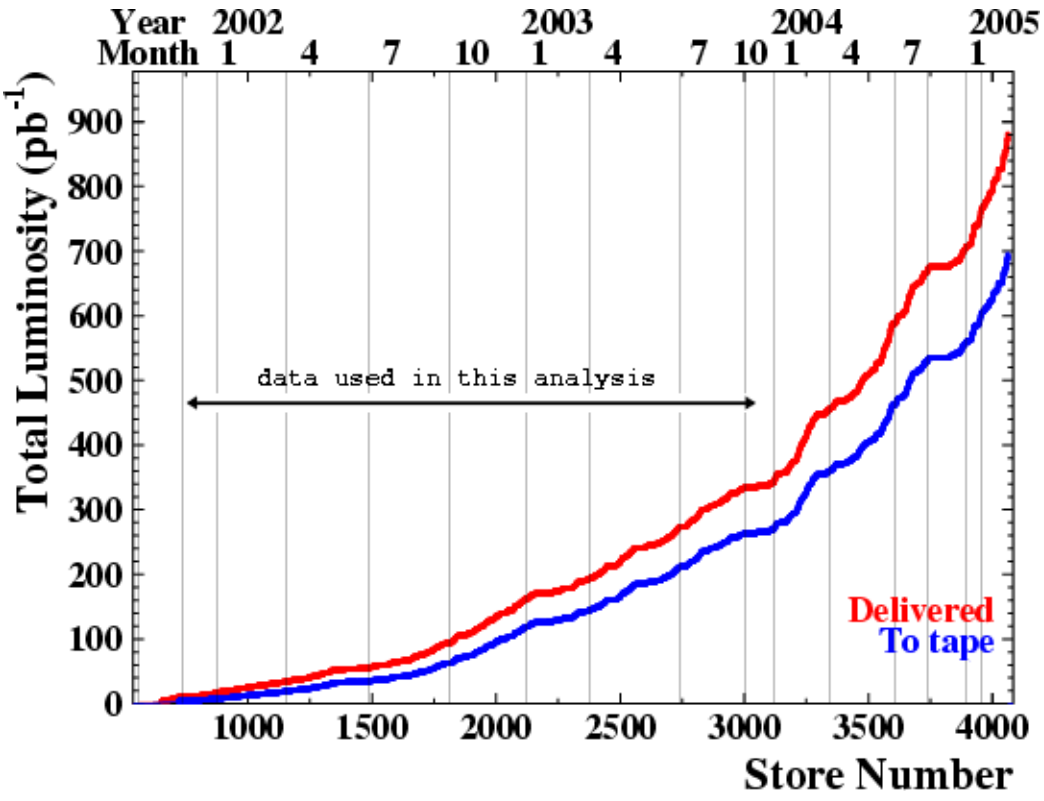

Figure 2.3: Delivered (upper curve) and recorded (lower curve) integrated luminosity since the start of Run II. The data taken from March 2002 to August 2003 was used for the analysis presented in this thesis.

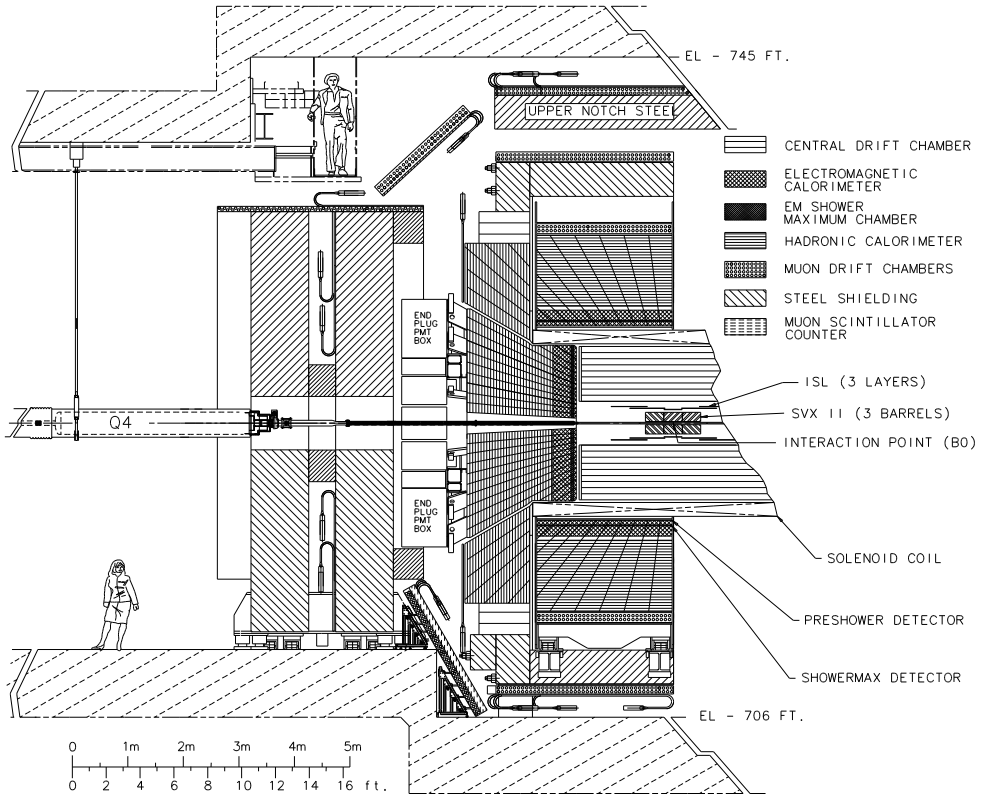

Figure 2.4: Elevation view of one half of the CDF II detector.

Figure 2.4 shows an elevation view of one half of the CDF II detector. In the CDF coordinate system, the polar angle θ in cylindrical coordinates is measured from the proton beam axis (z-axis) and the azimuthal angle φ from the plane of the Tevatron with respect to the positive x-axis, that points radially outward from the Tevatron ring. Throughout this thesis, *longitudinal* means parallel to the proton beam and *transverse* means perpendicular to the proton beam. The pseudorapidity is defined by $\eta = -\ln(\tan\frac{\theta}{2})$.

2.2.1 The Tracking System

CDF II uses the same solenoid as in Run I, but the complete tracking system of the Run I detector has been replaced. The superconducting solenoid is of length 4.8 m and radius 1.5 m and generates a 1.4 T magnetic field. As can be seen in Figure 2.5, the tracking system consists of silicon detectors near the interaction region and a drift chamber. Between the drift chamber and the solenoid, a time-of-flight detector has been added to improve the particle identification capabilities of CDF [30].

The silicon tracker system [31] consists of eight layers arranged in cylinders

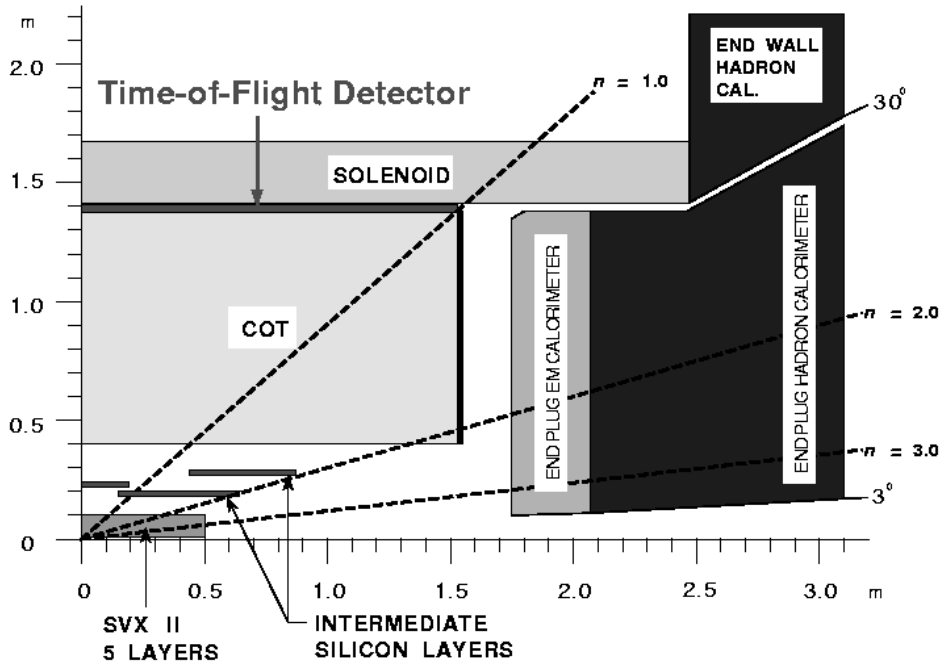

Figure 2.5: Longitudinal view of the CDF II tracking system.

spanning radii from 1.35 cm to 28 cm and lengths from 90 cm to nearly two meters for a total of six square meters of silicon and 722.000 readout channels.

Layer 00, the innermost layer, utilizes radiation tolerant silicon and low-mass readout cables between the sensors and readout electronics. Layer 00 was later added to the design of the vertex detector system to enhance its resolution and longevity [30]. To replace this layer relatively easily, it is supported by the beam pipe.

The silicon vertex detector, *SVX II*, consists of five layers of double sided silicon strip detectors at radii from 2.4 to 10.7 cm. The SVX II is 96 cm long and covers the pseudorapidity interval $|\eta| < 2$. The layers are assembled in three cylindrical barrels with beryllium "bulkheads" at each end for support and cooling of the modules. The modules consist of two readout units of silicon with a hybrid at each end mounted directly atop the silicon to avoid gaps. The design improves upon the previous SVX′ [32] used in Run I by enlarging coverage and elimination of gaps.

With an outer radius for the SVX II of 10.7 cm, additional tracking information is needed to robustly link to tracks found in the drift chamber. This is achieved by an additional silicon layer at a radius of 22 cm covering the interval $|\eta| < 1$ and two layers in the forward and backward direction. These *Intermediate Silicon Layers* (ISL) allow stand-alone silicon tracking over the whole region

of $|\eta| < 2$. The Institut für Experimentelle Kernphysik in Karlsruhe participated in the construction of the ISL [33].

The impact parameter resolution of the silicon system is expected to be better than the resolution of the SVX′. The averaged impact parameter resolution in Run II is measured to $\sigma_D = 34$ μm [34] for muon tracks with p_{T} around 1.5 GeV/c, where p_T is the transverse momentum of the particle in units of GeV/c. The impact parameter D is the distance of closest approach of the track helix to the beam axis measured in the plane perpendicular to the beam. Figure 2.6 shows the positive effect of Layer 00 on the expected impact parameter resolution.

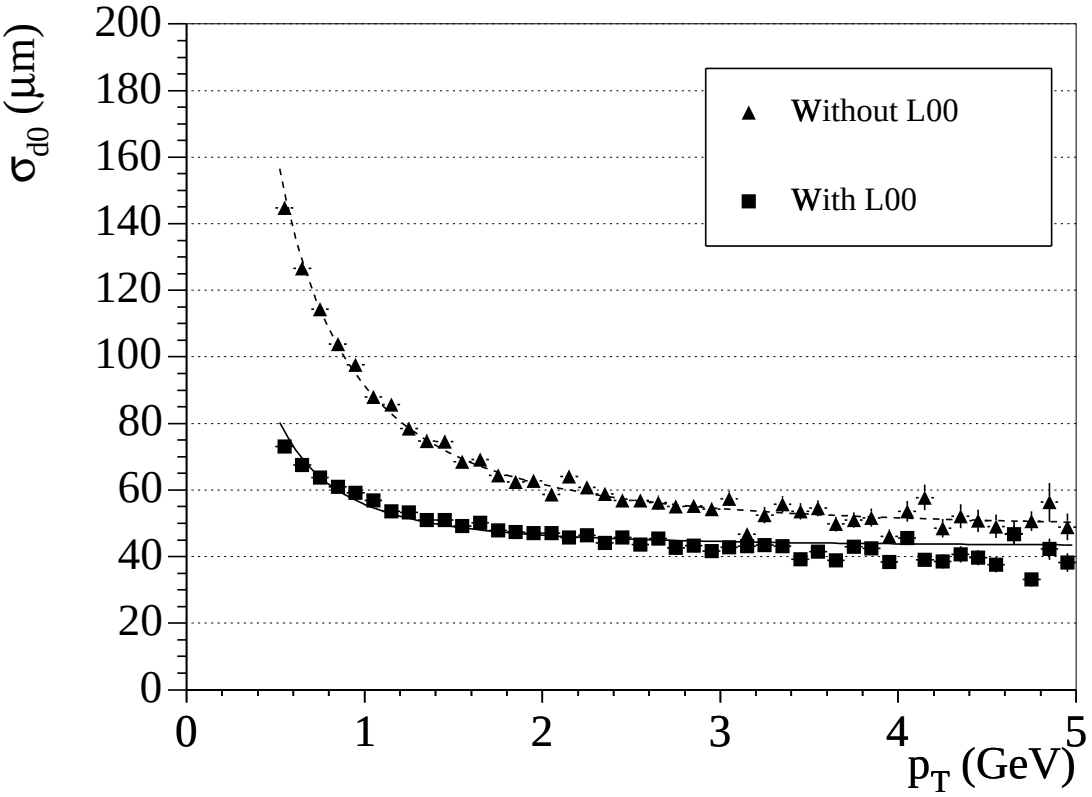

Figure 2.6: Effect of Layer 00 on the impact parameter resolution as a function of transverse momentum.

The drift chamber used during Run I, the *Central Tracking Chamber* (CTC), would suffer from severe occupancy problems at $\mathcal{L} \geq 1 \times 10^{32}\mathrm{cm}^{-2}\mathrm{s}^{-1}$. Hence, it has been replaced by the *Central Outer Tracker* [35], COT, that uses smaller drift cells and a faster gas to reduce drift times. The COT is a cylindrical open-cell drift chamber with inner and outer radii of 44 and 132 cm. It is designed to find charged particles in the region $|\eta| \leq 1$ with transverse momenta as low as

400 MeV/c. The COT is segmented into four axial and four stereo super-layers. Each super-layer contains 12 sense wires alternated with 13 potential wires which shape the field within the cell, yielding a total of 96 measurement. The COT uses Argon-Ethane (50:50) as the drift gas, which gives a maximum drift time of 180 ns. This time scale has to be compared to the beam crossing time of 396 ns. The resolution of the COT is comparable to the resolution of the CTC. Using the silicon detectors and the COT, the overall momentum resolution for charged particles is $\delta p_T/p_{\mathrm{T}}^2 < 0.1\%\ (\mathrm{GeV}/c)^{-1}$.

Between the COT and the solenoid, a *Time-of-Flight system* (TOF) is installed mainly for particle identification. It consists of scintillator panels which provide both timing and amplitude information. The timing resolution is 100 ps. The detector covers the central region out to $|\eta| < 1.1$ and is capable of distinguishing kaons from pions by their flight time difference with at least 2σ separation up to kaon momenta of 1.6 GeV/c. Figure 2.7 illustrates its performance using data.

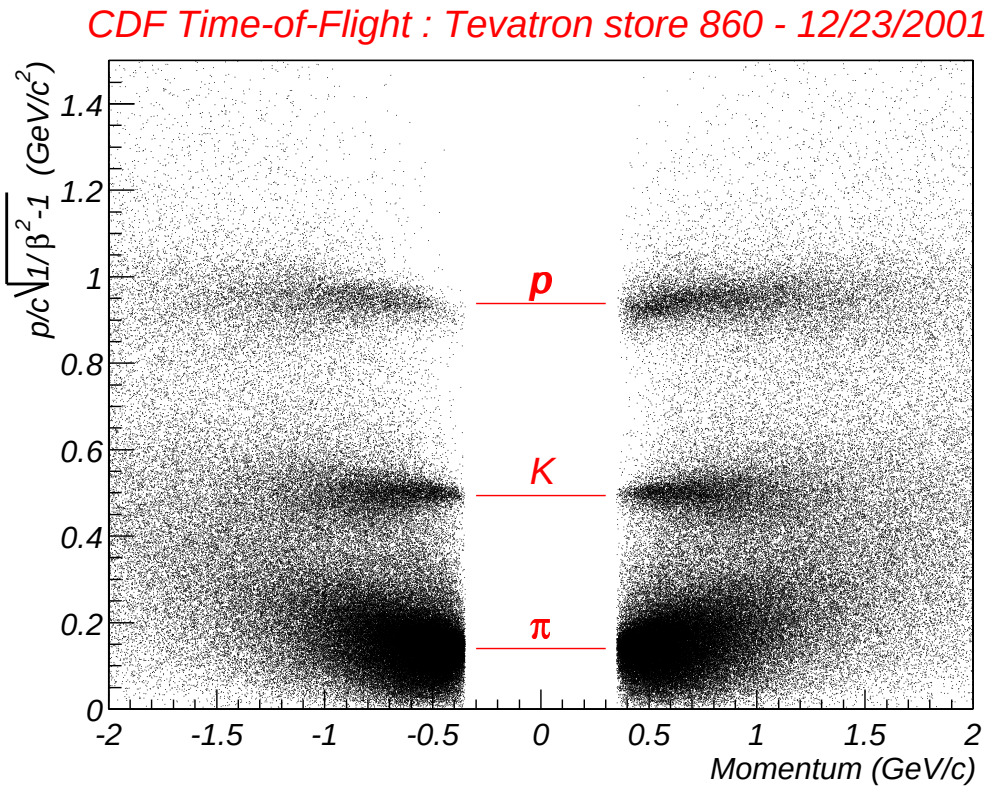

Figure 2.7: Performance of the time of flight system (TOF).

2.2.2 The Calorimeter Systems

The solenoid and tracking volume of CDF II is surrounded by calorimeters which cover 2π in azimuth and range in pseudorapidity from $\eta = -3.64$ to $\eta = 3.64$. They are segmented in azimuth and in pseudorapidity to form a projective tower geometry which points back to the nominal interaction point. As one can see in Figure 2.4, there are two main η regions of calorimeters, central and plug. Each region has an electromagnetic calorimeter (CEM and PEM) with lead absorbers and an hadronic calorimeter (CHA/WHA and PHA) with iron absorbers. Both electromagnetic calorimeters have pre-shower and stereo shower maximum detectors to improve their spatial resolution. Table 2.2 summarizes the properties of the calorimeters in Run II.

System	η Range	Thickness	Energy Resolution
CEM	$\lvert\eta\rvert < 1.1$	19 X_0, 1 λ	$13.5\%/\sqrt{E_T} \oplus 2\%$
PEM	$1.1 < \lvert\eta\rvert < 3.64$	21 X_0, 1 λ	$16\%/\sqrt{E} \oplus 1\%$
CHA	$\lvert\eta\rvert < 0.9$	4.5 λ	$75\%/\sqrt{E_T} \oplus 3\%$
WHA	$0.7 < \lvert\eta\rvert < 1.3$	4.5 λ	$75\%/\sqrt{E} \oplus 4\%$
PHA	$1.1 < \lvert\eta\rvert < 3.64$	7 λ	$74\%/\sqrt{E} \oplus 4\%$

Table 2.2: Summary of CDF calorimeter properties in Run II. The energy resolutions for the electromagnetic calorimeters are for incident electrons and photons, and for the hadronic calorimeters for incident isolated pions. The $\oplus$ signifies that the constant term is added in quadrature. The transverse energy E_T and the energy E are given in GeV.

In Run II, the scintillator-based calorimeters in the central region continue perform well. The electromagnetic section of the scintillating tile calorimeter in the forward region [36], $|\eta| > 1$, has a energy resolution of approximately $16\%/\sqrt{E}$ with a 1% constant term. The overall segmentation of the calorimeters is shown in Table 2.3.

System	$\lvert\eta\rvert$ Range	$\Delta\phi$	$\Delta\eta$
CEM/CHA/WHA	0.0 - 1.1(1.2h)	15°	~ 0.1
PEM/PHA	1.1(1.2h) - 1.8	7.5°	~ 0.1
PEM/PHA	1.8 - 2.1	7.5°	~ 0.16
PEM/PHA	2.1 - 3.64	15°	$0.2 - 0.6$

Table 2.3: CDF II calorimeter segmentation.

2.2.3 The Muon Systems

Four systems of scintillators and drift tubes are used to detect muons with CDF. The central calorimeters act as a hadron absorber for the *Central Muon Detection System* (CMU). In Run I, the CMU consisted of four layers of drift chambers located outside the central hadronic calorimeter. It covered 84% of the solid angle for the pseudorapidity interval $|\eta| < 0.6$ and could be reached by muons with transverse momenta greater than 1.4 GeV/c. In 1992, the system was upgraded by adding 0.6 m of steel behind the CMU and additional four layers of drift chambers behind the steel. This new system has been called *Central Muon Upgrade* (CMP). For $|\eta| < 0.6$ the CMP covered 63% of the solid angle while both systems overlapped in 53% of the solid angle. In addition, the pseudorapidity range of $0.6 < |\eta| < 1.0$ was covered by the *Central Muon Extension* (CMX) to 71% of the solid angle.

The changes for Run II in the muon systems represent incremental improvements. New chambers have been added to the CMP and CMX systems to close gaps in the azimuthal coverage and the shielding is improved. The forward muon system has been replaced with the *Intermediate Muon System*, IMU, covering a range from $1.0 \leq |\eta| \leq 1.5$. Table 2.4 gives an overview of the different muon systems in Run II.

	CMU	CMP	CMX	IMU
coverage	$\|\eta\| < 0.6$	$\|\eta\| < 0.6$	$0.6 < \|\eta\| < 1.0$	$1.0 < \|\eta\| < 1.5$
drift tubes (Run I)	2304	864	1536	none
drift tubes (Run II)	2304	1076	2208	1728
counters (Run I)		128	256	none
counters (Run II)		269	324	864
min p_T	1.4 GeV/c	2.2 GeV/c	1.4 GeV/c	$1.4 - 2.0$ GeV/c

Table 2.4: Design parameters of the CDF II muon detectors. The first row is the pseudorapidity coverage of the different detector systems. The total number of drift tubes used in Run I and II is listed in the second and third rows. The fourth and fifth rows list the total number of counters used in Run I and II. The last row states the minimal transverse momentum of a detectable muon.

2.2.4 Luminosity Measurement

In order to measure cross sections of physical processes it is essential to measure the luminosity corresponding to the used data set. Cherenkov Luminosity

Counters (CLC) are used at CDF. These counters monitor the average number of inelastic $p\bar{p}$ interactions in each bunch crossing. The rate of inelastic $p\bar{p}$ interactions is connected to the instantaneous luminosity $\mathcal{L}$ by

$$\mu \cdot f_{\mathrm{BC}} = \sigma_{\mathrm{in}} \cdot \mathcal{L} \ , \tag{2.1}$$

where μ is the average number of inelastic $p\bar{p}$ interactions per bunch crossing, f_{BC} is the rate of bunch crossings and σ_{in} the inelastic $p\bar{p}$ cross section. This cross section has been measured at $\sqrt{s} = 1800$ GeV and is scaled to $\sqrt{s} = 1960$ GeV. The number of $p\bar{p}$ interactions in a bunch crossing is described by the Poisson statistics where the probability of empty crossings is given by $P_0(\mu) = e^{-\mu}$. An empty crossing is observed if less than two counters observe a signal above a given threshold in either module of the CLC. The measured fraction of empty bunch crossings is corrected for the CLC acceptance and the value of μ is calculated. Using equation (2.1) the instantaneous luminosity can be calculated. The systematic error assigned to this measurement is estimated to 6%.

2.3 Data Acquisition and Monitoring

2.3.1 Electronics and Triggering

The CDF electronics systems have been replaced to handle the different bunch spacing in Run II. The increased instantaneous luminosity requires a similar increase in data transfer rates and the reduced separation between accelerator bunches a new architecture for the readout system. Figure 2.8 shows the flow chart of the new trigger system and data acquisition (DAQ). The electronics system was built to handle a 132 ns bunch crossing, but beam-beam interactions led to unstable beam conditions and therefore only every third bunch is filled resulting in an effective beam crossing time of 396 ns.

Due to the higher collision rate, the trigger in Run II must have a larger rejection factor while maintaining high efficiency for the broad range of physics topics. The lowest level trigger, "Level 1", uses output from the muon detectors for muon triggers and from all the calorimeters for electron and jet triggers. An addition to the previous run is the reconstruction of tracks using COT information already in "Level 1". This is done by the *XFT*, the eXtremely Fast Tracker [37]. A typical rate of the "Level 1" triggers is at present 18 kHz.

The second level trigger, "Level 2" uses the calorimeter trigger information with greater sophistication by running a cluster finder. In addition, data from the shower maximum detector (CES) can be used to improve the identification of electrons and photons. The most challenging addition for "Level 2" is the *Silicon Vertex Tracker* (SVT). The SVT provides the ability to select events with tracks which have large impact parameters. This opens a complete new

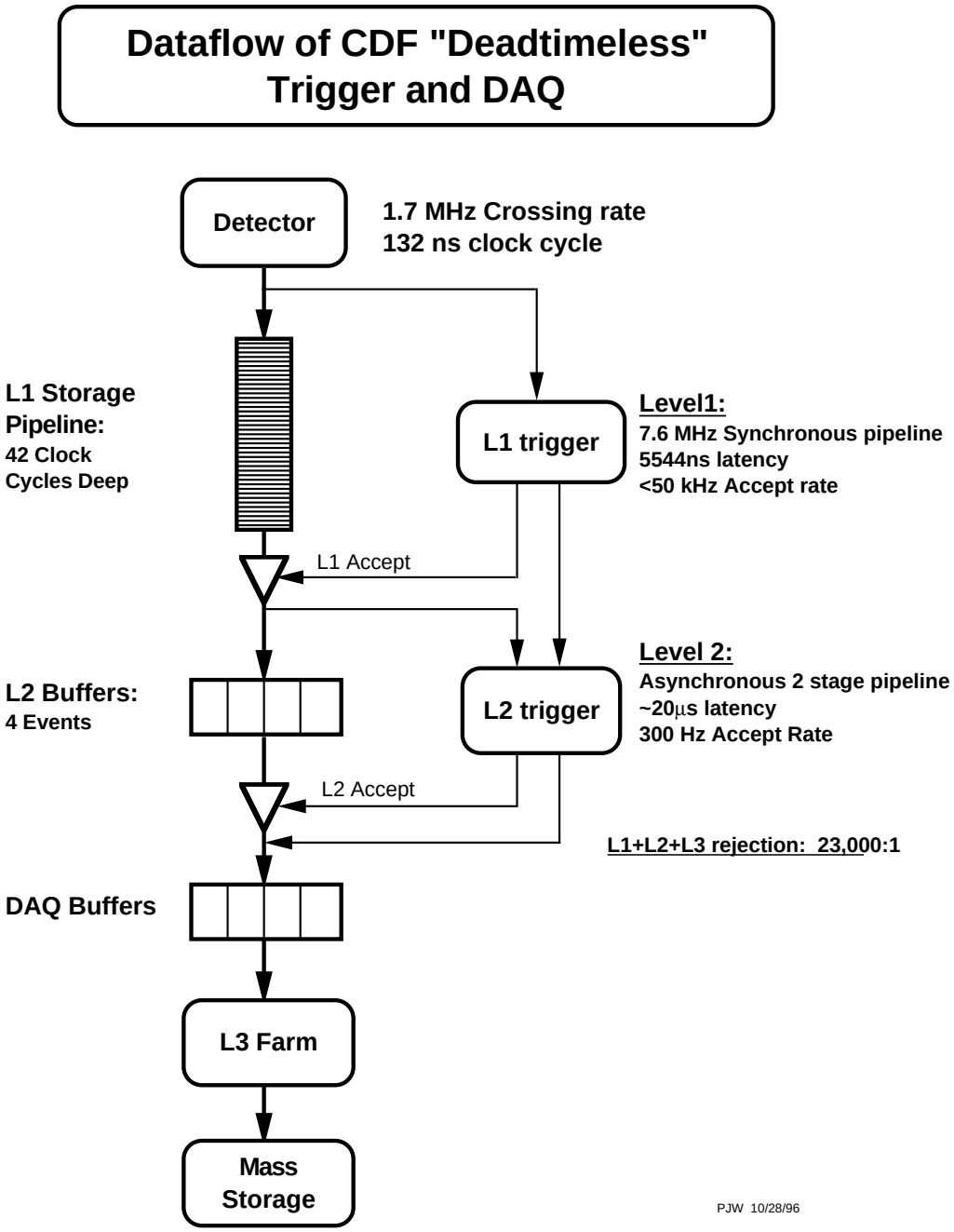

Figure 2.8: Functional block diagram of the CDF II data flow.

window for physics measurements at a hadron collider, like charm physics with high statistics and the study of hadronic B decays. The "Level 2" output rate is approximately 300 Hz.

The third level of triggering, the "Level 3", uses the algorithms run in the "offline" reconstruction. The software is run on a PC farm. The output rate of the "Level 3" trigger is approximately 75 Hz at present. The accepted events are then transferred to the *Feynman Computing Center* via network and stored on tape. To facilitate the handling of the huge data volumes collected with CDF, the data coming from "Level 3" is currently split into eight different streams. The triggers an event has passed decide to which streams this event belongs, e.g. all events passing any of the highly energetic lepton triggers end up in "stream B".

2.3.2 Monitoring of the Data Taking

A complex multi-purpose detector, like CDF, consists of many different detector systems. To take data with high efficiency and high quality, it is necessary to quickly spot problems with one of these subdetectors. This is achieved by a monitoring system that almost instantaneously produces characteristic distributions for each subsystem during data taking. At CDF, all processes receiving data from the DAQ are called *consumers* [38, 39, 40]. These monitoring systems are designed to not affect the data taking rate. Thus, these systems work with copies of the recorded data. The monitoring software analyses the data sets and compares the resulting distribution to reference distributions. If a distribution shows significant deviations to the default values a member of the shift crew, the consumer operator, is alerted by the system. Then, the consumer operator has to decide whether to notify the responsible experts or to proceed since these deviations are to be expected within the current data taking conditions. The monitoring displays are based on the *ROOT* object oriented analysis package [41], that provides C++ classes for the processing and visualization of histograms used to monitor the data quality. Examples for consumer monitors are:

- *YMon* monitoring the rates and distributions of each detector subsystem looking for bad channels, cards, voltage supplies, etc.
- *TrigMon* monitoring the various trigger quantities in each trigger bank looking for hot/failed channels, loose cables, trigger bits fired, bunch counter mismatches, photomultiplier spikes, etc.
- *XMon* monitoring the trigger rates
- *Stage0* fitting the drift constants for the gas in the drift chamber (COT)

- *LumMon* monitoring the luminosity measurements and the performance of the *Cherenkov Luminosity Counters* (CLC)
- *ObjectMon* monitoring the "Level 3" reconstructed objects, e.g. jets, electrons, muons, and tracks
- *SVXMon* and *SiliMon* monitoring the performance of the silicon detectors
- *BeamMon* fitting the position of the beam line for each run
- *DAQMon* monitoring the readout performances of almost all of the different crates, the different readout times, and the event sizes

The members of the CDF group of the "Institut für Experimentelle Kernphysik" played a major role in the design and the implementation of these systems.

Chapter 3

Event Reconstruction and Data Samples

The events in the different raw data streams are reconstructed on a PC farm [42]. The events with their reconstructed jets, tracks, muons, electrons, and other high level objects are then written into different data sets based on the triggers passed by the event. All events passing the high-E_T electron triggers are in the *BHEL08/9* data set for example. The *"08"* indicates the production version and corresponds to production with the *4.8.4* version of the CDF software. This data set was used in this analysis. The following sections will briefly describe the main reconstruction steps.

3.1 Track Reconstruction

Using information from the tracking detectors, particle trajectories can be reconstructed. Inside the solenoid, charged particles travel on a helix with its axis parallel to the magnetic field. At CDF five parameters are used to describe this helix [43]. These parameters are defined with respect to the point of minimum approach to the origin, the perigee.

- $\cot\theta$: the cotangent of the polar angle at the perigee
- C : the half curvature (same sign as the charge of the particle)
- z_0 : the z position at the perigee
- d_0 : the signed impact parameter; the distance between the helix and the perigee
- φ_0 : direction of the track at the perigee

3.1.1 Tracking in the Central Outer Tracker

In a first step, tracks in the *Central Outer Tracker* (COT) are reconstructed. The drift chamber is the tracking detector with the largest distance from the beam axis. Due to the fact, that its occupancy is lower and the tracks are more isolated, the reconstruction is easier for this detector in comparison to the silicon detectors.

There are two algorithms in use to reconstruct tracks in the COT. One algorithm is based on the code used in Run I to reconstruct tracks in the CTC [44]. In this approach, segments are reconstructed in the super-layers. These segments are then linked together to reconstruct the trajectory.

The other algorithm [45] uses one segment in the outer super-layers and the expected beam line to construct a reference track. The distances of the hits in the other super-layers from this reference are filled into a histogram. This histogram is used to determine the track parameters. Due to this procedure, the tracks are already beam constrained which improves the momentum resolution. However, the exact position of the beam line is not known when the reconstruction is done and the tracks reconstructed by this algorithm have a bias towards the assumed beam position used in the construction of the reference tracks.

3.1.2 Silicon Tracking

There are three different approaches to reconstruct tracks in the silicon system: *outside-in*, *inside-out* and *stand-alone* tracking. The *outside-in* tracking algorithm propagates a track found in the COT into the silicon system and tries to add hits to the track. After a hit has been added, the track parameters are recalculated using this additional information. In the CDF software, there are two implementations of this algorithm. One is based on the Run I code and uses a progressive fitter [46]. The other uses a Kalman fitter, which is the optimal fitter for this task, since this fitter naturally takes dE/dx and multiple scattering effects into account. This fitter and the algorithms based on it have been developed at the Institut für Experimentelle Kernphysik in Karlsruhe [47].

The *stand-alone* tracking algorithm is as well based on this Kalman fitter. The COT does not cover the forward and backward regions ($|\eta| > 1.1$). Thus, only the information of the silicon detectors can be used to find tracks up to $|\eta| < 2.0$. This is the task of the *stand-alone* algorithm. To reduce combinatorics, the algorithm uses only hits not used by the two *outside-in* strategies. The position of the beam line is needed for the construction of the track candidates causing a small bias towards the assumed beam position.

The *inside-out* tracking algorithm uses silicon stand-alone tracks to define a search road for hits in the COT detector. The hits in the road form a COT track that is fit using the silicon track z_0 and D information as constraints. The

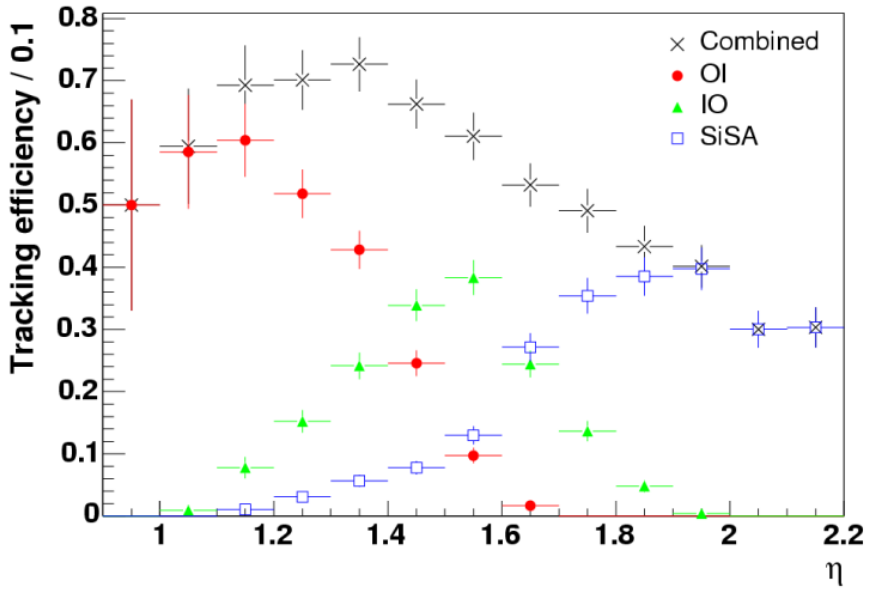

Figure 3.1: The tracking efficiency in the forward region $|\eta| > 0.9$ for different tracking algorithms.

silicon hits are finally refit using the new COT track as seed. Figure 3.1 shows the tracking efficiencies for the different algorithms in the forward region of the detector. Due to the fact that the *inside-out* algorithm refits the *stand-alone* tracks using COT information, the *stand-alone* tracking algorithm efficiency is small in the region $|\eta| < 1.5$.

3.2 Primary Vertex Reconstruction

Many analyses like life time measurements and analyses needing a b-tag require a precise measurement of the primary vertex position for each event. The primary vertex is the point from which all prompt tracks originate. In many applications, the position of the beam line can be used to estimate the primary vertex position in x and y, if the z coordinate is known. This method is limited by the size of the collision region, the beam width, but proved to be sufficient for most applications in b-physics. For events with high multiplicity (e.g. $t\bar{t}$) the primary vertex can be found with a better precision than the beam width. To achieve this goal Vxprim [48] was developed. The Vxprim program fits the primary vertex using

reconstructed tracks. Vxprim is used to fit the beam line on a run by run basis [49].

The Vxprim algorithm is run on production level. The results of this algorithm are used to determine the "beamline" positions [50]. The beamline is defined by the locus of all reconstructed primary vertices, thus the beamline is the position of the luminous region. The Vxprim algorithm uses all tracks fulfilling certain quality requirements. A track is accepted if for example at least two stereo and two axial super layers with at least six COT hits each have been assigned to this COT track. Silicon tracks reconstructed by an outside-in algorithm are required to have at least four $r-\varphi$ hits. In a first step all tracks passing the quality cuts are fit to a common vertex. In an iterative "pruning" process each track is removed from the vertex fit and a χ^2 of this track with respect to the vertex is calculated. If the highest χ^2-value of these tracks exceeds a certain threshold, the track is removed. Then the vertex fit is repeated using the remaining tracks and this pruning procedure is continued until all tracks pass the χ^2 cut. The vertex is accepted if a minimum number of tracks is assigned to the vertex.

3.3 The Beamline

As mentioned above the beamline is the luminous region of the proton-antiproton collisions within the CDF detector. The beamline can be used to refine the knowledge of the primary vertex position in a given event.

The beamline is constructed by the positions of the primary vertices of each run section. The transverse profile of the luminous region inside the CDF can be described by Gaussian functions in x and y. The means of these Gaussians define the beam position. The width of these Gaussians varies along the length of the interaction region due to the focusing of the beams. This can be expressed by the following equation [51, 52]:

$$\sigma(z) = \sqrt{\epsilon \cdot (\beta^* + \frac{(z - z_{\min})^2}{\beta^*})}, \tag{3.1}$$

where ϵ is the transverse emittance, β^* the amplitude function at the interaction point, and $z_{\min}$ the z position of the minimum of the amplitude function. The measured value for this width at the position $z = 0$ is approximately 30 μm, rising to approximately 50 to 60 μm at $|z| = 40$ cm [53, 54, 55]. Thus, the knowledge of the beam position coordinates x and y gives a good estimate for the primary vertex position in an event. Unfortunately, the beams are not centered in the detector and not parallel to the detector z-axis. At $z = 0$ the beamline is at $(x_0, y_0) \approx (-2.0, 3.9)$ mm. In early 2004 the interaction point was moved closer to the origin. The dependence of the x and y position of the

beam in z can be described by a straight line:

$$\bar{x} = x_{slope}z + x_0; \quad \bar{y} = y_{slope}z + y_0 \tag{3.2}$$

The slope is about 5.0 μm/cm in the horizontal plane (x_{slope}) and about 1.7 μm/cm in the vertical plane y_{slope}. These parameters are rather stable during periods of continuous data taking, the position of the beamline varies from its mean position not more than 20%.

3.4 Electron Reconstruction

High momentum electrons leave isolated energy deposits in adjacent towers in the electromagnetic calorimeters. These towers can be identified and merged into one electromagnetic cluster. Electrons are then identified in the central electromagnetic calorimeter (CEM) as isolated clusters which match a XFT track in the pseudorapidity rage $|\eta| < 1.1$. The corresponding energy deposition in the hadronic calorimeter should be low. The electron hardware trigger requires the assigned XFT track to exceed a transverse momentum of 8 GeV/c and a electromagnetic transverse energy of the cluster $E_{\rm T} > 16$ GeV. The ratio of energy depositions in the hadronic and the electromagnetic calorimeter has to be less than 0.125.

3.5 Muon Reconstruction

The muon system is described in 2.2.3. Muon candidates are identified as isolated tracks which can be extrapolated to the muon stubs. Muon stubs are reconstructed track segments in one of the four-layer stacks of the muon chambers (CMX,CMU,CMP). The muon hardware trigger requires an XFT track with $p_{\rm T} > 8$ GeV/c matched to such a track segment or stub in the joint CMUP configuration or in the CMX.

3.6 Jet Reconstruction

The hadronization of a final state quark creates a jet of hadrons. Hardronization describes the transition form colored partons to color neutral objects such as hadrons. These particles form then a particle jet. The energy of the hadrons is measured in the calorimeters. The momentum of the initial quark can be reconstructed by combining the energy measurements in the calorimeter towers that belong to the jet. Figure 3.2 illustrates the transition of fundamental particles to calorimeter jets. The out of cone particles correspond to particles originating from the parton but their energy deposit is not assigned to the calorimeter jet.

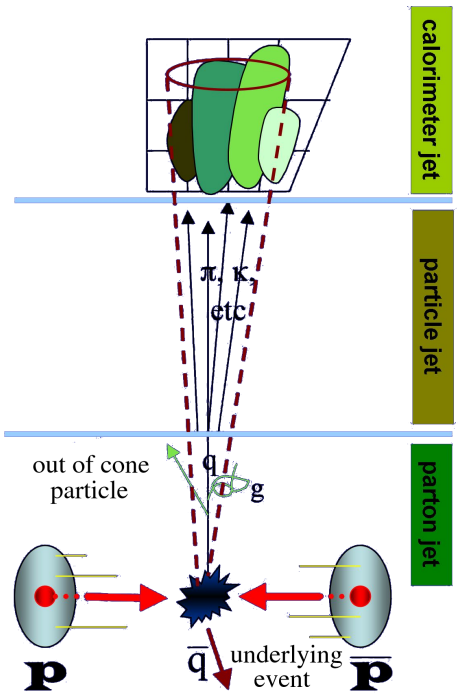

Figure 3.2: An illustration of the transition from partons to calorimeter jets.

3.6.1 Algorithms

Three different algorithms to reconstruct jets are implemented in the CDF software [56].

JetClu

This algorithm has been the standard algorithm in Run I. Thus, its systematics are very well understood. Firstly, this algorithm selects a seed tower. Then it draws a cone around this tower with a fixed radius in the η-φ plane. All calorimeter towers inside this cone are combined to form the jet. The axis of this jet is used as the new direction of the cone axis in the next iteration of this algorithm. If the jet axis stays stable, the reconstruction of this jet is finished. Seed towers are all calorimeter towers with a measured energy above a certain threshold.

Although this algorithm works very well in the dense environment of hadron-hadron collisions, it has two problems when it is applied to partons in order to derive theoretical predictions:

- A single parton with energy above threshold will serve as a seed. But, if the momentum of this parton is distributed to two partons with each

having half the energy, both might fail the threshold cut. This is called the collinear problem.

- If there are two high energetic partons that have a distance in the η-φ plane that exceeds the cone size, two jets will be formed by the algorithm. A gluon emitted by one of the partons might move the jet axis in a way that now both partons and the gluon form just one jet. This is called the infrared problem.

Midpoint Cone Algorithm

The midpoint cone algorithm is based on the simple cone algorithm described in the previous section. It was formulated to get rid of the problems of its predecessor by adding the midpoints between two towers as further seeds.

K_T-Clustering Algorithm

The K_T-clustering algorithm calculates the distances between all energy depositions based on the formula $d_{ij} = \min(p_{T,i}^2, p_{T,j}^2)\frac{\Delta\mathcal{R}_{ij}^2}{D^2}$, where $\mathcal{R}_{ij}$ is the distance between two momentum vectors in the $\eta - \varphi$ plane and D is a parameter of the jet algorithm. The two momentum vectors with the smallest distance are combined and this new vector is used instead of the two original ones. All distances are then recalculated and the procedure is iterated as long as there are distances below a certain threshold value.

This algorithm works very well on the partonic level and for experiments located at an electron-positron or electron-proton collider with a rather clean environment. Right now, the results of this algorithm for the experiments at the Tevatron are not well understood and disagree with the other two algorithms for low energetic jets. The measured inclusive cross section in Run I for JetClu and K_T jets differ about 37% for a jet transverse energy of 60 GeV [57]. The K_T jets are found to assign 7% more transverse energy to the jets than the cone algorithms. This discrepancy can be partially explained by the effects of final state hadronization on reconstructed energy. In simulations the cone algorithm finds jets with less transverse energy when using final state particles (after hadronization) in comparison to the parton jets (before hadronization). In contrast, the particle jets found by the K_T algorithm have more energy compared to the parton jets due to the merging of nearby partons to one single jet. Currently several efforts are taken to understand the behavior of the K_T algorithm in $p\bar{p}$ collisions.

3.6.2 Jet Energy Corrections

Not all the particles created during the fragmentation of a hadron are measured in the calorimeter, nor do the jet algorithms combine all towers correctly. Furthermore, the calorimeter response depends on the pseudorapidity of the tower and generally varies with time. In addition there can be extra energy in the calorimeter cell originating from multiple $p\bar{p}$ interactions in the same bunch crossing and from the so-called underlying event. This contribution is due to momentum transfer resulting from the interactions of the proton or antiproton remnant partons. To compensate for these effects, the energy of the reconstructed jet needs to be corrected to match the energy of the initial parton one aims to reconstruct. Only then, one gets the right momenta and masses for the primary partons.

A group within CDF has derived a set of jet corrections for Run II [58]. Right now seven different corrections are applied to a jet. The following corrections are performed:

1. η-dependent relative corrections
2. time-dependent corrections
3. raw energy scale corrections for Run IIa to agree with Run Ib
4. multiple interactions corrections
5. absolute energy corrections (from calorimeter energy to particle energy)
6. underlying event corrections
7. out-of-cone corrections

The single corrections are performed sequentially. Applying "Level 4" corrections means that the first four corrections are applied. Figure 3.3 illustrates the impact of the relative corrections. The goal of these corrections is to adjust the forward calorimeter scale to the central calorimeter scale, where the calorimeters are better calibrated and understood. The left plots shows the calorimeter response before applying these corrections. The data and MC simulation are in good agreement. The right plots shows the result of the correction. The corrected distribution is independent of the pseudorapidity of the jet.

3.7 The Identification of Bottom Jets

In many physics analyses, it is crucial to know the flavor of a quark producing the jet to extract a signal. It is possible to discriminate jets originated by a

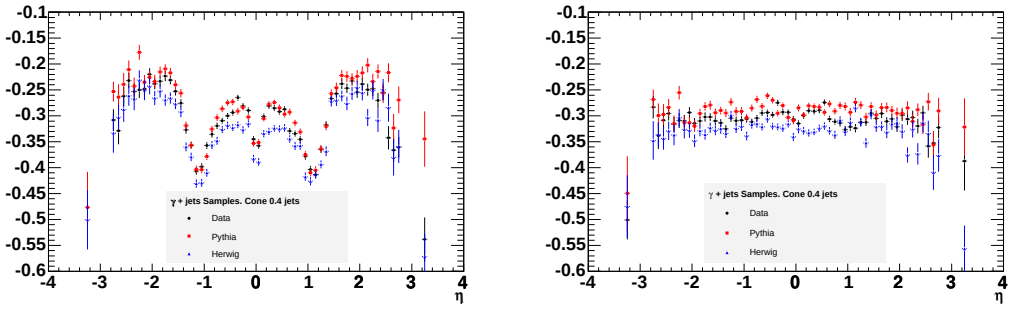

Figure 3.3: The η-dependence of the relative calorimeter response in arbitrary units before (left) and after applying the relative corrections (right).

bottom quark from jets originated by lighter quarks or gluons. Due to the relatively large mass of the bottom quark, the bottom hadron carries most of the momentum of the original quark. Thus, the hadron is boosted and, due to its lifetime of approximately 1.5 ps, it travels a sizeable distance before its decay.

3.7.1 The Jet Probability

One way to tag a jet is to look for tracks near the jet axis that do not originate from the primary vertex. For every track, one can calculate the probability p_i that the particle belonging to this track has been produced at the primary vertex. This probability is constructed by fitting the impact parameter significance distribution of tracks to be found within a jet cone. The fit resolution function $R(S)$ with $S = d_0/\sigma_{d_0}$ is then used to determine the probability $p_i(S_0)$ for a track that the impact parameter significance S_0 is due to the detector resolution:

$$p_i(S_0) = \frac{\int_{-\infty}^{-|S_0|} R(S)dS}{\int_{-\infty}^{0} R(S)dS} \tag{3.3}$$

Using all N tracks of positive impact parameter associated to this jet, a joint probability P is calculated whether this jet has been formed at the primary vertex. For tracks not originating from the primary vertex, this probability peaks at $P = 0$, whereas the distribution for jets containing tracks originating from the primary vertex is flat. Therefore, a jet is tagged if the probability P_{jet} is smaller than a given threshold [59].

3.7.2 The *SecVtx* Algorithm

The second algorithm in use at the CDF is called *SecVtx*. This algorithm searches for a secondary vertex directly. This algorithm is essentially unchanged

from Run I, only the track selection has been retuned to match the improved CDF II dectector. A detailed description of the algorithm can be found in [60].

The first step of the algorithm is to identify the primary vertex of the event. If a high momentum lepton is identified in the event, the vertex with the smallest distance to the lepton is used. In the absence of such a lepton, the vertex with the highest total scalar sum of transverse momentum of associated tracks is used. The position of the primary vertex is than refit by using all the tracks that are found within a window of ±1cm around the z-position of this vertex and fulfilling the requirement to have an impact parameter significance $|d_0/\sigma_{d_0}| < 3$ relative to the beamline. In a pruning process all used tracks are removed that contribute a $\chi^2 > 10$ to the fit. If no tracks survive the beamline profile is used for the primary vertex position estimate. The next step of the algorithm is the actual reconstruction of the secondary vertex. Since the algorithm operates on a per-jet basis, the tracks within the jet cone are considered for each jet in the event. All tracks not passing quality cuts on the number of silicon hits assigned to the track, quality of those hits and the χ^2-value of the track fit are rejected. Only jets to which at least two such good tracks have been assigned are "taggable". Based on the impact parameter significance with respect to the primary vertex displaced tracks are then selected and serve as input for the algorithm. *SecVtx* uses a two-pass approach to find displaced vertices. In the first pass the algorithm uses all tracks with $P_{\mathrm{T}} > 0.5$ GeV/c and $|d_0/\sigma_{d_0}| > 2.5$. In this pass at least three tracks are required to form a secondary vertex. If this first pass fails, the track requirements are tightened ($P_{\mathrm{T}} > 1$ GeV/c and $|d_0/\sigma_{d_0}| > 3$), but yet two-track vertices are accepted. Once a displaced vertex is found in a jet, certain criteria are applied to the vertex to enrich vertices originating from b and c hadron decays. For example one requirement is that $L_{2d}/\sigma_{L_{2d}} > 3$. Here L_{2d} denotes the two-dimensional decay length of the secondary vertex, that is calculated as a projection onto the jet axis of the vector pointing from the primary to the secondary vertex in the $r - \phi$ view only.
The left plots in figure 3.4 shows the efficiency to tag a fiducial b-jet in MC $t\bar{t}$ events in the central region of the tracker depending on the transverse jet energy. The right plot in this figure denotes the pseudorapidity dependence of the tagging efficiency of jets with $E_{\mathrm{T,jet}} > 15$ GeV. This efficiency is $\approx 40\%$ in the central region for $t\bar{t}$ events. Averaged over $E_{\mathrm{T,jet}}$ and η_{jet} the efficiency to tag a heavy flavor jet is 0.240 ± 0.007 for data and 0.292 ± 0.010 for MC events. Therefore a scale factor of 0.82 ± 0.06 has to be applied to MC derived acceptances using this tagger. This scale factor accounts for the fact that in MC events the quality of the tracks is overestimated. Table 3.1 summarizes these numbers. Unfortunately not only secondary vertices originating from heavy quark decays are identified but also so-called mistags. These mistags correspond to wrongly assigned vertices fulfilling all required vertex quality criteria. Sources for mistags are for example light flavor jets, where by accident a secondary vertex was found. Figure 3.5 shows the mistag efficiency for the algorithm as a function

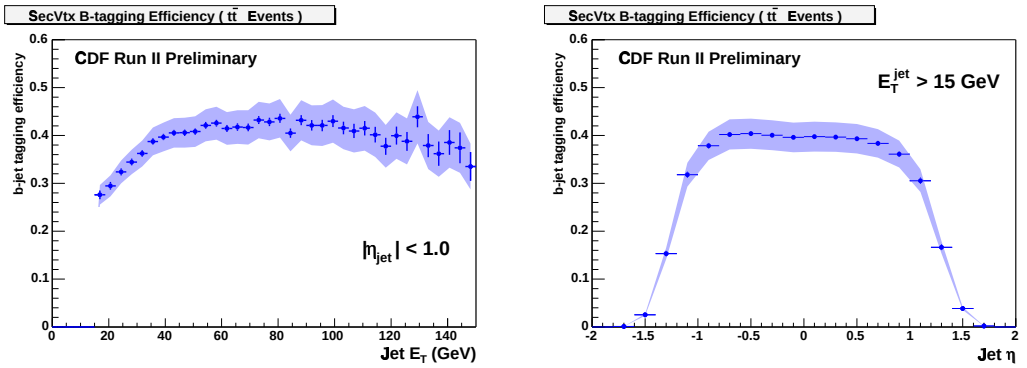

Figure 3.4: Efficiency to tag a b-jet as function of the transverse jet energy for $t\bar{t}$ events.

$\epsilon(Data)$	0.240	$\pm$	0.007
$\epsilon(MC)$	0.292	$\pm$	0.010
Scale Factor	0.82	$\pm$	0.06

Table 3.1: Efficiencies to tag a heavy flavor jet for data and Monte Carlo events, and the resulting scale factor.

of $E_{\mathrm{T,jet}}$ and η_{jet}. Although these numbers are quite small (0.4-0.6%) compared to the tagging efficiency, the reader should keep in mind that the production rate of light flavor jets is much higher than the one for heavy flavor jets. Thus mistags are a significant source of background events for any analysis using this tagger.
In order to estimate the kinematic properties of such mistags, a mistag matrix has been developed within the CDF collaboration, that provides a mistagging probability depending on the number of tracks assigned to the jet, $E_{\mathrm{T,jet}}$, η_{jet} and the azimuthal angle ϕ_{jet}. In addition the scalar sum of the transverse momentum of all taggable jets is considered.

3.8 Detector Simulation

The understanding of efficiencies, acceptances and the kinematic properties of signal and background processes requires a deep knowledge of the physics processes and the detector response. Therefore, Monte Carlo generators are used that randomly generate hard parton interactions according to the probability density of phase space. The resulting partons are then processed by a parton showering to simulate gluon radiation and fragmentation. The resulting particles are then handed to the detector simulation. The CDF collaboration uses

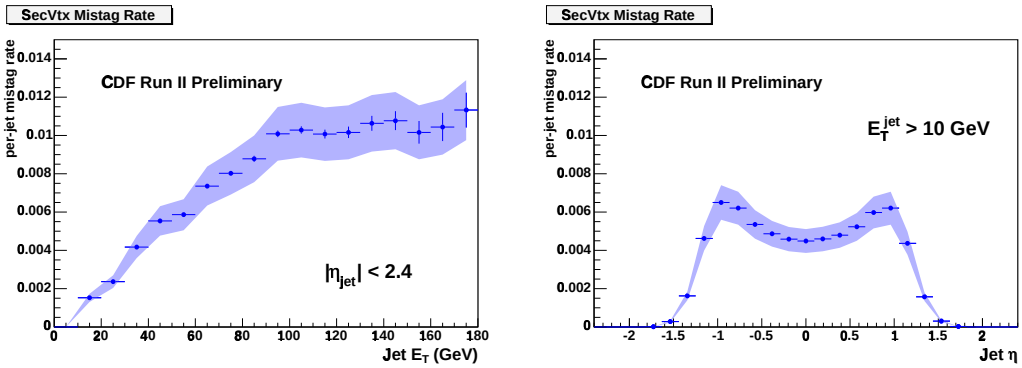

Figure 3.5: Efficiency to misidentify a heavy flavor jet as function of the transverse jet energy and the jet pseudorapidity.

the GEANT3 [61] package to simulate the tracking of particles through matter. This package calculates the charge deposition in the silicon layers using a simple geometrical model based on the path length of the ionizing particle. To model the drift chamber,COT, a GARFIELD simulation is used, that was tuned to match the data [62]. The calorimeter simulation GFLASH [63] was also tuned using test beam data for electrons and high transverse momentum pions. A detailed description of the CDF II simulation can be found elsewhere [64].

3.9 Data Samples

In this section, the data samples used in this analysis will be characterized and the data reprocessing will be explained. To take advantage of newer calibrations and correct for bugs in the reconstruction code used originally, most of the high level objects have been remade. CDF software version *4.8.4 Production* was used for this task. The calorimeter reconstruction was redone with the latest calorimeter constants. The jets, electromagnetic objects, muons, and calculated missing transverse energy were dropped on input and remade. The tracks were refit to take correctly the alignment into account. Subsequently, new primary vertices were reconstructed and the latest version of the b-tagging algorithm was used.

To facilitate the further data analysis, the events were written out in an extended ntuple, so-called *TopNtuple*. In fact, *TopNtuple* is a *micro-DST* and offers a new framework to easily access the data and analyze it using ROOT. Developing code is much faster within this framework than in the CDF offline framework. Furthermore, the events can be read in much faster. All high level objects stored in the *TopNtuple* contain the required information as their counterparts in the standard CDF event data model (EDM).

3.9.1 Collider Data Sample: *btop0g/j* and *btopIg/j*

The data sample used in this analysis is called *btop*. It is based on the high-energetic electron sample (*BHEL08/9*) and muon sample (*BHMU08/9*). However, a few additional cuts on the lepton candidates were applied to clean up the sample. These cuts are discussed in detail in chapter 4.

For this analysis the good runs list version 4.0 of the CDF Lepton+Jets Working Group as of 12/01/03 was used. This list contains all runs, where all detector components needed for this analysis were functional and included in the data-taking process. If for example the beam radiation is above a critical threshold the silicon chips are endangered and thus not switched on. Table A.1 in the appendix lists the integrated luminosities for all processed file sets of the electron samples and table A.2 for the muons. The analyzed data corresponds to an integrated luminosity of (162 ± 10) pb^{-1} with an error on the luminosity of 6% [65] for the CEM electrons and CMUP muons. The CMX muon luminosity is 150 pb^{-1}. All good runs up to September 07, 2003 have been used.

Chapter 4

Event Selection Criteria and Event Yield for Single Top Production

The experimental signature of signal top events is characterized by the decay products of the top quark and additional jets. The production process was described in 1.2. For the s-channel process an additional jet is originating from the bottom quark of the V_{tb} Vertex. In case of t-channel production one expects a light flavor quark jet emitted at high pseudo-rapidity and an additional bottom jet arising from initial state gluon splitting. This jet is typically produced in such high pseudo-rapidity regions that it cannot be detected. Additional jets are also created by gluon radiation. The production mode where the bottom quark involved in the hard process originates directly from the seaquark distribution of the proton or antiproton is suppressed by the PDF. Within the Standard Model the top quark decays to almost 100% to a W-Boson and a bottom quark. In order to suppress quantum chromodynamic mulitijet events the selection focuses on the leptonic decay modes of the W-Boson. We only consider the decay modes $W \to \mu\nu_\mu$ and $W \to e\nu_e$, since the τ lepton identification with good purity has low efficiency for CDF (about 20% of the mean values for electrons or muons). Since CDF implemented a trigger system for isolated high transverse momentum electron and muon candidates, these data sets are used for this search.

In this chapter the event detection efficiency for single top events are presented and the event yield to be expected is calculated. These numbers are the essential ingredients to calculate the production cross section or calculate upper bounds on the cross section. To calculate these efficiencies and acceptances we make use of Monte Carlo matrix element generators in conjunction with parton shower programs and the CDF detector simulation.

4.1 Monte Carlo Samples

To derive the event detection efficiencies for s- and t-channel single top events, we make use of a Monte Carlo event generator technique. The following section describes the Monte Carlo samples used for this analysis.

The signal Monte Carlo samples used for this analysis are generated with MadEvent [66], PYTHIA v6.203 [67] and TopRex [68]. Simulation and production were performed in the 4.9.1 release of the CDF offline software. The reconstructed events were passed through the "TopFind" module, linked against CDF software release 4.11.1, to produce TopNtuples [69].

Three different Monte Carlo programs have been used to estimate the systematic uncertainties due to the underlying modeling of Standard Model single top quark production. In contrast to PYTHIA, that is only capable of leading order $2 \to 2$ single top quark production on matrix element level (see left diagram in figure 4.1), MadEvent and TopRex have also the $2 \to 3$ matrix elements build in (see right diagram in figure 4.1). In the following the $2 \to 3$ processed will be referred to as "NLO"-diagram. Another weakness of PYTHIA is that the simulated top quarks are unpolarized in contrast to the prediction, whereas MadEvent and TopRex model the polarization accordingly. The s-channel process that is well modeled by MadEvent and TopRex, whereas the interaction scale used in the PYTHIA program was too low. The t-channel process at leading order shows a discrepancy concerning the kinematic distributions of a bottom quark or jet not originating from the top decay compared to the next-to-leading order calculations. On leading order matrix element level this quark is not present, it is generated by the parton shower algorithm. On next-to-leading order matrix element level this "second" bottom quark arises from the initial gluon splitting. Figure 4.1 depicts the t-channel Feynman diagrams of single top quark production. Technically, in the leading order process one starts with

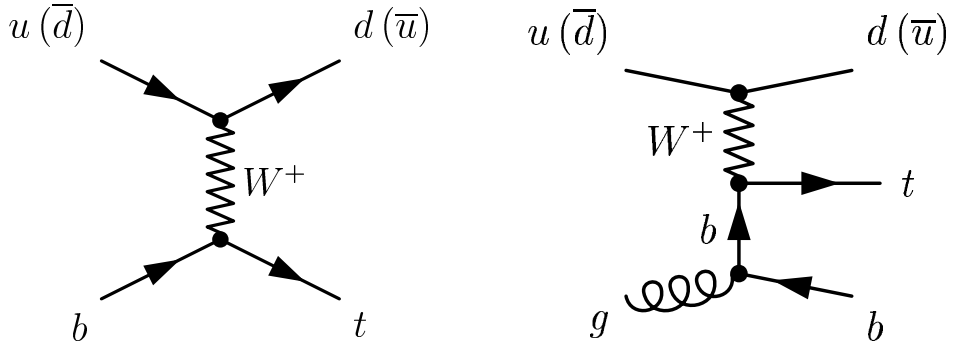

Figure 4.1: Feynman diagrams for single top production: t-channel $2 \to 2$ after introduction of a b-quark PDF (left), t-channel W-gluon-fusion diagram, is a NLO contribution if a b-quark PDF is used (right).

the bottom quark PDF in the initial state. Then a showering program forms an initial state for each event by backward evolution to avoid collinear singularities if the bottom quark is taken to be massless. This can be seen if one considers the propagator of the bottom quark in the matrix element:

$$\frac{1}{p_b^2} \approx -\frac{1}{EE^*(1-cos(\theta))} \tag{4.1}$$

Here E denotes the energy of a gluon from the proton or anti-proton, E^* is the energy of the of the bottom quark and θ the angle between the two. Thus, in the limit $\theta \to 0$ the matrix element approaches infinity. By this procedure most of the events will feature soft, forward final state "second" bottom quarks. In contrast to these soft bottom quarks, the obtained "second" bottom quarks using the next-to-leading diagram are rather hard with high transverse momentum. To match the next-to-leading order prediction for the transverse momentum distribution for the "second" bottom quark a combination of leading order and next-to-leading order events is used, a "matched" sample.

The goal of this matching procedure is to produce a smooth spectrum in $p_{\mathrm{T}}(b_2)$ by combining the leading order (LO) and next-to-leading order (NLO) events. The LO sample reproduces the p_{T} spectrum for low momenta well and not so well in the high momentum regime, while the opposite is true for the NLO sample. There should be some overlap between the two samples in the intermediate region. To match the distributions the number NLO events has been scaled down by the cross section ratio $R = \sigma_{LO}/\sigma_{NLO}$. The cross sections used for this ratio are obtained from MadEvent for the LO and NLO matrix elements and the resulting R-factor is 2.56. In the next step the intersection of the LO and scaled NLO $\log(p_{\mathrm{T}}(b_2))$ distributions was fit by using a neural network fitter. By this method an intersection of the two distributions was found at $log(K_{\mathrm{T}}/(1\ \mathrm{GeV/c}) = 2.89$ or $K_{\mathrm{T}} = 18.0\ \mathrm{GeV}/c$. The logarithm was used for this procedure to stabilize the fit result. The match t-channel sample is then constructed by:

- Combination of the LO and NLO events in the proportion R
- Selection of the subset LO events with $p_{\mathrm{T}}(b_2) < K_{\mathrm{T}}$
- Selection of the subset NLO events with $p_{\mathrm{T}}(b_2) > K_{\mathrm{T}}$

By this matching algorithm the transverse momentum distribution of the "second" bottom quark fits well the theoretical predictions for this distribution without harming the distributions for the top decay products. A more detail description of the mixing process is documented in Ref. [70].

The matching algorithm was applied to the MadEvent and the TopRex samples. Table 4.1 gives an overview on the signal samples used in this analysis..

MadEvent Samples, all with $W \to e, \mu, \tau$

Sample	Process	Description	N gen.
mtop0s	t-channel	LO $2 \to 2$	156606
mtop1s	t-channel	NLO $2 \to 3$	198903
mtop2s	s-channel	LO	199953

TopRex Samples, all with $W \to e, \mu, \tau$

Sample	Process	Description	N gen.
rtop0s	t-channel	TopRex L0; $W \to e, \mu, \tau$	199803
rtop1s	t-channel	TopRex NLO; $W \to e, \mu, \tau$	199459
rtop2s	s-channel	TopRex LO; $W \to e, \mu, \tau$	200107

Pythia Samples, all W decay modes

Sample	Process	Description	N gen.
ttop0s	t-channel	standard, no filter	499189
ttop1s	s-channel	standard, no filter	440000

Table 4.1: Monte Carlo samples used in the single top analysis.

4.2 Single Top Event Selection

In order to separate the single top quark events from the background, it is necessary to reconstruct these events to a high precision. Therefore additional requirements are imposed on the collider data with respect to the trigger requirements. This section describes the event selection requirements used throughout this analysis. The signature of single top events is given by the leptonic decay products of the W originating from the top decay, i.e. an isolated lepton and missing transverse energy. In addition to that, one expects hadronic jets, from which at least one should be an identified b jet.

4.2.1 Primary Vertex

The first requirement imposed on the events is a primary vertex in the fiducial volume of the detector. This builds the starting point of the event selection for simulated events:

$$|z_0| < 60 \text{ cm } (\texttt{fabs(TN->obsp\_Vz[0])<60.0})$$

For data a correction factor is applied. As already mentioned in the previous chapter the *TopNtuples* data format has been used in this analysis. The implementation of this requirement within the root framework is given in brackets. The next step is the lepton identification.

4.2.2 Lepton Identification

Since throughout this analysis the high-p_{T} lepton trigger samples are used, the lepton identification requirements are the starting point of the refinement of the event selection.

For the single top signals high-p_{T}, isolated leptons originating from the leptonic W boson decay are expected. In this analysis only triggered electrons and muons are used. Tau leptons also contribute to acceptance via decay to a muon or a electron and the corresponding neutrinos. The tightened electron selection criteria along with the corresponding TopNtuple implementation are given in Table 4.2. The electron selection requires an electromagnetic cluster with $E_{\mathrm{T}} > 20$ GeV matched to a track with transverse momentum greater than 10 GeV. The electromagnetic fraction and the shape of the shower of the cluster are demanded to be consistent with an electron signature. The assigned extrapolated track pointing to the location of the electromagnetic shower maximum is required to match a momentum consistent with the measured shower energy. Finally the energy deposition in a cone of radius $\Delta R = 0.4$ around the cluster, excluding the cluster itself, is determined and the ratio of this energy to the cluster energy is required to be less than 0.1. This is the isolation criterion. To suppress backgrounds due to photon conversions in the detector material into electrons and positrons, events are rejected if an oppositely charged track is to be found nearby the electron candidate track.

Table 4.3 shows the cuts applied to identify muons. The muon selection requires a COT track with transverse momentum greater than 20 GeV/c matching a CMUP or CMX muon stub. The matching procedure is based on the extrapolated track position at the location of the muon chambers after correcting for multiple scattering. The energy deposit in the calorimeter tower containing the muon candidate is required to be consistent with the signature of a minimum ionizing particle. Backgrounds from cosmic rays are removed by demanding that the track fits to the primary vertex position and that the minimum ionizing energy deposit in the tower is within a narrow timing window around the beam crossing. Unfortunately, certain quantities used for cosmic ray background rejection are not well modeled by the Monte Carlo detector simulation. Therefore, the cosmic rejection was not applied to the Monte Carlo samples. The signal loss for W+2 jet events was estimated from data and is 1.23%. [72]. This has to be accounted for as an additional factor in the event detection efficiency when using Monte Carlo samples.

Selection Cut	TopNtuple Implementation
CEM electron	`TN->electron_Region[ne]==0`
Fiducial	`TN->electron_Fiducial[ne]==1`
$E_T \geq 20.0$ GeV	`TN->electron_Et[ne]>=20.0`
$p_T \geq 10.0$ GeV	`TN->electron_TrkPt[ne]>=10.0`
$E_{had}/E_{em} \leq 0.055 + 0.00045E$	`TN->electron_Hadem[ne]<=(0.055+0.00045*` `TN->electron_En[ne])`
$L_{shr} \leq 0.2$	`TN->electron_LshrTrk[ne]<=0.2`
$E/P \leq 2.0$ .OR. $p_T > 50$ GeV	`TN->electron_EP[ne]<=2.0 ||` `TN->electron_TrkPt[ne]>50.0`
$\|z_0\| \leq 60.0$ cm	`fabs(TN->electron_TrkZ0[ne])<=60.0`
$\|\Delta z\| \leq 3.0$ cm	`fabs(TN->electron_DeltaZ[ne])<=3.0`
$-3.0 \leq Q \cdot \Delta x \leq 1.5$ (cm)	`qd=((float)TN->electron_Charge[ne])*` `TN->electron_DeltaX[ne];` `qd >= -3.0 && qd <= 1.5`
$\chi^2_{strip} \leq 10.0$	`TN->electron_StripChi2[ne]<=10.0`
Good COT Axial Segments≥ 3	`TN->electron_TrkAxSeg[ne]>=3`
Good COT Stereo Segments≥ 3	`TN->electron_TrkStSeg[ne]>=3`
Isolation ≤ 0.1	`TN->electron_Isol[ne]<=0.1`
Conversion Veto	`TN->electron_Conversion[ne]!=1`

Table 4.2: The baseline cuts for CEM electrons for Run 2 analyses (adapted from Ref. [71]).

Selection Cut	TopNtuple Implementation
CMUP muon	`(TN->muon_muontype[nm]&3)==3`
CMX muon	`(TN->muon_muontype[nm]&4)==4`
$p_T \geq 20.0$ GeV/c	`TN->muon_Pt[nm]>=20.0`
$E_{had} \leq max(6, 6 + 0.0280(p - 100))$	`TN->muon_HadEnergy[nm]<=6.0 ||` `(TN->muon_HadEnergy[nm]<=6.0+0.028` `*(TN->muon_P[nm]-100.0))`
$E_{em} \leq max(2, 2 + 0.0115(p - 100))$	`TN->muon_EmEnergy[nm]<=2.0 ||` `(TN->muon_EmEnergy[nm]<=2.0+0.0115` `*(TN->muon_P[nm]-100.0))`
$\|z_0\| \leq 60.0$ cm	`fabs(TN->muon_Z0[nm])<=60.0`
CMU$\|\Delta x\| \leq 3.0$ cm (CMUP only)	`fabs(TN->muon_CmuDx[nm])<=3.0`
CMP$\|\Delta x\| \leq 5.0$ cm (CMUP only)	`fabs(TN->muon_CmpDx[nm])<=5.0`
CMX$\|\Delta x\| \leq 6.0$ cm (CMX only)	`fabs(TN->muon_CmxDx[nm])<=6.0`
Good COT Axial Segments≥ 3	`TN->muon_TrkAxSeg[nm]>=3`
Good COT Stereo Segments≥ 3	`TN->muon_TrkStSeg[nm]>=3`
$\|d_0\| \leq 0.2$ cm if no Si hits	`TN->muon_TrkSiHits[nm]==0 &&` `fabs(TN->muon_D0[nm])<=0.2`
$\|d_0\| \leq 0.02$ cm if Si hits	`TN->muon_TrkSiHits[nm]!=0 &&` `fabs(TN->muon_D0[nm])<=0.02`
Isolation ≤ 0.1	`TN->muon_Isol[nm]<=0.1`
Cosmic Veto (for data only)	`cv=(TN->summary_fTopEventClass[0])` `(cv&0x20)==0`

Table 4.3: The baseline cuts for CMUP and CMX muons for Run 2 analyses (adapted from Ref. [71]). The cosmic veto is only applied to data, not to Monte Carlo events.

4.2.3 Dilepton Veto

Since in single top events only one high-p_{T} lepton originating from the leptonic W decay is expected, events are rejected where more than one of these tight leptons are found. Nevertheless one expects to see rather soft electrons and muons originating from semi-leptonic b decays.

$$N_{\text{tight lepton}=1} \quad (\texttt{TN->summary\_fnTightLepton[0]==1})$$

To improve this dilepton veto also forward electrons are considered. These so-called "PHX" electrons are not accepted as a trigger lepton, but they can be

very efficiently used to suppress backgrounds. (Here denoted as "PHX" veto.) These electrons are found by a colorimeter seeded tracking algorithm. The seeds are clusters in the forward (plug) electromagnetic calorimeters.

4.2.4 Z Boson Veto

To suppress backgrounds due to leptonic Z+jets production, events are rejected in which a combination of the identified tight lepton and a loosely identified lepton forms an invariant mass, that falls in the window of

$$76 \text{ GeV}/c^2 < M_{\ell\ell} < 106 \text{ GeV}/c^2$$

`(TN->summary_fTopEventClass[0]&0x8)==0`.

around the Z boson mass. For muons this loosely identified lepton is an opposite-signed isolated track with $p_{\mathrm{T}} > 10$ GeV/c. For primary electrons the lepton candidate may be such a track, an electromagnetic cluster or a jet with $E_{\mathrm{T}} > 15$ GeV and $|\eta| \leq 2.0$ that has less than three tracks assigned to the jet and an electromagnetic energy fraction greater than 95%.

4.2.5 Jet Selection and Jet Counting

The number of jets associated with the lepton originating from the W boson decay is measured by selecting jets of cone radius $\Delta R = 0.4$. In order to find these jets the JetClu algorithm was used. Additional requirements are corrected transverse energy $E_{\mathrm{T}} > 15$ GeV and $|\eta_{\mathrm{detector}}| \leq 2.8$. The jets have been clustered after removal of the towers assigned to the selected isolated lepton from the leptonic W decay and after a correction of the measured transverse energy in the towers for the location of the primary vertex. The pseudorapidity η_{detector} is the pseudorapidity coordinate of the calorimeter tower with respect to the origin of the coordinate system, the center of the detector.

All clustered jets to be found in one event are corrected if the uncorrected assigned transverse energy $E_T(\mathrm{raw}) \geq 8$ GeV and the pseudorapidity assigned to the jet axis in the detector coordinates $|\eta_{\mathrm{detector}}| \leq 2.8$. This preselection has to be performed since the corrections are only well-defined for this regime. At the stage of jet counting corrections up to level 4 are applied. Level 4 corresponds to applying relative energy, time-dependence, energy scale and multiple-interactions corrections as explained in section 3.6.2.
The reason for counting jets up to a pseudorapidity $|\eta_{\mathrm{detector}} = 2.8|$ accounts for the fact that in t-channel single top events the light flavor jet is emitted in forward direction. By this extension the acceptance for t-channel events is increased about 30%, while the s-channel acceptance remains essentially unchanged (+2%) and the backgrounds increase only moderately. In addition to this "tight" jet

selection for specific purposes we also consider a "loose" jet selection. Here the jets are required to have a corrected transverse energy $E_{\mathrm{T}} > 8$ GeV and $|\eta_{\mathrm{detector}}| \leq 2.8$.

4.2.6 $\not\!\!E_{\mathrm{T}}$ Selection Requirements

To select leptonic W boson events the missing transverse energy of the events is required to fulfill corrected $\not\!\!E_T \geq 20$ GeV. This selection criterion corresponds to the signature of the neutrino associated with the high momentum lepton from the W boson decay.

$\not\!\!E_T$ is calculated as the vector sum of the energy in each calorimeter tower multiplied by the azimuthal direction of the tower. If the identified lepton of such an event is a muon, $\not\!\!E_T$ is corrected by subtraction of the muon energy deposit in the calorimeter and by addition of the transverse muon momentum to the vector sum. This has to be done since a muon does not create a shower in the calorimeter, but deposits the energy of a minimal ionizing particle. Thus, without applying this correction $\not\!\!E_T$ would be artificially generated. Since corrected jet energies are used for the jet counting, one needs to correct $\not\!\!E_T$ to be consistent. So therefore the difference between the corrected and the uncorrected jet energies was calculated $\Delta E_T = E_T(\mathrm{raw}) - E_T(\mathrm{corr.})$ and added vectorially to the to $\not\!\!E_T$.
For the collider data an additional correction to the muon transverse momentum is applied and added vectorially to $\not\!\!E_T$: $\Delta P_T = P_T(\mu;\ \mathrm{raw}) - P_T(\mu;\ \mathrm{corr.})$ This correction is due to a systematic mismeasurement of the muon momentum.

4.2.7 B-tag Requirements

At least one jet must be identified as likely to contain a b hadron. Thus, at least one *SecVtx* tagged jet is required.

$$N_{btag} \geq 1 \quad (\texttt{TN->jet\_secvTag[nj]==1}).$$

The b-tagging relies on the reconstruction of displaced secondary vertices with the silicon micro-strip detector. Secondary vertices with a transverse decay length significance ($\Delta L_{xy}/\sigma_{xy}$) above 3 are accepted as a b-tag for jets.
For consistency we require that the charged lepton z_0 is within a window of 5 cm around the primary vertex used for b-tagging.("Z Vertex" requirement).

Figure 4.2 shows the jet multiplicity for s- and t-channel MadEvent Monte Carlo events after all imposed selection requirements described in this section. The large majority of single top events populates the 2-jet bin.

In this section the general selection requirements used for this analysis have been presented. Since the expected background are rather huge for such an

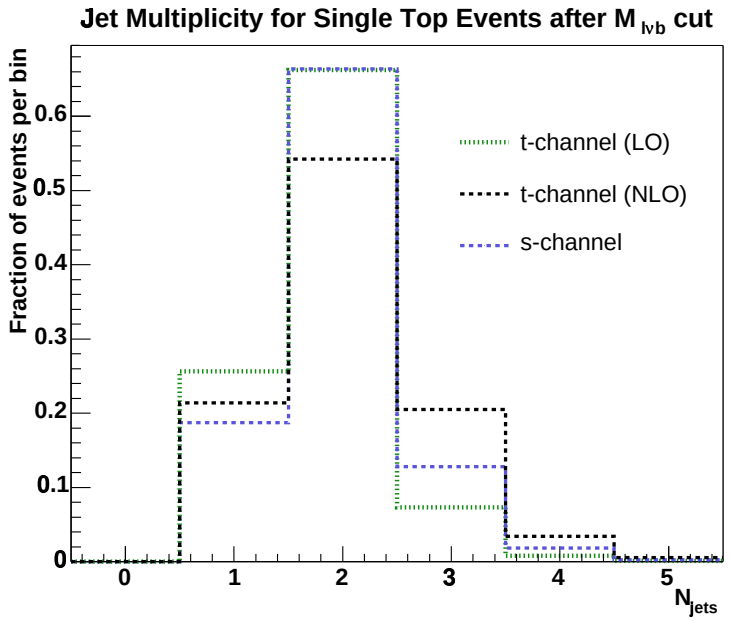

Figure 4.2: Jet multiplicity distribution after b-tag for MadEvent LO, NLO t-channel and s-channel events.

analysis and one of the goals of this analysis is to separate s- and t-channel single top events from each other, additional requirements have to be imposed.

4.3 Additional Requirements

As depicted in figure 4.2, the bulk number of single top events is to be found in the 2-jet bin. Therefore, this analysis will focus on the 2-jet subsample. A distinct feature of t-channel production is that the vast majority of events will have exactly one visible b-jet in the detector, whereas the s-channel production events will have 2 b jets. But due to a limited tagging efficiency and geometrical acceptance of the detector, part of the s-channel events will populate the 1-tag and the 2-tag sample. The number of expected t-channel events in the 2-tag subsample is almost negligible.
The reconstruction of the invariant mass of the lepton, the neutrino candidate and the bottom jet is highly correlated to the top quark mass and a useful discriminant for signal and background. In the following subsection the reconstruction algorithm for the kinematic mass M_{lvb} is presented.

4.3.1 Top Mass Reconstruction

One important requirement to establish the production of a certain elementary particle is to reconstruct one of its most distinct features, its rest mass. In the Standard Model top quark decay is dominated by the mode $t \to b + W$, which has a branching ratio close to 100%. In our analysis we reconstruct leptonic W boson decays. We therefore reconstruct $M_{\ell\nu b}$ as an estimator for $m_{\rm top}$.

b-jet assignment: The first step to calculate the top quark mass is to reconstruct the b-quark 4-momentum vector. The event selection criteria require at least one b-tagged jet be present. If there is one and only one b-tagged jet in the event, this jet is used for top mass reconstruction. If there are more b-tagged jets, the b-jet is chosen which has maximum $Q \cdot \eta$. Q is the lepton charge (in units of the elementary charge e) and is used to tag top and antitop events. η is the pseudo-rapidity of the b-jet. The b-jet 3-momentum vector $\vec{p}$ is corrected by a scale factor obtained from the jet corrections. In this case jet corrections up to level 7 are used, which includes all available corrections. We set the b-jet mass to $m_{\rm b-jet} = 5$ GeV/c^2, and calculate the energy: $E_b^2 = m_{\rm b-jet}^2 + \vec{p}^2$.

The second step is to reconstruct the W boson 4-momentum. The event selection is such that one and only one tight charged lepton (e or μ) will be found. The lepton four-momentum is very well reconstructed by CDF. The neutrino remains undetected. In reasonably good approximation the transverse momentum, $p_{\rm T}$, of the neutrino is given by the missing transverse energy $\not\!\!E_T$, as obtained from calorimeter information. To improve the precision on the $\not\!\!E_T$ measurement corrections are applied. For events containing a muon, a correction due to the mismeasurement of the muon transverse momentum is applied as described in section4.2.The second correction is due to the jet energy measurement. The jet energy correction, however, has to be consistent with the fact that level 7 corrections are used for the b-jet. In contrast to the $\not\!\!E_T$ corrections described in section 4.2 correction level 6 are used for the jets to calculate the corrected $\not\!\!E_T$. Level 7 corrections are not used because they include out-of-cone corrections. Using them in the $\not\!\!E_T$ calculation would mean a double-counting of out-of-cone energies.

Calculating the neutrino $\mathbf{p_z}$ component: The z-component of the neutrino momentum is unknown. However, under the assumption that the events contain W boson decaying leptonically, the neutrino p_z can be calculated up to a two-fold ambiguity using the following kinematic constraints:

$$p_\mu(W) = p_\mu(\ell) + p_\mu(\nu) \qquad\qquad p_\mu(\nu)\, p^\mu(\nu) = 0 \tag{4.2}$$

Solving for $p_z(\nu)$ gives:

$$p_z(\nu) = \frac{\kappa\, p_z(\ell)}{E^2(\ell) - p_z^2(\ell)} \pm \frac{1}{2\left(E^2(\ell) - p_z^2(\ell)\right)} \cdot\sqrt{\left(2\kappa p_z(\ell)\right)^2 - 4\left(E^2(\ell)p_T^2(\nu) - \kappa^2\right)\cdot\left(E^2(\ell) - p_z^2(\ell)\right)} \tag{4.3}$$

$$\text{with} \quad \kappa = 0.5\left(M_W^2 - m_\ell^2\right) + \cos\left(\phi_\ell - \phi_\nu\right)\cdot p_T(\ell)\, p_T(\nu) \tag{4.4}$$

For the calculation $p_T(\nu) = \not{E}_T$ is used. Out of the two solutions the one which has the smallest absolute value was chosen. In contrast to prompt W boson production the neutrinos produced in top decays via the W decay are rather central. If the p_z turns out to be complex with non-zero imaginary part (the expression beneath the square root is negative) only the real part of p_z was used. That happens in about 30% of the cases according to the Monte Carlo samples due to detector mismeasurements. This is fully compatible with the detector resolution. The following masses have been used: $M_W = 80.448$ GeV/c^2, $m_\mu = 0.106$ GeV/c^2 and $m_e = 0.511$ MeV/c^2 . The neutrino energy is calculated using:

$$E(\nu) = \sqrt{\not{E}_T{}^2 + p_z^2}\,. \tag{4.5}$$

$M_{\ell\nu b}$ which for signal events estimates the top quark mass is then calculated by four-vector addition of the charged lepton, the neutrino candidate and the assigned b-jet .

Figure 4.3 shows the $M_{\ell\nu b}$ distribution for s- and t-channel single top MadEvent Monte Carlo data after application of the event selection criteria.

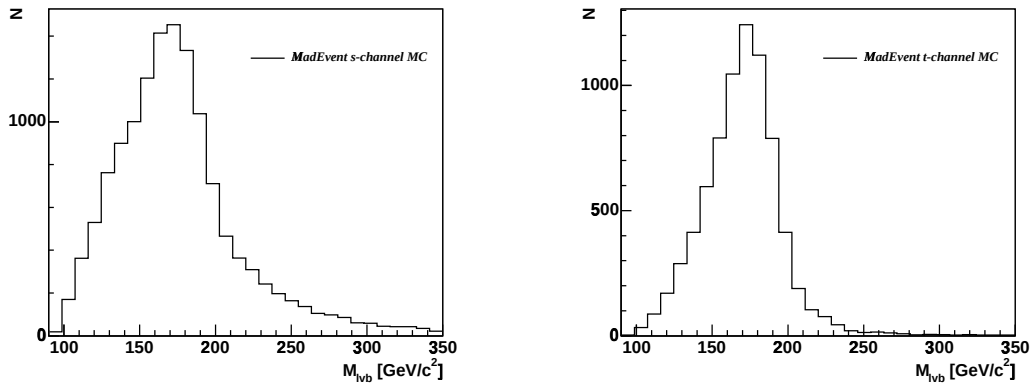

Figure 4.3: $M_{\ell\nu b}$ distribution for s- and t-channel single top MadEvent Monte Carlo data after application of the event selection criteria.

4.3.2 $M_{\ell\nu b}$ Requirements

Imposing requirements on M_{lvb} is a powerful tool to suppress backgrounds involving prompt W bosons. Since the vast majority of 2-jet single top events is to be found in the window 140 GeV/c^2 < $M_{\ell\nu b}$ < 210 GeV/c^2 this requirement is used.

4.3.3 The Leading Jet Requirement

In addition to the $M_{\ell\nu b}$ requirement the jet with the greatest transverse energy is demanded to exceed a transverse energy of 30 GeV if one and only one b-tagged jet was found in this event. Figure 4.4 shows the leading jet E_{T} distribution after application of the $M_{\ell\nu b}$ requirement for s- and t-channel single top MadEvent Monte Carlo.

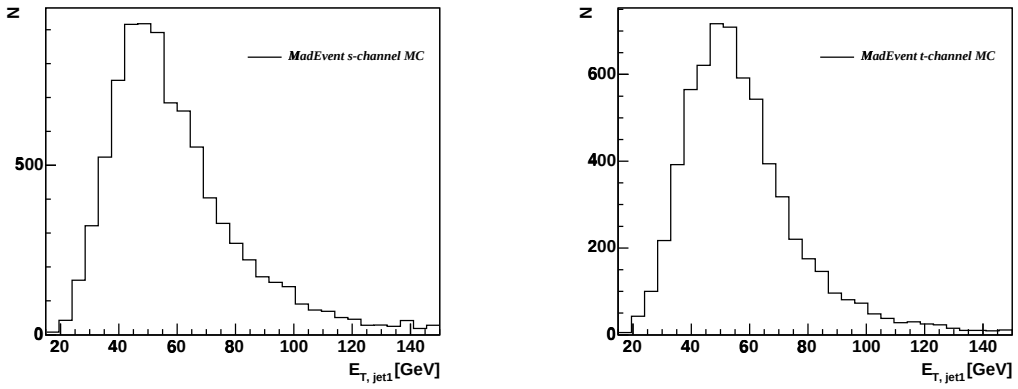

Figure 4.4: E_{T} distribution for s- and t-channel single top MadEvent Monte Carlo events after application of the event selection criteria including the $M_{\ell\nu b}$ requirement.

Table 4.4 shows the cutflow for t-channel MadEvent Monte Carlo events after application of each cut presented in this chapter. The number of Monte Carlo generated events is given in the line named `Total`. First events are selected which have the primary vertex (here:OBSV) in the fiducial volume of the CDF detector: $|z_0| < 60$ cm. The next step is the lepton identification. We require one and only one tight lepton per event, which we call `Dilepton Veto`. After the dilepton veto the events are subdivided in three categories according to the subsystem where the tight lepton was detected: `CEM`, `CMUP` and `CMX`. Events are rejected which have an additional Phoenix electron in the plug, `PHX Veto`. For CEM events there is an additional `conversion veto`. In addition the Z^0 veto

is applied. The number of events passing the requirement $\not\!\!E_T \geq 20$ GeV is given in the line `Missing Et`. The number of events that have a positive tag for at least one taggable jet is given in the line denoted `b tag` $\geq$ `1`. The final requirement concerns the reconstructed top quark mass $M_{l\nu b}$, and retains only events in which 140 GeV/c^2 $< \mathrm{M_{l\nu b}} <$ 210 GeV/c^2. For the exactly 1-btag subsample an additional cut is applied: At least one jet is required to have $E_T > 30$ GeV.

Cut	0 jet	1 jet	2 jet	3 jet	4 jet	≥ 5 jets	all
Total	3013	37733	82673	33931	5072	815	163237
OBSV < 60.0	2925	36682	80173	32425	4853	774	157832
≥ 1 lepton	852	10358	20377	2862	428	58	34935
CEM electrons							
Dilepton Veto	457	5879	11583	1580	235	35	19769
PHX Veto	455	5876	11580	1579	235	35	19760
Z Vertex Cut	455	5876	11579	1579	235	35	19759
Conversion veto	452	5863	11545	1574	235	35	19704
Z veto	449	5801	11349	1545	230	35	19409
Missing Et	421	5202	10259	1402	201	30	17515
b tag ≥ 1	0	1663	4251	692	119	13	6738
$140 \leq M_{b\ell\nu} \leq 210$	0	1385	3563	487	70	10	5515
$\mathsf{E_T(Jet1)} \geq 30$ GeV	0	1283	3442	478	69	10	5282
CMUP muons							
Dilepton Veto	269	3209	6426	941	133	17	10995
PHX Veto	269	3206	6425	941	133	17	10991
Z Vertex Cut	269	3206	6425	941	133	17	10991
Z veto	266	3192	6375	933	131	17	10914
Missing Et	246	2839	5708	836	115	17	9761
b tag ≥ 1	0	893	2394	395	67	8	3757
$140 \leq M_{b\ell\nu} \leq 210$	0	755	1999	280	34	6	3074
$\mathsf{E_T(Jet1)} \geq 30$ GeV	0	703	1954	274	32	6	2969
CMX muons							
Dilepton Veto	124	1266	2368	341	60	6	4165
PHX Veto	124	1262	2368	341	60	6	4161
Z Vertex Cut	124	1262	2368	341	60	6	4161
Z veto	124	1253	2351	340	58	6	4132
Missing Et	114	1109	2055	296	50	6	3630
b tag ≥ 1	0	351	859	146	27	6	1389
$140 \leq M_{b\ell\nu} \leq 210$	0	280	723	94	17	4	1118
$\mathsf{E_T(Jet1)} \geq 30$ GeV	0	255	696	91	17	4	1063

Table 4.4: Cut flow table of single top event selection for t-channel single top-quark Monte Carlo events.

4.4 Event Detection Efficiency

The final aim of this analysis is to calculate the single top quark production cross section σ_{st}. The calculation is based on the following formula:

$$\sigma_{st} = \frac{N_{\text{signal}}}{\epsilon_{\text{evt}} \cdot \int \mathcal{L}\, dt} \tag{4.6}$$

Here N_{signal} is the number of observed signal events, which is obtained for example from a maximum likelihood fit. ϵ_{evt} is the event detection efficiency which is the average probability of a single top event to be detected, i.e. to be found in our selected candidate sample. $\int \mathcal{L}\, dt$ is the integrated luminosity, which will be abbreviated as $\mathcal{L}_{\text{int}}$ in the paragraphs below.

At the current stage the integrated luminosity of CDF is not high enough to make a measurement of σ_{st} which is significantly different from 0. Therefore, an upper limit on the cross-section will be set. For this (4.6) is not directly used. However, (4.6) can be used to calculate the number of expected signal events. For this purpose it takes the form:

$$N_{\text{signal}}^{\text{predict}} = \sigma_{\text{st}}^{\text{theo}} \cdot \epsilon_{\text{evt}} \cdot \mathcal{L}_{\text{int}} \tag{4.7}$$

In this section the calculation of ϵ_{evt}, the event detection efficiency, is described. This is done using the Monte Carlo samples listed in Tab. 4.1.
ϵ_{evt} can be decomposed into 4 factors:

$$\epsilon_{\text{evt}} = \epsilon_{\text{evt}}^{\text{MC}} \cdot \epsilon_{\text{BR}} \cdot \epsilon_{\text{corr}} \cdot \epsilon_{\text{trig}} \tag{4.8}$$

Here $\epsilon_{\text{evt}}^{\text{MC}}$ is the event detection efficiency as obtained from our samples of simulated events by applying the event selection criteria. In some of these samples the W boson was only allowed to decay into leptons: $W \to e/\mu/\tau + \nu$. This has to be taken into account by applying the factor $\epsilon_{\text{BR}} = 0.3204$ [6]. This factor accounts for the leptonic branching ratios. ϵ_{corr} is a correction factor which takes into account the difference between simulated and data events. ϵ_{corr} gives a measure of how well the Monte Carlo simulation models the detector. ϵ_{trig} is the trigger efficiency. The correction factor is again composed out of several parts:

$$\epsilon_{\text{corr}} = \frac{\epsilon_{z0}^{\text{data}}}{\epsilon_{z0}^{\text{MC}}} \cdot \frac{\epsilon_{\text{leptonid}}^{\text{data}}}{\epsilon_{\text{leptonid}}^{\text{MC}}} \cdot \frac{\epsilon_{\text{reco}}^{\text{data}}}{\epsilon_{\text{reco}}^{\text{MC}}} \cdot \frac{\epsilon_{\text{tag}}^{\text{data}}}{\epsilon_{\text{tag}}^{\text{MC}}} \tag{4.9}$$

Since trigger and identification efficiencies and available luminosities vary for the different subdetectors used in this analysis (i.e.: CEM, CMU/CMP and CMX), three different cases have to be distinguished: $\epsilon_{\text{evt}}^{\text{CEM}}$, $\epsilon_{\text{evt}}^{\text{CMUP}}$ and $\epsilon_{\text{evt}}^{\text{CMX}}$. The determination of $\epsilon_{\text{evt}}^{\text{MC}}$ from Monte Carlo simulations will be discussed in the next section. The following values for the trigger efficiencies and reconstruction and identification scale factors have been measured using CDF II data [73, 74, 75]:

Efficiencies	CEM	CMUP	CMX
Trigger ($\epsilon_{\rm trig}$)	0.9656 ± 0.0006	0.887 ± 0.007	0.954 ± 0.006
ID s. f. ($\epsilon_{\rm ID}$)	0.965 ± 0.006	0.939 ± 0.007	1.014 ± 0.007
Reco s. f. ($\epsilon_{\rm reco}$)	1.0 per def.	0.945 ± 0.006	0.992 ± 0.003

Table 4.5: Electron and muon trigger efficiencies and ID efficiency scale (correction) factors for 200 pb^{-1}.

- $\epsilon_{z0}^{data} = 0.951 \pm 0.001 \pm 0.005$ is the z vertex cut efficiency in data [76]. In Monte Carlo we obtain $\epsilon_{z0}^{MC} = 0.965 \pm 0.003(stat.)$ for the MadEvent and TopRex samples and $\epsilon_{z0}^{MC} = 0.967 \pm 0.003(stat.)$ for the Pythia samples ttop0s and ttop1s. The correction factors therefore are: $\epsilon_{z0}^{data}/\epsilon_{z0}^{MC} = 0.986 \pm 0.006$ and $\epsilon_{z0}^{data}/\epsilon_{z0}^{MC} = 0.983 \pm 0.006$.

- The b-tagging efficiency differs between data and Monte Carlo. Therefore, the acceptance calculation has to be corrected since it is based on Monte Carlo events. $\epsilon_{tag-jet}^{data}/\epsilon_{tag-jet}^{MC} = 0.82 \pm 0.06$ is the correction factor for b-tagging efficiency [77] see section 3.7.2. This correction factor is valid per tagged b-jet. If a Monte Carlo sample contained only events with one and only one b-jet per event, the factor would be applicable globally. However, since there are also double-tag events the global correction factor has to be determined. One method is the counting method as described in Ref. [78]. This method is applied to the Monte Carlo samples. Each b-tagged jet is considered individually. Randomly $1 - \epsilon_{\rm tag}^{\rm data}/\epsilon_{\rm tag}^{\rm MC} = 18\%$ of the jets are discarded and the remaining events with at least one b-jet are counted. The results on the global correction factor $K = \epsilon_{\rm tag,global}^{\rm data}/\epsilon_{\rm tag,global}^{\rm MC}$ are given in Table 4.6 for 3 cases: (1) 1 or 2 b-tags (K_{12}), (2) exactly 1 b-tag (K_1), (3) exactly 2 b-tags (K_2).

For the t-channel K_{12} and K_1 are only little higher than 82%, since there is only one central high-p_T b-jet in the event. For the s-channel the correction factor is about 88% because there are two b-jets in the event.

4.4.1 Determination of $\epsilon_{\rm evt}^{\rm MC}$

The determination of the event detection efficiency is based on Monte Carlo events. All selection and identification criteria are applied to the simulated data. Table B.1 in the appendix summarizes the number of remaining events in the 2-jet bin after application of the following requirements:

- After requiring at least one b-tagged jet in the event (N_{btag})

B-tag Efficiencies				
Process	Sample	K_{12}	K_1	K_2
t-chan.	mtop0s/1s	0.8255	0.8304	0.6396
s-chan.	mtop2s	0.8489	0.891	0.6808
t-chan.	rtop0s/1s	0.8291	0.8394	0.6661
s-chan.	rtop2s	0.8503	0.894	0.6741
t-chan.	ttop1s	0.8215	0.8229	0.7229
s-chan.	ttop0s	0.8543	0.9021	0.6628

Table 4.6: Correction factor for b-tagging efficiency of the various single top samples.

- After requiring exactly one b-tagged jet in the event ($N_{btag=1}$)
- After the $M_{\ell\nu b}$ cut if at least one b-tag is assigned to the event
- After the additional cut on the leading jet in E_T (N_{jet1}) and the $M_{\ell\nu b}$ cut,
- After $M_{\ell\nu b}$ cut in the 1-b-tag bin (N_{1tag})
- After the $M_{\ell\nu b}$ and E_T(jet1) cut in the 1-b-tag bin ($N_{1tag,ET}$)
- After $M_{\ell\nu b}$ cut in the 2-b-tag bin (N_{2tag}).

All these scenarios are given since based on these numbers the analysis was optimized. Using the numbers in Table B.1 given in the appendix the Monte Carlo derived event detection efficiency $\epsilon_{\text{evt}}^{\text{MC}}$ is calculated. Table B.2 list the results of this calculation.

4.4.2 Determination of ϵ_{evt}

To convert $\epsilon_{\text{evt}}^{\text{MC}} \cdot \epsilon_{\text{BR}}$ into ϵ_{evt} one needs to calculate ϵ_{corr} first. This has to be done for each sample separately, since the b-tagging efficiency per event depends on the sample. To cover the different cut scenarios the numbers for (1) more than 1 b-tag, (2) exactly 1 b-tag and (3) exactly two b-tags are given. The assigned errors on ϵ_{corr} are calculated by adding the relative errors on $\epsilon_{\text{z0}}^{\text{data}}/\epsilon_{\text{z0}}^{\text{MC}}$, $\epsilon_{\text{leptonid}}^{\text{data}}/\epsilon_{\text{leptonid}}^{\text{MC}}$, $\epsilon_{\text{reco}}^{\text{data}}/\epsilon_{\text{reco}}^{\text{MC}}$ and $\epsilon_{\text{tag}}^{\text{data}}/\epsilon_{\text{tag}}^{\text{MC}}$. The results on ϵ_{corr} including the errors are presented in Tab. 4.7.

After calculation of ϵ_{corr} one can now compute ϵ_{evt} based on (4.8). The result is presented in Table 4.8.

Correction Factor Monte Carlo to Data						
	MadEvent		TopRex		Pythia	
Sample	t-chan.	s-chan.	t-chan.	s-chan.	t-chan.	s-chan.
Sample	mtop0s/1s	mtop2s	rtop0s/1s	rtop2s	ttop1s	ttop0s
CEM Electrons						
btag ≥ 1	0.784±0.058	0.807±0.059	0.786±0.058	0.809±0.060	0.780±0.057	0.811±0.060
btag == 1	0.788±0.058	0.847±0.062	0.796±0.059	0.850±0.063	0.781±0.058	0.856±0.063
btag == 2	0.607±0.045	0.648±0.048	0.632±0.047	0.641±0.047	0.686±0.051	0.629±0.046
CMUP Muons						
btag ≥ 1	0.720±0.053	0.742±0.055	0.723±0.054	0.744±0.055	0.717±0.053	0.745±0.055
btag == 1	0.725±0.054	0.779±0.058	0.732±0.054	0.782±0.058	0.718±0.053	0.787±0.058
btag == 2	0.558±0.041	0.595±0.044	0.581±0.043	0.590±0.044	0.631±0.047	0.578±0.043
CMX Muons						
btag ≥ 1	0.817±0.060	0.842±0.062	0.820±0.061	0.843±0.062	0.813±0.060	0.845±0.062
btag == 1	0.822±0.061	0.883±0.065	0.830±0.061	0.886±0.065	0.814±0.060	0.892±0.066
btag == 2	0.633±0.047	0.675±0.050	0.659±0.049	0.668±0.049	0.715±0.053	0.656±0.048

Table 4.7: ϵ_{corr} for single top Monte Carlo samples.

Event Detection Efficiency in %						
	MadEvent		TopRex		Pythia	
Process	t-chan.	s-chan.	t-chan.	s-chan.	t-chan.	s-chan.
Sample	mtop0s/1s	mtop2s	rtop0s/1s	rtop2s	ttop1s	ttop0s
CEM Electrons						
ϵ_{btag}	0.631±0.048	0.963±0.073	0.568±0.044	0.920±0.069	0.590±0.044	0.812±0.061
$\epsilon_{\mathsf{btag=1}}$	0.627±0.047	0.761±0.056	0.567±0.043	0.734±0.055	0.588±0.044	0.661±0.049
$\epsilon_{\mathsf{M}\ell\nu\mathsf{b}}$	0.529±0.040	0.633±0.048	0.466±0.036	0.612±0.046	0.491±0.037	0.539±0.041
ϵ_{jet1}	0.511±0.039	0.613±0.046	0.450±0.035	0.594±0.045	0.478±0.036	0.523±0.040
ϵ_{1tag}	0.527±0.040	0.483±0.037	0.468±0.036	0.477±0.036	0.490±0.037	0.423±0.032
$\epsilon_{\mathsf{1tag,ET}}$	0.509±0.039	0.466±0.036	0.452±0.035	0.460±0.035	0.477±0.036	0.408±0.031
ϵ_{2tag}	0.004±0.001	0.138±0.011	0.003±0.001	0.126±0.010	0.002±0.000	0.107±0.009
CMUP Muons						
ϵ_{btag}	0.300±0.023	0.449±0.035	0.297±0.023	0.454±0.035	0.309±0.024	0.414±0.032
$\epsilon_{\mathsf{btag=1}}$	0.298±0.023	0.356±0.027	0.297±0.022	0.369±0.028	0.308±0.023	0.341±0.026
$\epsilon_{\mathsf{M}\ell\nu\mathsf{b}}$	0.251±0.020	0.290±0.023	0.241±0.019	0.305±0.024	0.253±0.020	0.274±0.021
ϵ_{jet1}	0.245±0.019	0.281±0.022	0.235±0.019	0.297±0.023	0.246±0.019	0.266±0.021
ϵ_{1tag}	0.250±0.020	0.224±0.018	0.241±0.019	0.241±0.019	0.252±0.020	0.217±0.017
$\epsilon_{\mathsf{1tag,ET}}$	0.245±0.019	0.216±0.017	0.235±0.019	0.234±0.018	0.245±0.019	0.211±0.017
ϵ_{2tag}	0.002±0.000	0.061±0.005	0.003±0.001	0.060±0.005	0.001±0.000	0.053±0.005
CMX Muons						
ϵ_{btag}	0.131±0.011	0.203±0.016	0.130±0.011	0.213±0.017	0.135±0.011	0.205±0.016
$\epsilon_{\mathsf{btag=1}}$	0.130±0.010	0.164±0.013	0.130±0.010	0.177±0.014	0.134±0.010	0.167±0.013
$\epsilon_{\mathsf{M}\ell\nu\mathsf{b}}$	0.111±0.009	0.135±0.011	0.108±0.009	0.140±0.011	0.115±0.009	0.139±0.011
ϵ_{jet1}	0.106±0.009	0.130±0.011	0.105±0.009	0.135±0.011	0.111±0.009	0.135±0.011
ϵ_{1tag}	0.110±0.009	0.105±0.009	0.107±0.009	0.116±0.010	0.114±0.009	0.108±0.009
$\epsilon_{\mathsf{1tag,ET}}$	0.106±0.009	0.101±0.008	0.105±0.009	0.111±0.009	0.111±0.009	0.104±0.009
ϵ_{2tag}	0.001±0.000	0.028±0.003	0.001±0.000	0.024±0.002	0.000±0.000	0.029±0.003

Table 4.8: $\epsilon_{\mathsf{BR}} \cdot \epsilon_{\mathsf{evt}}^{\mathsf{MC}} \cdot \epsilon_{\mathsf{corr}} \cdot \epsilon_{\mathsf{trig}}$ for single top Monte Carlo samples.

4.4.3 Number of Expected Events

Since in this analysis the number of expected events is an important ingredient to derive upper boundaries on single top production, these numbers are finally calculated for the different scenarios. Using the values for ϵ_{evt} the number of expected events is calculated according to (4.7), the results are shown in Tab. 4.9 and in Tab. 4.10. The integrated luminosities for the CEM and CMUP trigger path used for this calculation adds up to 162 pb^{-1}. For the CMX 150 pb^{-1} of integrated luminosity has been used, due to an noncommissioned muon chamber in the early stage of Run II. The errors given here include the cross section prediction uncertainty of 13% and the uncertainty due to the luminosity measurement which is about 6% relative uncertainty. The numbers derived from the MadEvent samples will be used for the events yield, the differences to the numbers obtained by using PYTHIA and TopRex are used to estimate the uncertainties due to the choice of the single top production Monte Carlo generator.

All derived numbers for s- and t-channel are in good agreement. The slight differences are within the errors. After b-tagging, on average 3.4±0.6 t-channel events and 2.3±0.4 s-channel events are expected for an integrated luminosity of 162 pb^{-1}. The corresponding event detection efficiencies multiplied by the leptonic W decay branching ratios is about 1.06% for the t-channel and 1.60% for the s-channel.

Scenario	**MadEvent**	**TopRex**	**Pythia**
N_{btag}	2.29±0.37	2.24±0.36	2.02±0.33
$N_{\text{btag=1}}$	1.81±0.29	1.80±0.29	1.65±0.27
$N_{\text{M}\ell\nu\text{b}}$	1.50±0.24	1.50±0.24	1.35±0.22
N_{jet1}	1.45±0.24	1.45±0.24	1.31±0.21
N_{1tag}	1.15±0.19	1.18±0.19	1.06±0.17
$N_{\text{1tag,ET}}$	1.11±0.18	1.14±0.19	1.02±0.17
N_{2tag}	0.32±0.05	0.30±0.05	0.27±0.04

Table 4.9: Number of expected s-channel single top events derived from Monte Carlo samples.

Scenario	**MadEvent**	**TopRex**	**Pythia**
N_{btag}	3.37±0.55	3.15±0.51	3.29±0.54
$N_{\mathsf{btag=1}}$	3.35±0.54	3.15±0.51	3.26±0.53
$N_{\mathsf{M}\ell\nu\mathsf{b}}$	2.82±0.46	2.58±0.42	2.72±0.44
N_{jet1}	2.74±0.45	2.50±0.41	2.65±0.43
N_{1tag}	2.81±0.46	2.59±0.42	2.72±0.44
$N_{\mathsf{1tag,ET}}$	2.72±0.44	2.51±0.41	2.64±0.43
N_{2tag}	0.02±0.01	0.02±0.01	0.01±0.00

Table 4.10: Number of expected t-channel events derived form Monte Carlo samples.

Chapter 5

Background Estimate

In this chapter the background estimate for this search is presented.
Backgrounds to the single top production signal are all other processes contributing events to the sample after application of the event selection criteria. Two classes of backgrounds are distinguished:

- background contributions originating from top quark production, i.e. $t\bar{t}$ production.
- background processes, where no top quarks are involved. Here this class is called non-top backgrounds.

In this chapter the number of expected background events is calculated. In contrast to $t\bar{t}$ production, where precise cross section predictions and measurements exist, especially the cross section predictions for prompt W bosons plus additional jets production (W+jets) have large uncertainties. Therefore, these backgrounds have to be treated specially.
If a cross section of a process is well established, the event detection efficiency is calculated as described for the single top signals. Therefore the diboson production which belongs to the non-top backgrounds is treated different from the other considered non-top background sources.

5.1 $t\bar{t}$ Background

In this section the number of expected $t\bar{t}$ events to be expected after application of the event selection criteria is derived. This number will be calculated using the same technique as for the signal processes. Due to the uncertainty of the top quark mass a systematic error to the cross section prediction was taken into account.

	m_{top}	$\sigma_{t\bar{t}}$	Ref.
Berger and Conto.	175 GeV/c^2	$7.15^{+0.09}_{-0.55}$ pb	[81]
Bonciani et al.	175 GeV/c^2	$6.70^{+0.71}_{-0.88}$ pb	[82, 14]
Kidonakis	175 GeV/c^2	6.77 ± 0.42 pb	[13]
Bonciani et al.	170 GeV/c^2	$7.83^{+0.86}_{-1.04}$ pb	[82, 14]
Bonciani et al.	180 GeV/c^2	$5.75^{+0.59}_{-0.75}$ pb	[82, 14]

Table 5.1: Cross section predictions by three different groups of theorists for $p\overline{p}$ collisions at $\sqrt{s} = 1.96$ TeV.

5.1.1 $t\bar{t}$ cross section

In $p\overline{p}$ collisions at $\sqrt{s} = 1.96$ TeV top quark production is dominated by $t\bar{t}$-pair production via the strong interaction. Quark-antiquark annihilation is the dominating sub-process, contributing about 85% of the cross section. NLO corrections to the cross section are available since the late 1980's [79, 80]. More recent calculations try to improve the predictions by resuming leading and next-to-leading logarithmic terms in the cross-section which mainly originate from soft initial-state gluon bremsstrahlung. Table 5.1 shows the predictions of three different groups for $m_{\text{top}} = 175$ GeV/c^2.

The results of Berger and Contopanagos (BECO) were scaled down from their predictions for $\sqrt{s} = 2.00$ TeV. In our analysis we use the prediction by Bonciani et al. (BCMN) [82, 14] to calculate the number of expected $t\bar{t}$ events. Two reasons motivate that decision:

1. BCMN work with the most recent set of PDFs.
2. The error assigned by BCMN includes systematic uncertainties due to the choice of the PDF.

To take into account different predictions by BECO and Kidonakis half the difference between BCMN and BECO was assigned as additional systematic uncertainty $\Delta_2 = 0.23$ pb and added in quadrature to the error assigned by BCMN. These errors have been symmetrized. This was done by taking the average between the negative and positive errors. Additionally, the uncertainty in $\sigma_{t\bar{t}}$ due to the top mass uncertainty $\Delta m_{\text{top}} = 5$ GeV/c^2 was considered. The average difference between the cross section for 170/175 GeV/c^2 and 180/175 GeV/c^2, which is $\Delta_3 = 1.04$ pb, was taken. Adding up all three uncertainties in quadrature results in:

$$\Delta\sigma_{t\bar{t}} = \sqrt{0.795^2 + 0.23^2 + 1.04^2}\ \text{pb} = 1.32\ \text{pb} \tag{5.1}$$

m_{top}	$\sigma_{t\bar{t}}$
170 GeV/c^2	(7.83 ± 1.54) pb
175 GeV/c^2	(6.70 ± 1.32) pb
180 GeV/c^2	(5.75 ± 1.13) pb

Table 5.2: Cross section predictions used in our analysis to predict the number of $t\bar{t}$ background events.

Thus, $\sigma_{t\bar{t}} = (6.70 \pm 1.32)$ pb was used. Including the scaled uncertainty due to the other theoretical predictions (also for $m_{\text{top}} = 170, 180$ GeV/c^2) we get the numbers given in Table 5.2.

5.1.2 Event Detection Efficiency For $t\bar{t}$ Events

To calculate ϵ_{evt} for $t\bar{t}$ events the PYTHIA Monte Carlo program is used. The *ttopei* sample containing 398037 $t\bar{t}$ events is used as the default sample. To check the modeling also the HERWIG Monte Carlo Program was used. Table 5.3 lists the samples used.

$t\bar{t}$ Monte Carlo samples

Sample	Generator	Description	N ntup.
ttopei	PYTHIA	m_{top}=175 GeV/c^2	398037
ttopli	HERWIG	m_{top}=175 GeV/c^2	378471
ttoppk	HERWIG	m_{top}=170 GeV/c^2	206958
ttopsk	HERWIG	m_{top}=180 GeV/c^2	208000

Table 5.3: Monte Carlo samples used for the $t\bar{t}$ acceptance.

The number of Monte Carlo events surviving the event selection are listed in Table B.3 in the appendix. The Monte Carlo event detection efficiency is given in Table B.4 in the appendix. The b-tagging scale factors are given in Table 5.4.

B-tag Efficiencies				
Process	Sample	K_{12}	K_1	K_2
ttbar Pythia	ttopei	0.8566	0.9155	0.6729
Herwig	ttopli	0.8584	0.9211	0.6636
Herwig, 170	ttoppk	0.8562	0.9117	0.6815
Herwig, 180	ttopsk	0.8565	0.9128	0.6811

Table 5.4: Correction factor for b-tagging efficiency of the various $t\bar{t}$ samples.

Correction Factor Monte Carlo to Data				
	$t\bar{t}$ samples			
Sample	ttbar Pythia	Herwig	Herwig, 170	Herwig, 180
Sample	ttopei	ttopli	ttoppk	ttopsk
CEM Electrons				
btag ≥ 1	0.813±0.060	0.815±0.060	0.813±0.060	0.813±0.060
btag == 1	0.869±0.064	0.875±0.064	0.866±0.064	0.867±0.064
btag == 2	0.639±0.047	0.630±0.046	0.647±0.048	0.647±0.048
CMUP Muons				
btag ≥ 1	0.748±0.055	0.750±0.056	0.748±0.055	0.748±0.055
btag == 1	0.799±0.059	0.804±0.060	0.796±0.059	0.797±0.059
btag == 2	0.587±0.044	0.579±0.043	0.595±0.044	0.595±0.044
CMX Muons				
btag ≥ 1	0.847±0.063	0.850±0.063	0.848±0.063	0.848±0.063
btag == 1	0.906±0.067	0.912±0.067	0.902±0.067	0.904±0.067
btag == 2	0.666±0.049	0.657±0.048	0.675±0.050	0.674±0.050

Table 5.5: ϵ_{corr} for $t\bar{t}$ Monte Carlo samples.

The correction factors ϵ_{corr} are listed in in Tab. 5.5. The event detection efficiency ϵ_{evt} can be found in Table 5.6.

Event Detection Efficiency in %				
	$t\bar{t}$ samples			
Process	ttbar Pythia	Herwig	Herwig, 170	Herwig, 180
Sample	ttopei	ttopli	ttoppk	ttopsk
CEM Electrons				
ϵ_{btag}	0.433±0.033	0.431±0.033	0.437±0.035	0.434±0.035
$\epsilon_{\mathsf{btag=1}}$	0.376±0.028	0.372±0.028	0.364±0.029	0.365±0.027
$\epsilon_{\mathsf{M}\ell\nu\mathsf{b}}$	0.201±0.016	0.207±0.017	0.224±0.019	0.194±0.017
ϵ_{jet1}	0.196±0.016	0.202±0.016	0.217±0.018	0.189±0.016
ϵ_{1tag}	0.174±0.014	0.179±0.015	0.193±0.017	0.162±0.014
$\epsilon_{\mathsf{1tag,ET}}$	0.169±0.014	0.173±0.014	0.186±0.016	0.158±0.014
ϵ_{2tag}	0.030±0.003	0.031±0.003	0.034±0.004	0.033±0.004
CMUP Muons				
ϵ_{btag}	0.215±0.017	0.222±0.018	0.223±0.019	0.225±0.019
$\epsilon_{\mathsf{btag=1}}$	0.183±0.014	0.193±0.015	0.193±0.015	0.195±0.015
$\epsilon_{\mathsf{M}\ell\nu\mathsf{b}}$	0.107±0.009	0.108±0.009	0.114±0.010	0.102±0.010
ϵ_{jet1}	0.104±0.009	0.104±0.009	0.110±0.010	0.100±0.009
ϵ_{1tag}	0.091±0.008	0.094±0.008	0.098±0.009	0.088±0.009
$\epsilon_{\mathsf{1tag,ET}}$	0.088±0.008	0.090±0.008	0.095±0.009	0.086±0.008
ϵ_{2tag}	0.018±0.002	0.016±0.002	0.017±0.002	0.015±0.002
CMX Muons				
ϵ_{btag}	0.101±0.009	0.106±0.009	0.098±0.010	0.102±0.010
$\epsilon_{\mathsf{btag=1}}$	0.085±0.007	0.91±0.007	0.084±0.007	0.088±0.007
$\epsilon_{\mathsf{M}\ell\nu\mathsf{b}}$	0.048±0.005	0.056±0.005	0.049±0.006	0.047±0.006
ϵ_{jet1}	0.047±0.005	0.055±0.005	0.047±0.006	0.046±0.005
ϵ_{1tag}	0.041±0.004	0.048±0.005	0.041±0.005	0.041±0.005
$\epsilon_{\mathsf{1tag,ET}}$	0.040±0.004	0.047±0.005	0.039±0.005	0.040±0.005
ϵ_{2tag}	0.008±0.001	0.009±0.001	0.008±0.002	0.007±0.002

Table 5.6: $\epsilon_{\mathsf{BR}} \cdot \epsilon_{\mathsf{evt}}^{\mathsf{MC}} \cdot \epsilon_{\mathsf{corr}} \cdot \epsilon_{\mathsf{trig}}$ for $t\bar{t}$ Monte Carlo samples.

5.1.3 Number of expected $t\bar{t}$ events

After calculation of the event detection efficiency, the number of expected $t\bar{t}$ events can be calculated. The number of expected events are given in Tab. 5.7. The assigned errors include the systematic uncertainties due to the event generator and the top mass uncertainty. The relative uncertainties are given in Tab. 5.7. The numbers obtained using the PYTHIA Monte Carlo program will be used as the standard expectation, whereas the difference to the HERWIG results accounts for the systematic uncertainty due to this choice. After the b-tag requirement 8.03±1.79 events are expected to contribute to the data sample.

	$t\bar{t}$ samples			
Process	ttbar Pythia	Herwig	Herwig, 170	Herwig, 180
Sample	ttopei	ttopli	ttoppk	ttopsk
N_{btag}	8.03±1.79	8.14±1.82	8.13±1.83	8.16±1.83
$N_{\mathsf{btag=1}}$	6.90±1.52	7.03±1.54	7.08±1.54	6.94±1.52
$N_{\mathsf{M}\ell\nu\mathsf{b}}$	3.82±0.86	3.97±0.89	4.16±0.95	3.67±0.84
N_{jet1}	3.73±0.84	3.86±0.87	4.02±0.92	3.59±0.82
N_{1tag}	3.27±0.74	3.43±0.77	3.57±0.82	3.12±0.72
$N_{\mathsf{1tag,ET}}$	3.18±0.72	3.32±0.75	3.43±0.79	3.04±0.70
N_{2tag}	0.60±0.14	0.60±0.14	0.64±0.16	0.59±0.15

Table 5.7: Number of expected events for $t\bar{t}$ Monte Carlo samples.

5.2 Diboson Acceptance

In this section the number of background events originating from diboson production will be derived. Such events can significantly contribute to the backgrounds as the W and Z bosons decay into leptons and quarks. To predict the number of diboson events in the selected data sample the theoretical cross sections predicted by Campbell and Ellis [83] are used to calculate the event detection efficiency and the number of expected events. The first line in table 5.8 gives the numbers calculated by Campbell and Ellis. The errors given for these cross sections are 3% relative to the central value.

$\sqrt{s}$	WW	WZ	ZZ
2.00 TeV	13.5 pb	4.02 pb	1.60 pb
1.96 TeV	13.30 pb	3.96 pb	1.57 pb

Table 5.8: The predicted cross sections for diboson production at the Tevatron.

Their numbers have been calculated assuming $\sqrt{s} = 2.00$ TeV. Therefore, these numbers have been rescaled to a collider energy $\sqrt{s} = 1.96$ TeV. This has been performed by a linear and a quadratic interpolation of the numbers given. The mean of those interpolations is then the estimator for the cross sections of diboson production. The means are shown in the second line of the table.

The calculation of the event detection efficiency is done analog to the signal calculations. The used Monte Carlo samples are listed in table 5.9.

Di-boson samples, Alpgen Generator

Sample	Process	Description	N ntup.
atop4x	WW0p	$W_1 \rightarrow e$, μ, τ	944969
atop0y	WZ0p	no filter	191011
atop0z	ZZ0p	no filter	223606

Table 5.9: Monte Carlo samples used for the diboson acceptance.

The results are shown in the following tables: The number of Monte Carlo events for our six cut scenarios are listed in Table B.5 in the appendix. The Monte Carlo event detection efficiency is give in Table B.6. The b-tagging scale factors are given in Table 5.10. The correction factors ϵ_{corr} are listed in Tab. 5.11. The event detection efficiency ϵ_{evt} can be found in Table 5.12.

B-tag Efficiencies				
Process	Sample	K_{12}	K_1	K_2
WW0p	atop4x	0.8233	0.8242	0.6316
WZ0p	atop0y	0.8361	0.8551	0.6889
ZZ0p	atop0z	0.772	0.7714	0.7778

Table 5.10: Correction factor for b-tagging efficiency of the various diboson samples.

Correction Factor Monte Carlo to Data			
Sample	WW0p	WZ0p	ZZ0p
Sample	atop4x	atop0y	atop0z
CEM Electrons			
btag ≥ 1	0.781±0.058	0.793±0.058	0.732±0.054
btag == 1	0.782±0.058	0.811±0.060	0.731±0.054
btag == 2	0.599±0.044	0.653±0.048	0.737±0.054
CMUP Muons			
btag ≥ 1	0.718±0.053	0.729±0.054	0.673±0.050
btag == 1	0.719±0.053	0.745±0.055	0.672±0.050
btag == 2	0.551±0.041	0.600±0.044	0.678±0.050
CMX Muons			
btag ≥ 1	0.814±0.060	0.826±0.061	0.763±0.056
btag == 1	0.815±0.060	0.845±0.062	0.762±0.056
btag == 2	0.625±0.046	0.681±0.050	0.768±0.057

Table 5.11: ϵ_{corr} for diboson Monte Carlo samples.

Event Detection Efficiency in %			
Process	WW0p	WZ0p	ZZ0p
Sample	atop4x	atop0y	atop0z
CEM Electrons			
ϵ_{btag}	0.030±0.002	0.092±0.009	0.009±0.002
$\epsilon_{\mathsf{btag=1}}$	0.030±0.002	0.078±0.006	0.009±0.001
$\epsilon_{\mathsf{M}\ell\nu\mathsf{b}}$	0.013±0.001	0.047±0.006	0.004±0.001
ϵ_{jet1}	0.011±0.001	0.043±0.005	0.004±0.001
ϵ_{1tag}	0.013±0.001	0.039±0.005	0.003±0.001
$\epsilon_{\mathsf{1tag,ET}}$	0.011±0.001	0.035±0.005	0.003±0.001
ϵ_{2tag}	0.000±0.000	0.007±0.002	0.000±0.000
CMUP Muons			
ϵ_{btag}	0.014±0.001	0.048±0.005	0.014±0.002
$\epsilon_{\mathsf{btag=1}}$	0.014±0.001	0.042±0.004	0.011±0.001
$\epsilon_{\mathsf{M}\ell\nu\mathsf{b}}$	0.006±0.001	0.021±0.003	0.006±0.001
ϵ_{jet1}	0.006±0.001	0.020±0.003	0.006±0.001
ϵ_{1tag}	0.006±0.001	0.020±0.003	0.005±0.001
$\epsilon_{\mathsf{1tag,ET}}$	0.006±0.001	0.018±0.003	0.004±0.001
ϵ_{2tag}	0.000±0.000	0.002±0.001	0.002±0.001
CMX Muons			
ϵ_{btag}	0.008±0.001	0.028±0.004	0.006±0.001
$\epsilon_{\mathsf{btag=1}}$	0.008±0.001	0.023±0.004	0.005±0.001
$\epsilon_{\mathsf{M}\ell\nu\mathsf{b}}$	0.004±0.000	0.013±0.003	0.003±0.001
ϵ_{jet1}	0.003±0.000	0.012±0.002	0.003±0.001
ϵ_{1tag}	0.003±0.000	0.012±0.002	0.002±0.001
$\epsilon_{\mathsf{1tag,ET}}$	0.003±0.000	0.010±0.002	0.002±0.001
ϵ_{2tag}	0.000±0.000	0.001±0.001	0.000±0.000

Table 5.12: $\epsilon_{\mathsf{BR}} \cdot \epsilon_{\mathsf{evt}}^{\mathsf{MC}} \cdot \epsilon_{\mathsf{corr}} \cdot \epsilon_{\mathsf{trig}}$ for diboson Monte Carlo samples.

5.2.1 Number of Expected Diboson Events

The number of expected events are given in Table 5.13. The errors assigned to the numbers for the different scenarios include the 3% uncertainty due to the theoretical prediction and the uncertainty due to the integrated luminosity measurement of 6%.

Process	WW0p	WZ0p	ZZ0p	Σ diboson
Sample	atop4x	atop0y	atop0z	
N_{btag}	1.11±0.12	1.07±0.14	0.07±0.01	2.25±0.27
$N_{\mathsf{btag=1}}$	1.11±0.11	0.91±0.09	0.06±0.01	2.09±0.21
$N_{\mathsf{M}\ell\nu\mathsf{b}}$	0.47±0.05	0.52±0.08	0.03±0.01	1.02±0.14
N_{jet1}	0.43±0.05	0.47±0.07	0.03±0.01	0.93±0.13
N_{1tag}	0.47±0.05	0.45±0.07	0.03±0.01	0.94±0.13
$N_{\mathsf{1tag,ET}}$	0.43±0.05	0.40±0.07	0.02±0.01	0.85±0.12
N_{2tag}	0.00±0.00	0.07±0.02	0.01±0.00	0.07±0.02

Table 5.13: Number of expected events derived from diboson Monte Carlo samples.

5.3 Non-Top Background Estimate

In addition to the $t\bar{t}$ and diboson backgrounds discussed in the previous section, one large source of background events to the single top signal is the associated production of a W boson and multiple jets. An other significant source of background is the generic production of jets predicted by QCD. One of those jets can fake a lepton and thus enter the sample. In this section the calculation of our background estimate will be presented.
While the $t\bar{t}$ and diboson background can be estimated using the theoretical cross section predictions and acceptance from Monte Carlo, this method does not work for W plus multi-jet backgrounds because those cross sections are not reliably predicted by theory.
Since our event selection requires an identified bottom jet, the heavy flavor contribution will dominate this class of backgrounds, whereas due to a higher cross section the light flavor contribution dominates the samples after application of the lepton identification and the $\not\!\!E_T$ requirements, but without the b-tag requirement. For the CDF $t\bar{t}$ cross section measurement using b-tagging a background estimate was performed which is partly based on CDF data and partly on Monte Carlo simulations (known as method 2) [84]. The following section will briefly describe this calculation.

5.3.1 Method 2 Non-Top Background Estimate

One of the main problems of Monte Carlo generators is that those use only leading order calculation to predict the jet multiplicity for W/Z and multi-jet production. This leads to a large uncertainty in the absolute or overall normalization, despite of the fact that the individual relative contributions of the important diagrams are well-defined. The "method 2" estimate uses therefore the matrix element calculations of the relative heavy flavor fraction derived from Monte Carlo generators and collider data to measure the overall normalization. The combination of the two results gives thus the background estimate. This is achieved by multiplying the number of pretag W+jets events in data by the MC derived heavy flavor fraction and the tagging efficiency in Monte Carlo (including the scale factor between data and simulation).

In order to derive the heavy flavor fractions the ALPGEN matrix element calculations are fed into the HERWIG parton shower program to simulate gluon radiation. This combination of calculations describes the collider data better than each approach separately. Unfortunately, this procedure leads to double counting in regions of phase space which are populated by higher order matrix elements and the parton shower. For example can the shower generate an additional parton in the $W + n$ parton Monte Carlo that covers parts of the phase of a $W + (n + 1)$ parton Monte Carlo. This problem can be solved by rejecting events where the parton shower produced a hard gluon. After applying this

algorithm the fractions of events populating the individual jet bins in data and Monte Carlo are in good agreement.
The heavy flavor fractions are then defined by the ratio of observed W+heavy flavor events and the W+jets cross sections. The systematic uncertainties assigned to these fractions arise due to the matching procedure to avoid double counting (15%), the choice of the interaction scale Q^2 (5%), the used PDF (5-10%), the uncertainty of the jet energy scale (5-10%), the modelling of intial and final state radiation (10%) and the uncertainties due to the limited knowledge of the quark masses (6-10%). The numbers in brackets denote the resulting relative uncertainties of the heavy flavor fractions. The resulting total systematic uncertainty adds up to about 21%.
Since the current data sample contains only few tagged W+jets data events the Monte Carlo derived heavy flavor fractions cannot directly be verified. Method 2 used a tagged QCD jet sample instead, whose production process is described by diagrams similar to the W+jets sample. The selection requirements for these event are 2 or 3 jets with $E_{\mathrm{T}} > 15$ GeV and $|\eta| < 2.0$ and at least one jet with $E_{\mathrm{T}} > 20$ GeV to fulfill trigger requirements. Within this QCD jet sample the fractions are fit by a linear combination of the pseudo-$c\tau$ distributions of b, c and light parton or gluon jets derived from MC. The pseudo-$c\tau$ variable is defined as $L_{2D} \cdot M_{vertex}/p_{\mathrm{T}}^{vertex}$, here M_{vertex} denotes the invariant mass of all tracks in the secondary vertex and p_{T}^{vertex} is the transverse momentum of the secondary vertex four-vector. L_{2D} is the two-dimensional decay length of the vertex. The fit heavy flavor fractions are 50% higher then the Monte Carlo prediction. Due to this fitting procedure an additional systematic uncertainty of 5% (10%) is assigned to the b (c) fraction. Table 5.14 lists the heavy flavor fractions and the tagging efficiencies after application of a 50% correction factor for $W + 2$ jets events. These numbers can thus be used to predict the fractions of events in the $W + 2$ jets sample which have $Wb\bar{b}$, $Wc\bar{c}$ and Wc by multiplication with the number of pretag events after subtraction of the non-W backgrounds and the expected mistags.

5.3.2 Non-W QCD Background

The non-W QCD background is a composition of events where the identified lepton is not originating from a W boson decay. These events include lepton and missing energy fakes in addition to semileptonic b hadron decays. Since for method 2 it is crucial to measure the absolute number of W+jets events before tagging, it is necessary to understand the non-W contamination in the pretag sample. There is a number of tagged non-W QCD events that contribute to the background after requiring a SecVtx-tag. Both fractions are directly measured using collider data.

This measurement is based on the fact that in a leptonic W decay an isolated lepton and a large missing transverse energy, the signature of the neutrino, are

	W + HF fraction [%]	tagging eff. ($\geq 1tag$) [%]
1B	1.4±0.4	27.8±2.5
2B	1.4±0.4	48.6±3.2
1C	2.4±0.6	6.7±1.0
2C	1.8±0.5	12.3±1.9
Wc	6.0±1.3	6.1±0.9

Table 5.14: The heavy flavor fractions and the SecVtx tagging efficiency in the W + 2jet sample. The 1B (1C) fractions are for events with exactly one jet matched to a b (c) parton, and the 2B (2C) fractions are for events with exactly two jets matched to the partons.

produced, while for non-W events this is not necessarily true. Therefore one uses the sideband regions of lepton isolation and $\not\!\!E_T$ in the high-p_{T} lepton sample to extrapolate the QCD contaminations in the signal region.
Four regions of interest are defined:

- Region A: isolation > 0.2 and $\not\!\!E_T$ <15 GeV
- Region B: isolation < 0.1 and $\not\!\!E_T$ <15 GeV
- Region C: isolation > 0.2 and $\not\!\!E_T$ >20 GeV
- Region D: isolation < 0.1 and $\not\!\!E_T$ >20 GeV

Here Region D corresponds to the W boson signal region. The used variables isolation and $\not\!\!E_T$ are assumed to be uncorrelated for QCD background events and thus the ratio of non-W events at low and high isolation in the low $\not\!\!E_T$ region should be the same as in the high $\not\!\!E_T$ region. So the non-W background events can be estimated by

$$QCD_D = \frac{N_B \cdot N_C}{N_A}. \tag{5.2}$$

Here N denotes the number of events observed in the index region, after applying a correction due to the contribution of true W and $t\bar{t}$ events. This correction is determined using Monte Carlo samples to calculate the ratio of these events in the different regions and then normalized to the observed number of pretag events. The correction is 5-30% depending on jet multiplicity and lepton type. The major uncertainty of this method is due to the assumption that QCD events are uncorrelated in the isolation-$\not\!\!E_T$ plane. This uncertainty is about 25%.
The pretag non-W QCD fraction of electrons was measured to 0.17±0.04 in the 2 jet bin, and 0.043±0.011 for muons in this bin. The total number of expected QCD events for 162 pb^{-1} is 10.1±1.7 events.

5.3.3 Mistags

As already mentioned when introducing the SecVtx algorithm, there are also secondary vertices found by the algorithm not originating from the decay of heavy flavor hadrons. This is expected to be mainly due to a random combination of tracks fit to a vertex. To estimate the number of mistags to be expected in the data sample the mistag matrix is used. This matrix is parameterized using the number of tracks assigned to the jet, the uncorrected jet E_{T}, the η and ϕ coordinates of the jet axis and the sum of transverse energies of all taggable jets. This matrix is obtained from inclusive jet samples. Each jet in the pretag sample is weighted by the mistag rate given by the matrix. The sum of the assigned weights of all jets in an event is then scaled down by the fraction of pretag events due to QCD background, since this fraction has already been accounted for in the previous section. The low mistag rate per jet corresponds to a negligible number of events having more than one mistagged jet. Therefore, the number of mistagged jets is a good approximation for the number of events containing at least one mistagged jet. The uncertainties assigned to this background are given by the statistical error of the pretag sample. In addition, a systematic uncertainty of 11% due to the sample dependency of the mistag rate parameterization is assigned. The expected number of mistags in the 2 jet sample is 17.0±2.4 events.

5.3.4 W+Heavy Flavor Backgrounds

After subtraction of the non-W backgrounds from the pretag events, one can calculate the W+heavy flavor contributions to the tagged sample by using the method 2 algorithm described in section 5.3.1 The number of events in the 2 jet bin having $Wb\bar{b}$, $Wc\bar{c}$ and Wc contributions are given in table 5.15. These numbers have been obtained by multiplying the pretag events by the corresponding heavy flavor fraction and the tagging efficiency depending on the number of visible heavy flavor jets in Monte Carlo. In addition the mistags and the non-W QCD events are listed.

5.3.5 Calculation Of The Non-Top Backgrounds For The Single Top Search

In the previous sections the number of expected non-top events using the method 2 calculations have been presented. Since in this single top analysis jets have been accepted up to $|\eta| \leq 2.8$ the numbers derived by the method 2 estimate have to be scaled to account for the differences in the event selection criteria. The selection cuts of our single top analysis are described in section 4.

	$W+2$ jets
Pretag	2448
$Wb\bar{b}$	22.5±2.4
$Wc\bar{c}$	8.0±2.2
Wc	7.7±2.0
Mistags	17.0±2.4
non-W QCD	10.1±1.7

Table 5.15: Summary of the method 2 background estimate for the 2 jet bin.

In order to scale these numbers we calculate a scale factor based on the corresponding ALPGEN Monte Carlo samples and non-W QCD samples, respectively. Five different classes of events contribute to our non-top background (other than diboson already discussed) events: $Wb\bar{b}$, $Wc\bar{c}$, Wc, mistags and non-W events. We use the following Monte Carlo samples generated by Alpgen to calculate the scale factors for the W+heavy flavor background and the mistags:

- $Wb\bar{b}$: $We\nu BB0p$ (atop40), $W\mu\nu BB0p$ (atop46), $W\tau\nu BB0p$ (atop4c)
- $Wc\bar{c}$: $We\nu CC0p$ (atop43), $W\mu\nu CC0p$ (atop49), $W\tau\nu CC0p$ (atop4f)
- Wc: $We\nu C1p$ (atop1w), $W\mu\nu C1p$ (atop4w)
- Mistags: $We\nu 2p$ (atop02), $W\mu\nu 2p$ (atop08), $W\tau\nu 2p$ (atop2e)

For estimating the non-W QCD contribution a tagged sample was used in which the isolation requirement of the lepton identification was reversed.
Each of these files is then processed by the same cuts as used for the method 2 background estimate. The number of events that pass the selection are denoted as $N_{\eta 2}$. The events that pass the extended jet definition up to $|\eta| < 2.8$ are labeled $N_{\eta 2.8}$. This extension was introduced to increase the single top t-channel production acceptance. In addition, the number of events passing the $M_{\ell\nu b}$ ($N_{M\ell\nu b}$), E_T(jet 1) > 30 GeV (N_{jet1}), exactly one b-tag (N_{1tag}), exactly one b-tag and E_T(jet 1) > 30 GeV ($N_{1tag,ET}$), exactly two b-tags (N_{2tag}) requirements have been evaluated. The number of events surviving these cut scenarios are given in Tab. 5.16.

The mistag samples are treated special. If we apply the b-tag requirement only very few events remain. Too little to predict cut efficiencies for the subsequent cuts. Therefore, we apply the mistag matrix to each jet and consider this jet b-tagged which has the highest mistag probability. This pseudo tag is needed since a invariant mass of the lepton, neutrino candidate and the tagged jet is reconstructed and required to fall within the window of 140-210 GeV/c.

Process	Wbb0p	Wcc0p	Wc	Mis-tags	non-W
$N_{\eta 2}$	4169	967	1389	9121	1198
$N_{\eta 2.8}$	4388	1021	1524	9900	1219
$N_{btag=1}$	3554	993	1514	9900	1154
$N_{M\ell\nu b}$	2036	439	679	4036	359
N_{jet1}	1731	375	597	3276	328
N_{1tag}	1646	426	673	–	327
$N_{1tag,ET}$	1394	365	591	–	298
N_{2tag}	390	13	6	–	32

Table 5.16: Number of events for different cut scenarios.

As already mentioned the number of events contributing to the 2-tag subsample is negligible. The scale factors for the method 2 numbers are then derived by dividing the remaining events after each cut by the corresponding event numbers $N_{\eta 2}$. The resulting scale factors are shown in Tab. 5.17. To evaluate the

Process	Wbb0p	Wcc0p	Wc	Mis-tags	non-W
$\epsilon_{\eta 2.8}$	1.0525	1.0558	1.0972	1.0854	1.0175
$\epsilon_{btag=1}$	0.8525	1.0239	1.0830	1.0854	0.9633
$\epsilon_{M\ell\nu b}$	0.4640	0.4300	0.4455	0.4077	0.2945
ϵ_{jet1}	0.3945	0.3673	0.3917	0.3309	0.2691
ϵ_{1tag}	0.3751	0.4172	0.4416	–	0.2682
$\epsilon_{1tag,ET}$	0.3177	0.3575	0.3878	–	0.2445
ϵ_{2tag}	0.0889	0.0127	0.0039	–	0.0263

Table 5.17: Scale factor for different cut scenarios relative to the method 2 result.

systematic errors due to introducing such a scale factor the jet energy scale was shifted by $\pm 1\sigma$ from the mean value and a symmetrized error calculated. This is based on the assumption that after applying a cut on the invariant mass M_{lvb} the errors are dominated by the jet energy scale uncertainty. The obtained errors are given in table 5.18. In case of requiring exactly one b-tag ($N_{\mathrm{btag=1}}$) the error was calculated assuming the identical relative error as obtained by the method 2

calculation. These errors are added in quadrature to the relative errors obtained

Process	Wbb0p	Wcc0p	Wc	Mistags	non-W
$N_{M\ell\nu b}$	11.5%	10.8%	11.0%	16.1%	15.5%
N_{jet1}	13.0%	12.4%	12.9%	17.9%	15.9%
N_{1tag}	13.0%	11.2%	11.2%	–	15.9%
$N_{\text{1tag,ET}}$	14.5%	12.7%	13.2%	–	16.3%

Table 5.18: Relative errors on scale factors for different cut scenarios.

by the method 2 calculation. So the final numbers for the non-top background estimate and the corresponding errors can be calculated.

Process	Wbbar	Wccbar	Wc	Mistags	non-W
$N_{\eta 2.0}$	22.5±6.5	8.0±2.2	7.7±2.0	17.0±2.4	10.1±1.7
$N_{\eta 2.8}$	23.68±6.84	8.45±2.32	8.45±2.19	18.45±2.60	10.28±1.73
$N_{\mathrm{btag}=1}$	19.18±5.54	8.22±2.26	8.39±2.17	18.45±2.60	9.74±1.64
$N_{M\ell\nu b}$	10.99±3.42	3.63±1.07	3.76±1.06	7.52±1.61	3.03±0.69
N_{jet1}	9.34±2.96	3.10±0.94	3.31±0.96	6.11±1.39	2.77±0.64
$N_{1\mathrm{tag}}$	8.88±2.81	3.52±1.05	3.73±1.06	7.52±1.61	2.76±0.64
$N_{1\mathrm{tag,ET}}$	7.52±2.43	3.02±0.91	3.28±0.95	6.11±1.39	2.51±0.59
$N_{2\mathrm{tag}}$	2.11±0.67	0.11±0.03	0.03±0.01	0.00±0.00	0.27±0.06

Table 5.19: Number of expected W+jets events in single top analysis.

5.3.6 Number of Expected Non-Top Events

The resulting number of W+Jets events predicted for the single top analysis are given in Tab. 5.19. The background estimate given by the method 2 calculation is given in the first line of this table denoted as $N_{\eta 2.0}$. Table 5.20 shows the sum of the W+jets result in the 2 jet bin and the diboson contribution discussed before. The errors for the W+jets result have been evaluated by linear addition of the errors assigned to the W+ heavy flavor contributions and then adding the errors of mistags and non-W background in quadrature. The linear addition of errors was chosen since the errors originating from the heavy flavor fraction calculations are highly correlated for these samples and the number of pretag events is used for each contribution. To get the total number of non-top events the number of diboson events has to be added. The number of expected diboson events was calculated in table 5.13

Process	W + Jets	di-boson	Total Non-Top
N_{btag}	69.30 ± 11.78	2.25 ± 0.27	71.55 ± 11.78
$N_{\text{btag=1}}$	63.98 ± 10.43	2.09 ± 0.21	66.07 ± 10.43
$N_{M\ell\nu b}$	28.93 ± 5.82	1.02 ± 0.14	29.95 ± 5.82
N_{jet1}	24.63 ± 5.09	0.93 ± 0.13	25.56 ± 5.09
N_{1tag}	26.42 ± 5.21	0.94 ± 0.13	27.36 ± 5.21
$N_{\text{1tag,ET}}$	22.44 ± 4.56	0.85 ± 0.12	23.29 ± 4.56
N_{2tag}	2.52 ± 0.71	0.07 ± 0.02	2.59 ± 0.71

Table 5.20: Number of expected non-top events for this analysis.

Chapter 6

Analysis technique

In this chapter the analysis techniques used in the analysis are presented. A likelihood function is used to measure the single top contents of the CDF data sample and calculate upper limits on single top production. This technique will be explained in the first part of this chapter. In addition a multivariate technique, here an iterated discriminant analysis, is used to improve the significance of the analysis. This analysis technique will be presented in the last part of this chapter.

6.1 The Likelihood Function for The Separate Single Top Search

In order to extract the signal content of our data sample, a binned likelihood function is used. This technique is commonly used in experimental high energy physics to measure the most probable value of observables such as cross sections. In this section the likelihood function for the single top search and the implementation of systematic uncertainties is presented.

6.1.1 The Likelihood Function

Likelihood functions [85] are based on a known or estimated probability density function $f(x|a)$ where x is an observable and a is a set of unknown parameters to be estimated. The likelihood function $L(a)$ for a set of measured observables $x_1, x_2, \ldots x_n$ is defined by

$$L(a) = f(x_1|a) \cdot f(x_2|a) \cdots f(x_n|a) = \prod_{i=1}^{n} f(x_i|a) \tag{6.1}$$

This function $L(a)$ can be interpreted as the probability of obtaining the measured values x_i for a given parameter set a. So the best estimator $\hat{a}$ for the

parameter set a is the one that maximizes the likelihood function $L(a)$ with respect to the given data set $\{x_i\}$.
Since a binned likelihood function is used for this analysis the contents of a set of bins n_i derived from a distribution are used as observables. The parameter a aimed to measure or limit is the production cross section σ.
The statistical content of a bin n_i is described by the Poisson distribution

$$P(n_i) = \frac{\mu_i^{n_i}}{n_i!} e^{-\mu_i} \tag{6.2}$$

where μ_i denotes the expectation value of the distribution in this bin i. This expectation value μ_i is the sum of all signal and background process expectation values μ_{ji} contributing to the specific bin i. Each μ_{ji} is the product of the productions cross section σ_j times a bin specific acceptance function ν_{ji}. Thus the Poisson mean for a bin i in the presence of d signal and background processes is

$$\mu_i = \sum_{j=1}^{d} \mu_{ji} = \sum_{j=1}^{d} \nu_{ji}\sigma_j. \tag{6.3}$$

The likelihood consisting of q bins within this scenario is defined by

$$L(\sigma) = \prod_{i=1}^{q} \frac{\mu_i^{n_i}}{n_i!} e^{-\mu_i}. \tag{6.4}$$

6.1.2 Incorporation of Systematic Uncertainties

In pure Bayesian theory all nuisance parameters, including the systematic errors, should occur in the likelihood function. In this section the implementation of errors in the likelihood function is presented. Each source of systematic uncertainties leads to an uncertainty in the acceptance function ν_{ji}. Here Gaussian distributed errors are assumed, i.e. the probability that the absolute difference between a measured quantity Q and the true quantity $\hat{Q}$ is within the quoted errors, is 68.26%. This corresponds to the so-called 1σ level. The existence of errors leads to the introduction of additional parameters in the likelihood modeling the effects of these errors. These parameter occur here in the definition of the μ_{ij} and enter thus through μ_i the likelihood function.
In the case of only one source of systematic uncertainty the $\{\mu_i\}$ are defined by:

$$\mu_i(\delta) = \sum_{j=1}^{d} \mu_{ji} = \sum_{j=1}^{d} \nu_{ji}(1 + \kappa_{ij}\delta)\sigma_j \tag{6.5}$$

Here κ_{ij} is the relative effect of error at the 1σ level and δ a parameter describing the relative size of the systematic effect. The likelihood function is the given by

$$L(\sigma_1, \ldots \sigma_d, \delta) = \frac{1}{\sqrt{2\pi}} e^{-\frac{1}{2}\delta} \prod_{i=1}^{q} \frac{\mu_i(\delta)^{n_i}}{n_i!} e^{-\mu_i(\delta)}. \tag{6.6}$$

The Gaussian factor in the likelihood reflects the assumption that the errors are distributed according to the error function. Since systematic uncertainties are considered here the specific value of δ has to be applied to all processes. If one aims for setting upper limits on observables one integrates out the parameter δ and thus calculates the marginalized likelihood function L^*, which is defined by:

$$L^*(\sigma_1, \ldots, \sigma_d) = \int_{-\infty}^{\infty} L(\sigma_1, \ldots \sigma_d, \delta) d\delta \tag{6.7}$$

This reduced or marginalized likelihood is finally maximized with respect to the data set. If several independent data sets are used, a combined likelihood function can be introduced, consisting of likelihood functions for the individual subsamples. These likelihood functions are then multiplied to form the combined likelihood.

6.1.3 The Likelihood Function for the Separate t- and s-channel Search

In the previous section some general aspects of likelihood functions have been discussed. In this section the likelihood function used for this analysis is presented. The acceptances for s- and t-channel events strongly depend on the required number of b-tags in the 2-jet subsample. Almost all t-channel single top events surviving the selection have exactly one assigned b-tagged jet, while the s-channel events contribute to the 1-tag and the 2-tag subsample. Therefore, the splitting of the sample according to the number of assigned b-jets leads to a separation of the two production channels. This was also proposed in [16].

Thus, the data sample is divided in a subsample defined by events in which exactly one secondary vertex has been reconstructed and the sample where exactly two secondary vertices have been assigned to the event. Four classes of processes are considered: The t-channel and s-channel single top production modes, $t\bar{t}$ and non-top, which includes all considered processes not originating from top production. In addition the background contributions are constrained by Gaussian functions within their errors. The background cross sections will be integrated out. Since the acceptance for t-channel events in the first subsample is much higher than in the second one, this part of the likelihood is based on the observable M using n_M bins to cover the corresponding interval. This observable M has to be chosen. The observable should exhibit a strong discrimination between signal and backgrounds. For the other subsample the total number of events is used as our underlying observable since the number of expected 2-tag events is quite small.
Due to practical reasons the acceptance function ν_{ji} given in equation (6.3) is divided in two parts:

$$\nu_{ji} = \nu_j \alpha_{ji}, \tag{6.8}$$

Here the term ν_j reflects the absolute acceptance of process j, whereas α_{ij} denotes the relative acceptance within bin i. For convenience reasons the parameter $\beta_j = \sigma_j/\sigma_{\mathrm{SM,j}}$ is used which is the cross section of process j normalized to the Standard Model prediction. The following paragraph summarizes the indices and variables used in the likelihood function.

Definition of variables:

1. Four physics processes are considered:

   j = index over processes
   $j = 1$: t-channel, $j = 2$: s-channel, $j = 3$: $t\bar{t}$, $j = 4$: non-top.

2. The cross section of process j is σ_j. In the likelihood function the parameter β_j is used, the cross section normalized to its SM prediction: $\beta_j = \sigma_j/\sigma_{SM,j}$.

3. The absolute acceptance of process j is ν_j. It is the event detection efficiency multiplied with the integrated luminosity.

4. A M distribution divided into n_M bins (M *template histogram*) in the 1-tag subsample and the number of events in the double-b-tag subsample is fit. The corresponding acceptances are: ν_{j1} and ν_{jd}. The bins of the M histogram are indexed with k.

5. The normalized content of bin k of the template histogram for process j is α_{jk}.

6. 6 effects which cause systematic uncertainties in acceptance and in the shape of the template histograms are considered. The sources of systematic uncertainties are indexed with i. The relative acceptance uncertainties due to these six sources are named: ϵ_{ji}. The relative uncertainties in the bin content of bin k of the template histograms are called κ_{jik}. Since some errors are asymmetric, positive and negative uncertainties are introduced: ϵ_{ji+}, ϵ_{ji-}, κ_{jik+} and κ_{jik-}.

7. Two other uncertainties influence only the acceptance: (1) the error on the event detection efficiency (b-tag scale factor, lepton identification efficiency etc.) and (2) luminosity. Those are added in quadrature and they enter as ϵ_7 in the likelihood.

8. So in total there are $S = 7$ systematic effects taken into account.

9. Gaussian functions of variable x with mean x_0 and standard deviation σ are denoted $G(x, x_0, \sigma)$.

10. H(x) denotes the Heaviside step function.

11. The variation in strength of a systematic effect i is measured with the variable δ_i.

12. The expected mean value of bin k for the M histogram is μ_k, for the double-b-tag-bin μ_d.

13. The data observed in bin k of the M histogram are denoted n_k, the data in the 2-tag-bin n_d.

14. The cross section uncertainties are denoted as Δ_j. For the non-top background this is a rate uncertainty, since this is a sum of several processes.

15. s denotes the index of the signal process, which is $s = 1$ for the t-channel search and $s = 2$ for the s-channel search. If $s = 1$, we define $t = 2$; if $s = 2$, we define $t = 1$.

The likelihood: Using the above definitions the likelihood function L equals:

$$\begin{aligned} L_s &= L_s(\beta_1, \dots, \beta_4; \delta_1, \dots, \delta_S) \\ &= \left\{ \prod_{k=1}^{B} \frac{e^{-\mu_k} \cdot \mu_k^{n_k}}{n_k!} \right\} \cdot \frac{e^{-\mu_d} \cdot \mu_d^{n_d}}{n_d!} \cdot \prod_{j=1,\, j\neq s}^{4} G(\beta_j, 1.0, \Delta_j) \cdot \prod_{i=1}^{S} G(\delta_i, 0, 1) \end{aligned}$$

The first factors are Poisson terms for the bins of the M histogram (index k) and the double-tag-bin (index d). The second set of factors are Gaussian integration kernels which constrain the nuisance parameters to the expectation. The expected mean in bin k is:

$$\begin{aligned} \mu_k &= \sum_{j=1}^{4} \beta_j \cdot \nu_{j1} \cdot \left\{ \prod_{i=1}^{S} (1 + |\delta_i| \cdot (\epsilon_{ji+} H(\delta_i) + \epsilon_{ji-} H(-\delta_i))) \right\} \\ &\quad \cdot \alpha_{jk} \cdot \left\{ \prod_{l=1}^{S} (1 + |\delta_l| \cdot (\kappa_{jlk+} H(\delta_l) + \kappa_{jlk-} H(-\delta_l))) \right\} \\ \mu_d &= \sum_{j=1}^{4} \beta_j \cdot \nu_{jd} \cdot \left\{ \prod_{i=1}^{S} (1 + |\delta_i| \cdot (\epsilon_{ji+} H(\delta_i) + \epsilon_{ji-} H(-\delta_i))) \right\} \end{aligned}$$

The marginalized Likelihood is defined as:

$$L_s^*(\beta_s) = \int_0^{+\infty} \int_0^{+\infty} \int_0^{+\infty} \int_{dV_\delta} L_s(\beta_1, \dots, \beta_4; \delta_1, \dots, \delta_S)\, d\delta^{S+1} d\beta_3 d\beta_4 d\beta_t$$

The volume integral in δ space is defined as:

$$\int_{dV\delta} d\delta^{S+1} = \int_{a_1}^{+\infty} \dots \int_{a_S}^{+\infty} \int_{a_N}^{+\infty} d\delta_1 \dots d\delta_S d\delta_N$$

The integration is implemented as a Monte Carlo integration. For each Monte Carlo integration point random numbers are generated for the nuisance parameters β_j and δ_i according to Gaussian distributions $G(\beta_j, 1.0, \Delta_j)$ and $G(\delta_i, 0, 1)$. The lower cut offs a_j have to be chosen such, that no bin obtains unphysical, negative entries. Practically, in a Monte Carlo integration, this is done by rejecting negative factors of $1 + \epsilon_{ij}\delta_j$ and $1 + \kappa_{ijk}\delta_j$. If any one of these factors is negative for a particular δ_j re-throwing of a new random number for δ_j is performed. Effectively, this alters the Gaussian prior distributions, leading to truncated Gaussians as effective priors. A detailed description of the likelihood function can be found in [86].

6.1.4 Calculation of Upper Limits

Electroweak single top quark production is predicted by the Standard Model of high energy physics, but has not yet been discovered. If no significant signal is present in the data set and thus a measurement of a cross section or a discovery is not feasible, one can at least rule out models predicting an increased signal cross section in comparison to the Standard Model predictions. Therefore upper boundaries are calculated. Limits are calculated for a given confidence level (C.L.). The corresponding confidence level is the probability that any measurement of the examined quantity will reveal a value smaller than the quoted upper limit.

There are various approaches to calculate these upper limits. In this analysis the likelihood function will be used to determine the upper limit on electroweak single top quark production in the absence of a significant signal.
If one interprets the normalized posterior likelihood function as the posterior probability density the limit can be calculated by integrating this likelihood function. The confidence level $c_{C.L.}$ assigned to the limit σ_{up} is then defined by the area covered by the integral:

$$c_{C.L.} = \frac{\int_{-\infty}^{\sigma_{\text{up}}} L^*(\sigma^*)d\sigma^*}{\int_{-\infty}^{+\infty} L^*(\sigma^*)d\sigma^*} \tag{6.9}$$

Here $L^*(\sigma)$ is the marginalized likelihood. Since a Bayesian approach is followed in this analysis, a prior probability density is introduced. Here the Heaviside step function is used. This choice corresponds to the fact, that any physical cross section has to be greater or equals zero. Since a separate s- and t-channel single top search is presented in this analysis, the t-channel is constrained to the expectation by a Gaussian and integrated out when calculating the s-channel upper limit and vice versa. Thus, in each case 10 nuisance parameters will be integrated out. For a given confidence level equation (6.9) can be used to find the upper limit σ_{up}. This is done by shifting the upper boundary of the integral until the required confidence level has been reached. For this analysis a confidence level (C.L.) of 95% was used.

The ϵ_{ji} are obtained from determining the acceptance for shifted Monte Carlo samples, for which a particular effect as been changed by $\pm 1\,\sigma$. The κ_{jlk} are obtained from shifted and normalized template histograms γ_{jlk}: $\kappa_{jlk} = (\gamma_{jik} - \alpha_{jk})/\alpha_{jk}$. The bin content of the template histogram (α_{jk}) is subtracted from the shifted histogram (γ_{jlk}) and divided by the standard template value.

6.2 Iterated Discriminant Analysis

One of the major problems of this analysis is the reduction or the separation of signal and backgrounds. One of the methods used in this analysis is the Iterated Discriminant Analysis (IDA) which is a nonlinear variant of the Fisher discriminant analysis. In the next section a short introduction to the Fisher algorithm will be presented.

6.2.1 Fisher discriminant analysis

The aim of a discriminant algorithm is to solve the classification problem, i.e. to find a function that separates signal from background processes in a given parameter space. Fishers algorithm tries to separate signal from background by a hyperplane in the N-dimensional parameter space [85, 87]. Here the N parameters are a set of variables characterizing the signal and the background classes. The variables i from a class k can be described by a vector $\vec{X}_{ik} = (X_1^{(k)}, X_2^{(k)}, \ldots X_N^{(k)})^T$. The classification problem is then solved by measuring the Euclidean distance in the parameter space between the test event and the signal and background classes.
The algorithm calculates the estimated mean value of class k for a test sample with n_k elements, which is defined by

$$\vec{m}_k = \frac{1}{n_k} \sum_{i=1}^{n_k} \vec{X}_{ki} \tag{6.10}$$

and the covariance matrix of the two classes, which is defined by

$$\mathbf{T} = \frac{1}{n_1 + n_2} \sum_{k=1}^{2} \sum_{i=1}^{n_k} (\vec{X}_{ki} - \vec{m}_k)(\vec{X}_{ki} - \vec{m}_k)^T \,. \tag{6.11}$$

The desired separating function can be written as

$$D(\vec{X}) = \vec{a} \cdot \vec{X} \,. \tag{6.12}$$

Here $\vec{a}$ denotes the coefficient vector. This function assigns each point a value D. The coefficients have to be chosen in such a way that the separation between signal and background events is maximal. In fact D is a projection of the

2 classes which should maximize the distance between the two class centers (defined by the class mean values) and minimize the distance within the classes. Therefore, the Matrix M is introduced

$$\mathbf{M} = (\vec{m}_1 - \vec{m}_2)(\vec{m}_1 - \vec{m}_2)^T \tag{6.13}$$

which measures the the quadratic distance of the class centers. The problem can then be rewritten as a maximization problem of the following equation:

$$J(\vec{a}) = \frac{\vec{a}^T \mathbf{M} \vec{a}}{\vec{a}^T \mathbf{T} \vec{a}} \tag{6.14}$$

This problem can be solved using the variation principle. It leads to an eigenvector problem, where the eigenvector assigned to the largest eigenvalue solves the problem:

$$\vec{a} = \mathbf{T}^{-1}(\vec{m}_1 - \vec{m}_2) \tag{6.15}$$

A way to distinguish the two classes is then to introduce a cut a_0 on the discriminant distribution $D(\vec{X})$. This cut value a_0 has to be chosen according to the specific classification problem considered. If $D(\vec{X}) < a_0$ for a given test event it belongs to class 1, if $D(\vec{X}) > a_0$ it belongs to class 2. This algorithm works optimal if the considered variables are Gaussian distributed. A detailed description of the Fisher Discriminant analysis can be found in [85].

6.2.2 Nonlinear Discriminant Analysis

In a two-dimensional parameter space the cut a_0 calculated by the Fisher discriminant analysis corresponds to a straight line in this parameter space. For more complicated classification problems it is desirable to have more degrees of freedom in choosing the separation function. For example, if the two classes considered, overlap partially or have shapes that cannot be separated by straight lines Fisher's algorithm is not optimal. One way to improve the algorithm is to use a nonlinear separation function. In this analysis a quadratic function in the variables $\vec{X}$ is used:

$$D(\vec{X}) = (\vec{a} + \mathbf{B}\vec{X}) \cdot \vec{X} \tag{6.16}$$

By introduction of new variables $\vec{X}'$ which are defined by

$$\vec{X}' = (\vec{X}_1, \vec{X}_2, \ldots \vec{X}_N, \vec{X}_1\vec{X}_1, \vec{X}_1\vec{X}_2, \ldots \vec{X}_1\vec{X}_N, \ldots \vec{X}_N\vec{X}_N)^T \tag{6.17}$$

and new coefficients

$$\vec{a}' = (a_1, a_2, \ldots a_N, B_{11}, B_{12}, \ldots B_{NN})^T \tag{6.18}$$

the classification problem can be linearized and reduced to the problem solved by Fishers algorithm in the new

$$N_F = \frac{1}{2}(N^2 + 3N) \tag{6.19}$$

dimensional parameter space. Hyperplanes in this parameter space correspond to hyperboloids in the N-dimensional parameter space.

6.2.3 Iterated Discriminant Analysis

In order to improve the separation power the nonlinear discriminant algorithm is repeated twice [88]. All events that survive the first iteration cut a_0 are input to the second iteration. In this analysis several different background channels (C_b) are considered. These background channels differ in the corresponding cross sections ($\sigma^{c,b}$) or number of expected events and the population of phase space regions. To combine these channels to a common background class the weighted average of the mean values m and the covariance matrices T was used. The weight was defined by the corresponding cross section ratio.

$$\vec{m}_b = \frac{1}{w_b} \sum_{c=1}^{C_b} \sigma^{b,c} \vec{m}_c \tag{6.20}$$

$$\mathbf{T}_b = \frac{1}{w_b} \sum_{c=1}^{C_b} \sigma^{b,c} \mathbf{T}_c \tag{6.21}$$

$$w_b = \sum_{c=1}^{C_b} \sigma^{b,c} \tag{6.22}$$

The signal efficiencies for each iteration of the algorithm have to be chosen. With this choice the cut on the discriminant a_0 is determined. In the implementation of the algorithm used in this analysis, the signal efficiency of the first step is 90% and for the second step it is 70%. This choice granted sufficient Monte Carlo statistics for the second iteration.

Chapter 7

Cutbased Separate Single Top Search

In this chapter the results of the cutbased separate t- and s-channel Single Top Search based on $Q \cdot \eta$ for the 1-b-tag subsample and the number of events for the double-b-tag subsample using an integrated luminosity of 162 pb^{-1} are presented. A likelihood technique described in the previous chapter based on $Q \cdot \eta$ in the 1-tag subsample and the number of observed events in the 2-tag subsample is used. Here Q is the charge of the lepton and η is the pseudorapidity of the non-b-tagged jet. In the next section the corresponding distributions will be presented.

The event detection efficiency and the number of expected event was calculated for several event selection scenarios. For all these scenarios the expected sensitivity was estimated and the scenario yielding the highest sensitivity is chosen.

7.1 The $Q \cdot \eta$ distribution in the 1-tag subsample

As already mentioned the observable $Q \cdot \eta$ was chosen as variable to be used in the likelihood function for the 1-tag subsample. Figure 7.1 shows the probability densities as a function of $Q \cdot \eta$ in 16 bins of width 0.4. The entries in the outer bins arise due to jet corrections taking the primary vertex position into account. Thus uncorrected jets with a pseudorapidity $|\eta_{\text{detector}}| < 2.8$ can result in a corrected $|\eta| > 2.8$. The t-channel signal peaks in forward direction, whereas the background distributions peak in the central region. The asymmetry of the t-channel distribution is due to the parton distribution function of the proton, since a produced t ($\bar{t}$) is dominantly associated with a light quark (antiquark) jet propagating in the proton (antiproton) direction. This quark (antiquark) jet originates from the W-Boson exchange of the valence quark (anti-quark). The peak in negative regime dominantly arises from the down

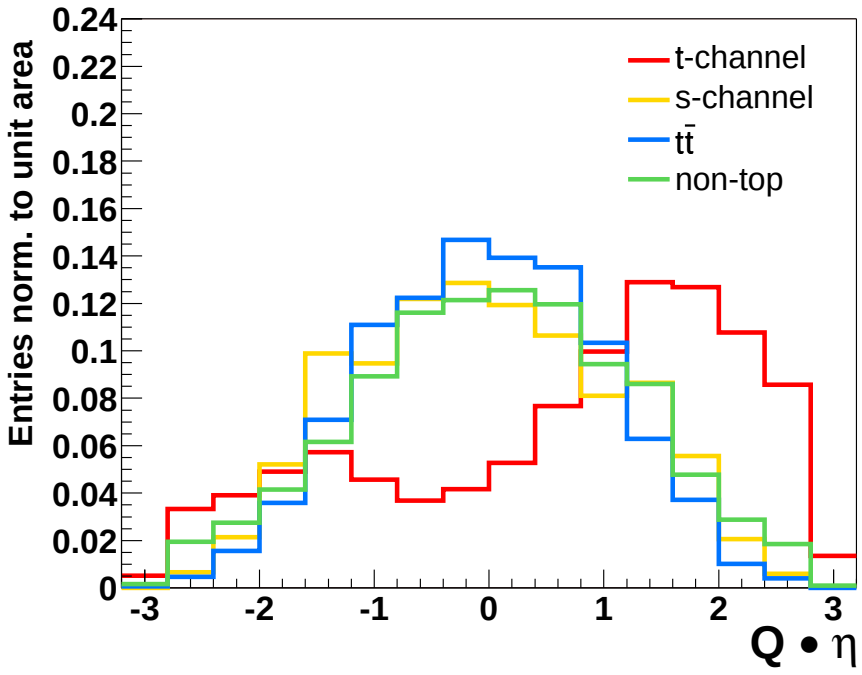

Figure 7.1: $Q \cdot \eta$ distributions. Monte Carlo templates normalized to unit area.

quark component of the proton (antidown quark component of the antiproton) involved in single top production. In these processes antitop quarks are produced and thus $Q \cdot \eta$ is negative. Since the proton consists of two valence up type quarks and one down type quark a asymmetry is detected. This distribution is a strong discriminant for t-channel signal events in comparison to s-channel and background events. The distributions shown here are derived by requiring 140 GeV/c^2 $< \mathrm{M}_{\ell\nu\mathrm{b}} <$ 210 GeV/c^2 and $E_{\mathrm{T}} > 30$ GeV/c for the leading jet. The distributions are basically identical for all considered scenarios. The non-top background distribution is the sum of the individual contributions weighted by their contributions to this background class. Figure 7.2 depicts the individual contributions.

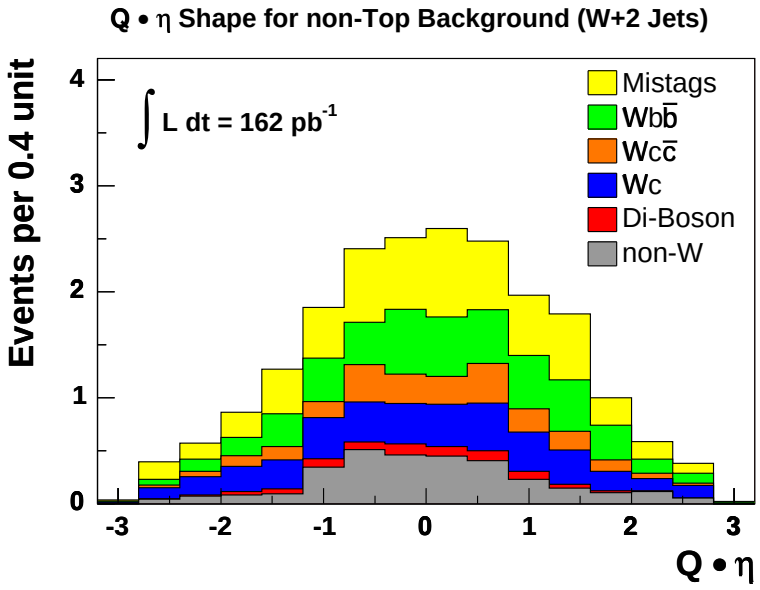

Figure 7.2: $Q \cdot \eta$ distributions for the non-top backgrounds. Monte Carlo templates normalized to the number of expected events.

7.2 Optimization

The available data set and the significance of the signal with respect to the large backgrounds is not large enough to measure or discover single top production and thus this analysis will concentrate on setting upper limits on electroweak single top production. Therefore, the given scenarios have been evaluated and the expected upper limits on single top production has been calculated assuming Standard Model production. In the following subsection the method to derive the expected upper limit or a-priori sensitivity will be explained.

7.2.1 A-priori Sensitivity

In order to estimate the median limit that can be set on Standard Model single top production associated to a given scenario randomly generated CDF pseudo-experiments are used. The procedure it the following:
A Poisson distributed random number according to the number of expected events for each channel in the 1-tag and 2-tag subsample is thrown. The resulting numbers are the events obtained for the signal and background processes in the samples. For each obtained events a second random number is drawn according to the probability density assigned to the corresponding $Q \cdot \eta$ template histogram. By this procedure each pseudo event is assigned to a $Q \cdot \eta$ value. All these events are then accumulated and for a pseudo data set corresponding to an integrated luminosity of $\mathcal{L} = 162$ pb^{-1}. A likelihood function is then used to calculate the 95% C.L. upper limit for each experiment. This technique is described in the previous chapter. Since especially the integration process of the errors is very time consuming for a huge number of pseudo experiments, the procedure given there concerning the treatment of errors was simplified for this optimization process. Instead of integrating out all nuisance parameters the likelihood function is calculated in the absence of systematic uncertainties. The resulting function is then convoluted with a Gaussian function accounting for the errors.

$$L_{sm}(\beta) = \int_{-\infty}^{+\infty} L(\beta') \cdot \frac{1}{\sigma(\beta)\sqrt{2\pi}} \exp\left(-\frac{1}{2}\left(\frac{\beta - \beta'}{\sigma(\beta)}\right)^2\right) d\beta' \qquad (7.1)$$

with $\sigma(\beta) = \sigma_{\text{norm}} + \beta\sigma_{\text{shape}}$ and $\beta = \sigma_{\text{signal}}/\sigma_{\text{SM}}$. This likelihood is then integrated and the according limit calculated.

This procedure is repeated 20000 times and the obtained median limit defines the a-priori sensitivity of the given scenario.

7.2.2 Choice of the Cut Scenario

Five different analysis scenarios have been involved in the optimization process. A normalization uncertainty of 20% and and shape uncertainty of 20% are as-

No.	scenario	a-priori limit
1	b-tag	16.4 pb
2	$M_{\ell\nu b}$	12.2 pb
3	$M_{\ell\nu b} \oplus E_T(\text{jet } 1)$	11.8 pb
4	$M_{\ell\nu b}$ and 1-b-tag	12.2 pb
5	$M_{\ell\nu b}$, $E_T(\text{jet } 1)$ and 1-b-tag	11.5 pb

Table 7.1: Summary table of a-priori sensitivity for different cut scenarios.

sumed to evalute these scenarios. The following scenarios have been investigated for the t-channel production only:

1. All events after b-tagging.
2. Add $M_{\ell\nu b}$.
3. Add $M_{\ell\nu b}$ and $E_T(\text{jet } 1)$ cut.
4. Add $M_{\ell\nu b}$ and use only events with exactly 1-b-tag.
5. Add $M_{\ell\nu b}$ and $E_T(\text{jet } 1)$ cut and use only events with exactly 1-b-tag.

In these scenarios the s-channel is treated as background process. The obtained a-priori sensitivities are listed in table 7.1. Scenario No. 5 leads to the highest a-priori sensitivity for the t-channel, thus this scenario will be used. To gain sensitivity for the s-channel process the 2-tag subsample is added to this scenario. Within the 2-tag subsample three different requirements have been tested:

6. Use number of observed 2-tag events after $M_{\ell\nu b}$ cut.
7. Use a 6 bin likelihood function based on $M_{\ell\nu b}$ in the 2-tag subsample.
8. Use a 6 bin likelihood function based on E_{T} in the 2-tag subsample.

Table 7.2 list the obtained a-priori sensitivities for the combination of the two subsamples. All considered scenarios revealed the same sensitivity for the s- and the t-channel production. The best choice obtained is the scenario using the number of events in the 2-tag samples, because for this scenario the uncertainties to be considered arise from acceptance uncertainties only. Thus, scenario No.6 will be used for this analysis.

No.	scenario	a-priori limit t-ch.	a-priori limit s-ch.
6	only 2-b-tag bin	10.9 pb	10.5 pb
7	$M_{\ell\nu b}$ in 2-b-tag bin	10.9 pb	10.4 pb
8	E_T(jet 1) in 2-b-tag-bin	10.9 pb	10.3 pb

Table 7.2: Summary table of a-priori sensitivity for different cut scenarios.

7.3 Evaluation of Systematic Uncertainties

As already mentioned when introducing the likelihood function seven sources of systematic uncertainties have been considered.

- The uncertainty assigned to the jet energy scale, which is the uncertainty assigned to the jet energy measurement and the jet energy corrections (JES)
- The uncertainty in modeling initial state radiation (ISR)
- The uncertainty in modeling final state radiation (FSR)
- The uncertainty assigned to the choice of the parton distribution function (PDF)
- The uncertainty due to the choice of the signal modeling (Monte Carlo Generator)
- The uncertainty arising from the measurement of the top quark mass
- The uncertainties due to the measurements of trigger and b-tagging efficiencies and uncertainties due to the luminosity measurement

The effect of the jet energy scale uncertainty is estimated by application of a function to all jets describing $\pm 1\sigma$ variations of this effect. The acceptance has then been recalculated using these modified datasets. To evaluated the uncertainty due to the change in the $Q \cdot \eta$ distributions the template histograms for each variation have been created and the relative error with respect to the standard distribution has been evaluated for each bin. In the 2-tag subsample there are no shape uncertainties present, since a counting method is used. The estimation of the uncertainties due to the modeling of initial and final state radiation is based on Monte Carlo Samples using two different models to describe these processes. After calculation of the acceptances half the difference between these tunes is taken as the estimator for the uncertainty. To evaluate the uncertainty due to the choice of a specific PDF parametrization several different PDF sets were used. The maximum deviation obtained by the MRST72

parametrization from our standard choice CTEQ5L was used for the PDF uncertainty. To estimate the uncertainty due to the signal modeling the TopRex Monte Carlo samples have been evaluated. Half the difference between the obtained MadEvent and TopRex deviations define the 1σ error. To estimate the effects due to the top quark mass uncertainty Monte Carlo samples generated with a top quark mass of 170 GeV/c^2 and 180 GeV/c^2 have been evaluated and compared to the standard choice of 175 GeV/c^2. All the mentioned effects so far contribute to an uncertainty in the acceptance and in the probability density function, that is here the $Q \cdot \eta$ distribution. The last source of uncertainty contributes only to the acceptance uncertainties. These errrors are added in quadrature, the major contribution arise due to b-tagging (7%) and from the luminosity measurement(6%).
Due to the low statistics in the 2-tag subsample the errors have been evaluated in the 1-tag sample only. Identical errors are assumed for the 2-tag subsample. Table 7.3 summarizes the acceptance uncertainties due to systematic errors for the two signal processes. Table 7.4 lists the considered systematic uncertainties for the backgrounds.

No.	Source	t-channel	s-channel
1	Jet energy scale	$^{+2.4}_{-6.7}$%	$^{+0.4}_{-3.1}$%
2	ISR	±1.0%	±0.6%
3	FSR	±2.2%	±5.3%
4	PDF	±4.4%	±2.5%
5	Generator	±5%	±2%
6	Top quark mass	$^{+0.7}_{-6.9}$%	-2.3%
7	ϵ_{trig}, ϵ_{ID}, luminosity	±9.8%	±9.8%

Table 7.3: Systematic acceptance uncertainties for t- and s-channel single-top signal.

No.	Source	$t\bar{t}$	non-top
1	Jet energy scale	$^{+25}_{-20}$%	±15.1%
6	Top quark mass	±4.4%	—

Table 7.4: Systematic acceptance uncertainties ϵ_{ij+} and ϵ_{ij-} for $t\bar{t}$ and non-top background.

For each systematic sample also shifted template histograms have been created and the difference to the standard templates have been calculated. Some examples for the $q \cdot \eta$ histogram are shown in Fig. 7.3.

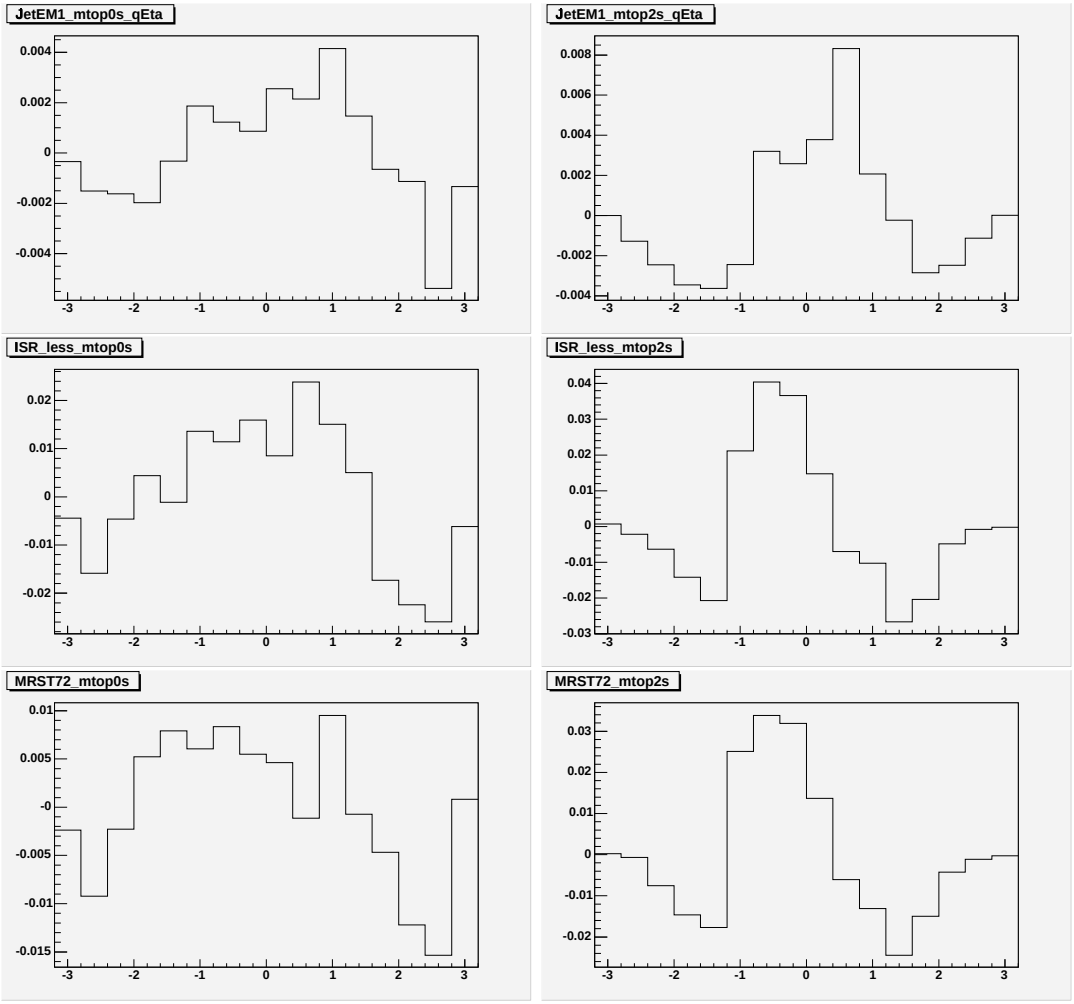

Figure 7.3: Changes of $Q \cdot \eta$ template histograms due to systematic uncertainties for t- and s-channel single-top.

7.4 Apriori Sensitivity including Systematic Uncertainties

After having calculated the uncertainties the expected limit using pseudo experiments and the full likelihood function can be performed. Here all nuisance parameters are properly integrated out and the errors are treated properly. The technique of pseudo experiments was describes in the optimization section of this chapter. For the Gaussian priors constraining the background cross section $\Delta_3 = 23\%$ for $t\bar{t}$ and $\Delta_4 = 20\%$ for non-top backgrounds is used. Several thousand pseudo experiments have been created and the mean limit is evaluated for s- and t-channel single top production. If the s-channel single top production cross-section limit is calculated Standard Model t-channel production within the 13% uncertainty is assumed and vice versa.

Figure 7.4 depicts the s-channel limit distribution of such 5840 CDF pseudo-

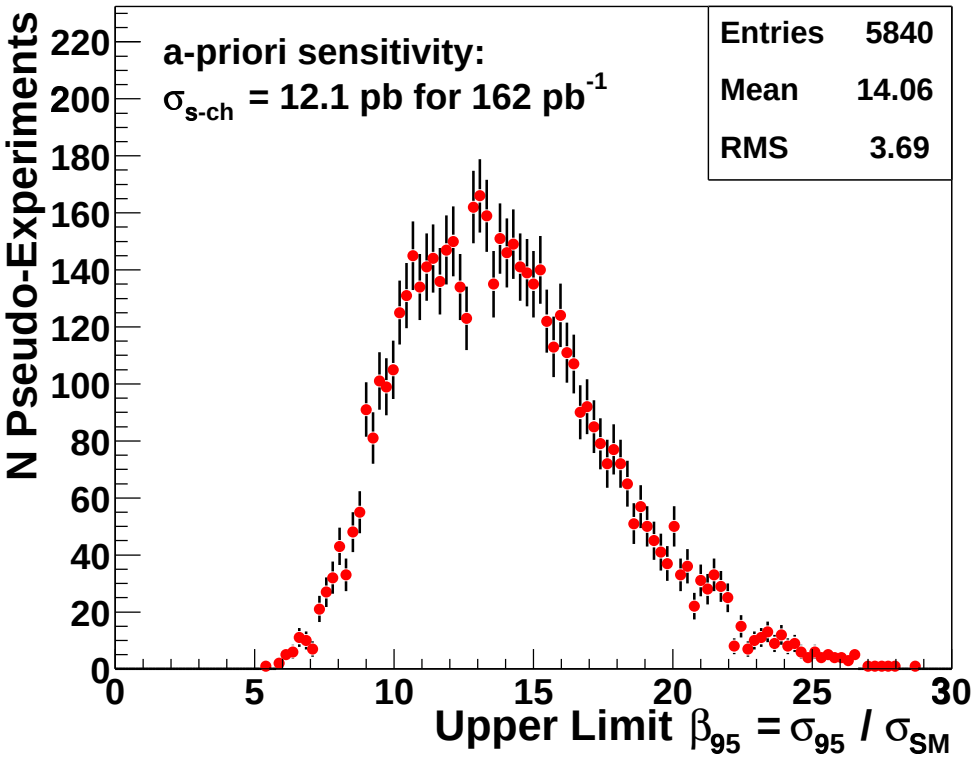

Figure 7.4: The distribution of the *s*-channel single top limits normalized to the SM cross-section assuming SM production and an integrated luminosity of 162 pb^{-1}.

experiments. All sources of systematic uncertainties have been integrated out for an individual experiment. The median limit one could expect to set on s-channel production with our event-selection assuming SM production is 12.1 pb. This

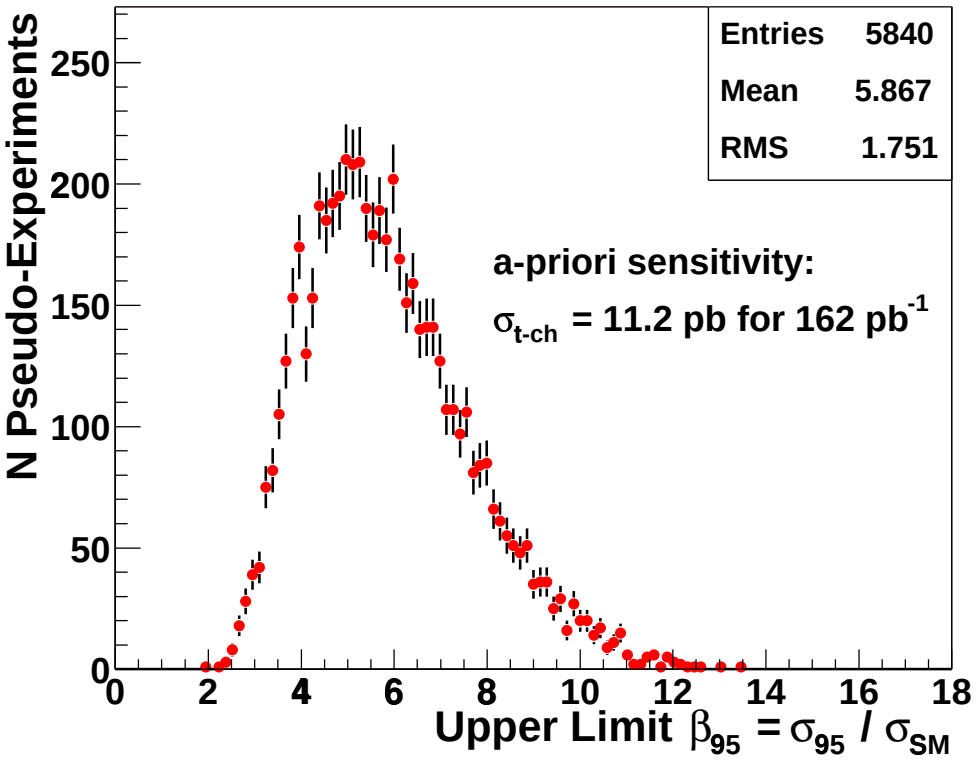

Figure 7.5: The distribution of the t-channel single top limits normalized to the SM cross-section assuming SM production and an integrated luminosity of 162 pb^{-1}.

value corresponds to a β-value of 13.75, which is defined by the cross-section limit in units of the SM cross-section. We have chosen the median of the distribution as figure of merit for our sensitivity since the mean value would weight the tails of the distributions stronger.
Figure 7.5 presents the corresponding distribution of the t-channel limits using the identical 5840 CDF pseudo-experiments. The limit we would here expect to set on SM t-channel single top production is 11.2 pb corresponding to a β-value of 5.65.
The sensitivity for the t-channel is much higher compared to the s-channel. This is mainly due to the higher SM cross-section and to larger statistics in the 1-tag-subsample in which almost all t-channel events are reconstructed. Another reason is the use of a binned likelihood function based on $Q \cdot \eta$ which increases our sensitivity in comparison to a likelihood based on the number of observed events.

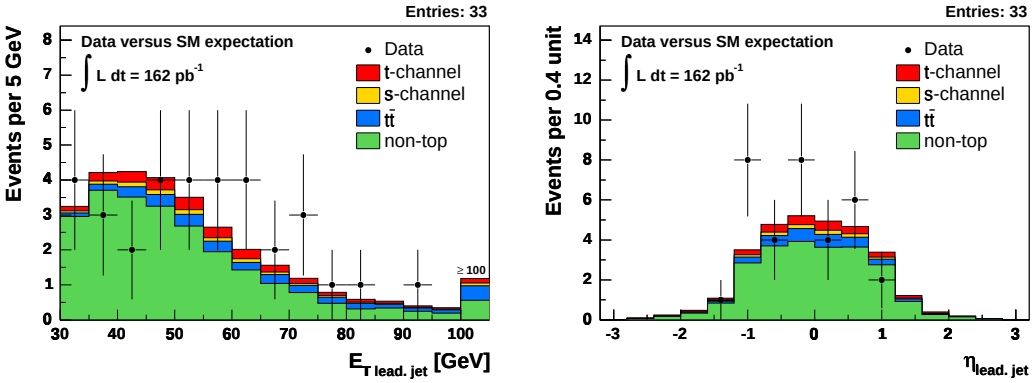

Figure 7.6: The transverse energy distribution (left) and the η distribution (right) of the leading jet of the 1-tag-subsample compared to the SM expectation.

7.5 Comparison of Data and SM Expectation

In this section we present kinematic distributions of the data compared to the Standard Model expectation. All distributions exhibit a good agreement of data and the SM expectation in the 1-tag-subsample. The expectations of signal and background rates are summarized in Table 7.5. In the double-tag subsample the small surplus in the number of observed events is clearly present. In this section some kinematic distributions are compared to the expectation. Figure 7.6 presents transverse energy distribution of the leading jet and the pseudorapidity distribution of 1-tag events. For single top signal events this jet originates from the bottom quark of the top decay with a probability of about 80%.

Figure 7.7 shows the transverse energy distribution and the pseudorapidity distribution of the trigger lepton in 1-tag events. This distribution ranges from -1.1 to +1.1 due to the coverage of the central muon chambers and the central outer tracker (COT) needed for the electron trigger.

Figure 7.8 shows the invariant mass distribution of the bottom jet assigned to the top quark and reconstructed W-Boson candidate and the dijet mass of the two jets for the 2-tag-subsample. In these distributions a small surplus is present.

Figure 7.9 shows the $Q \cdot \eta$ distribution we use to extract the single top content in the 1-tag-subsample. There is lack of events in the forward region of this observable. In this regime the signal probability achieves its maximum value.

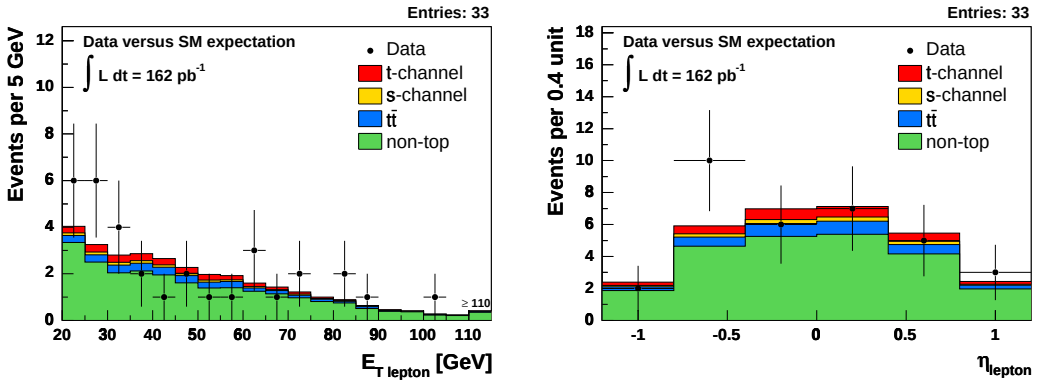

Figure 7.7: The transverse energy distribution (left) and the η distribution (right) of the lepton in the 1-tag-subsample compared to the SM expectation.

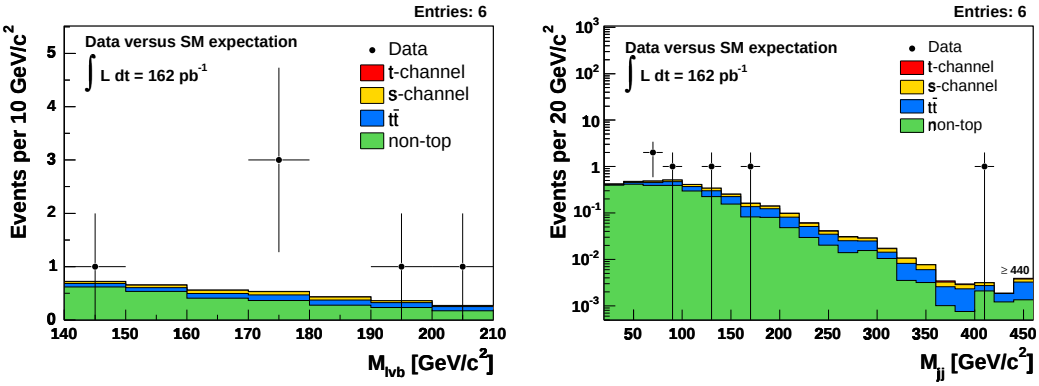

Figure 7.8: The reconstructed $M_{\ell\nu b}$ (left) and the invariant dijet mass distribution (right) in the 2-tag-subsample compared to the SM expectation.

Process	N events in separate search	
	1-b-tag-bin	double-tag-bin
$t\bar{t}$ ($\sigma = 6.70^{+0.71}_{-0.88}$ pb)	3.2 ± 0.7	0.60 ± 0.14
non-top	23.3 ± 4.6	2.59 ± 0.71
Sum Background	26.5 ± 4.7	3.19 ± 0.72
t-channel ($\sigma = 1.98 \pm 0.26$ pb)	2.7 ± 0.4	0.02 ± 0.01
s-channel ($\sigma = 0.88 \pm 0.11$ pb)	1.1 ± 0.2	0.32 ± 0.05
Sum Single-Top	3.8 ± 0.5	0.34 ± 0.05
Sum Expected	30.3 ± 4.7	3.53 ± 0.72
Observed	33	6

Table 7.5: Expected number of signal and background events passing all selection cuts in the W+2 jets data sample for (162 ± 10) pb^{-1} of CDF II data, compared with observations.

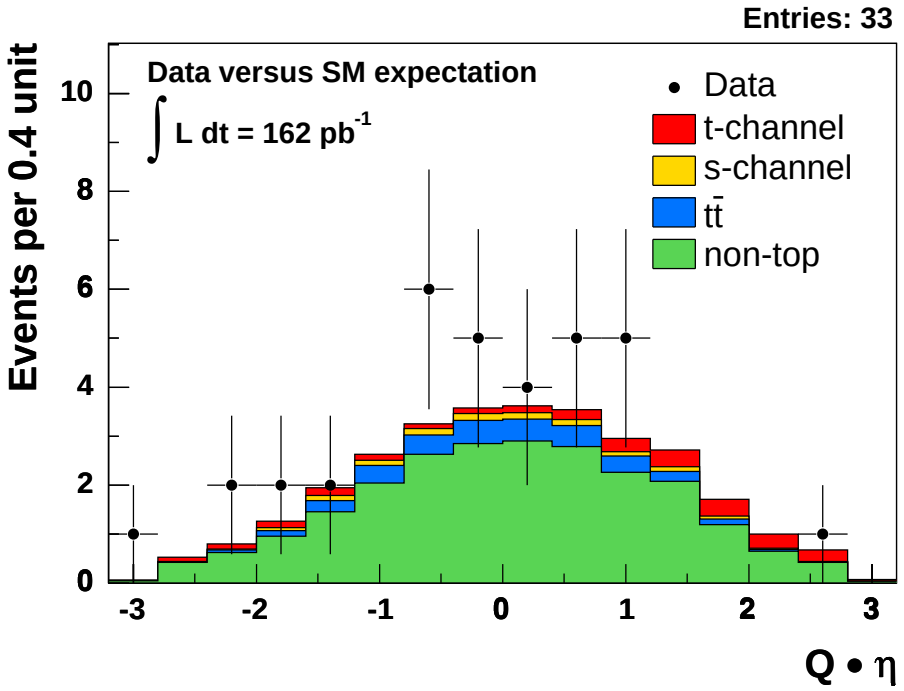

Figure 7.9: The $Q \cdot \eta$ distribution in the 1-tag-subsample compared to the SM expectation.

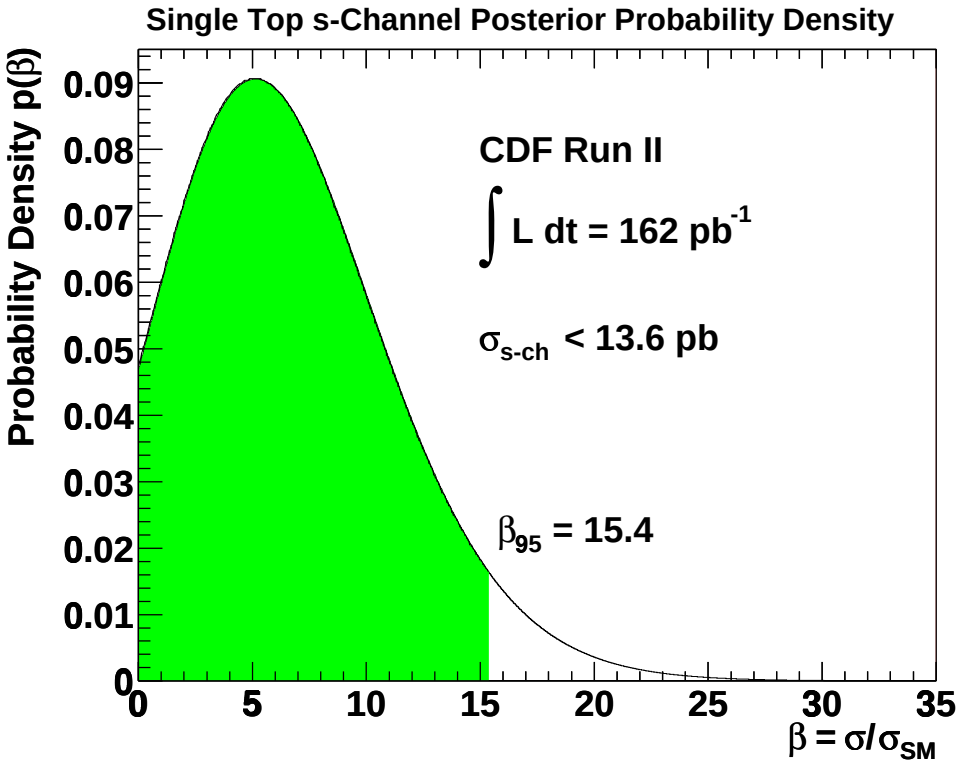

Figure 7.10: The posteriori s-channel probability density for the CDF data. The full curve represents 95% of the area below the probability density.

7.6 Results

In this section the a-posteriori limits for s- and t-channel single top production cross section using 162 pb^{-1} CDF data are presented. Figure 7.10 shows the posteriori probability density for s-channel single top production as a function of the β parameter. The posteriori probability density is calculated by the likelihood function times the prior density, which is here the Heaviside function. The choice of this function reveals the fact that any physical cross section has to be non-negative. Due to the small surplus in the 2-tag-subsample the probability density peaks at $\beta = 5.2$. Thus there is a high probability that there are s-channel events present in the sample. The upper limit we obtain for s-channel single top production is 13.6 pb. This corresponds to a β-value of 15.4. This value is slightly higher than the one expected in pseudo-experiments.

Figure 7.11 shows the posteriori probability density for t-channel single top production. Here the likelihood peaks at zero. Thus the most probable value within this dataset is zero, meaning that with high probability there are no t-channel signal events in the data sample. This is also revealed in the corresponding limit of 10.1 pb which is smaller than the apriori sensitivity. This can be explained by

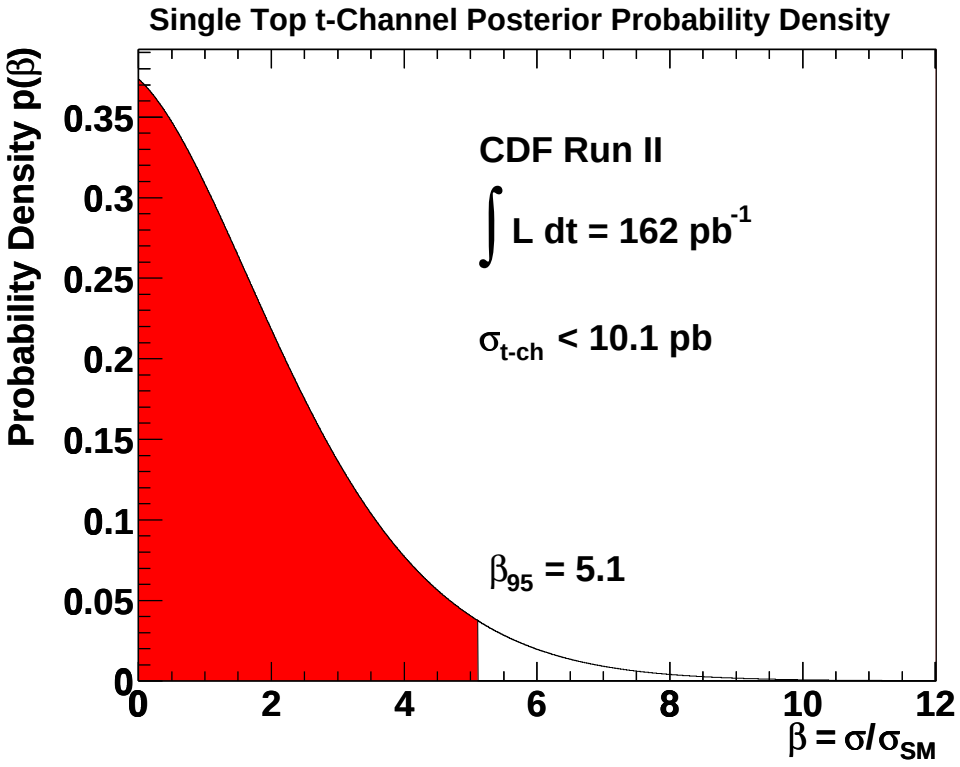

Figure 7.11: The posteriori s-channel probability density for the CDF data. The full curve represents 95% of the area below the probability density.

the lack of events in the very positive region of the $Q \cdot \eta$ distribution. Table 7.6 summarizes the most probable value, the value at with the 95% confidence level is reached in units of the SM cross-section and the limit obtained using the CDF dataset of 162 pb^{-1} luminosity. The quoted uncertainties for the most probable values are the highest posterior density (HDP) intervals of the likelihood function. This interval is defined by the two values of β covering 68% of the total probability around the maximum while minimizing the distance $\delta\beta$ between them. Since the maximum value for the t-channel is found at $\beta = 0$ the lower edge of the interval is set to zero.

A this analysis was published in reference [89].

Process	MPV $\pm$ HPD $[pb]$	expected limit $[pb]$	observed limit $[pb]$
t-channel	$0.0^{+4.7}_{-0.0}$	11.2	10.1
s-channel	$4.6^{+3.8}_{-3.8}$	12.1	13.6

Table 7.6: Summary of the upper limits at the 95% C.L. and the most probable values of the single top cross sections.

Chapter 8

Separate Single Top Search using IDA

In this chapter a separate s- and t-channel single top quark production search using an iterated discriminant analysis (IDA) is presented. The main goal of applying such a multivariate technique is to increase the sensitivity of our search. This is necessary to achieve a discovery or an exclusion of Standard Model single top production given the current integrated luminosity expectations for Tevatron Run II.
The sensitivity for this search is defined by $\rho = N_{\mathrm{sig}}/\sqrt{N_{\mathrm{back}}}$. Here N_{sig} denotes the number of signal events and N_{back} is the sum of all background events. Thus, ρ gives a measure for the probability that the number of signal events can be consistent with statistical fluctuations of the backgrounds. The smaller ρ is the higher is this probability.

8.1 Iterated Discriminant Analysis (IDA)

The technique of such an iterated discriminant analysis is described in section 6.2. A nice feature of such a technique is that different observables can be combined to a single discriminant. Thereby, this discriminant is calculated using the mean values of the covariance matrices for the signal and background channels. The strategy of this analysis is the following: The largest expected backgrounds in the lepton+2 jets data sample are due to W+jets contributions. Therefore, the goal of applying this technique is to suppress these backgrounds. In the previous chapter the optimization process revealed that the splitting of the sample according to the number of assigned b-tags is a very good tool to gain sensitivity for the s-channel without harming the t-channel sensitivity. Therefore, the sample is divided in the 1-tag and the 2-tag subsamples. For the 2-tag subsample the scenario as used in the cutbased search is chosen. For the 1-tag subsample to which the IDA algorithm is applied the starting point is the event

Process	$N_{\text{events}}^{\text{btag=1}}$	$N_{\text{events}}^{M_{\ell\nu b}}$
t-channel	3.35±0.54	3.25±0.52
s-channel	1.81±0.29	1.55±0.26
$t\bar{t}$	6.90±1.52	4.33±1.00
non-top	66.07±10.43	60.0±9.30
Total	78.18±10.56	69.13±9.37
Observed	70	63

Table 8.1: Summary of the expected events in the 1-tag subsample with and without application of the $M_{\ell\nu b} < 220$ GeV/c^2 requirement.

selection after requiring exactly one b-tagged jet in the 2-jet sample. The number of expected events for signal and background processes considered is given in table 8.1. Here $N_{\text{events}}^{\text{btag=1}}$ denotes the number of events to be expected after requiring exactly one b-tagged jet. $N_{\text{events}}^{M_{\ell\nu b}}$ is the subset of events also fulfilling $M_{\ell\nu b} < 220$ GeV/c^2. This requirement efficiently suppresses $t\bar{t}$ background. In order to calculate the discriminant in the two steps of the algorithm the signal class is made of t-channel single top Monte Carlo data, whereas the background class consists of a composition of $Wb\bar{b}$, $Wc\bar{c}$ and mistag Monte Carlo events. These Monte Carlo samples have been described in the chapter 5. The next subsection describes the input variables used for the algorithm.

8.1.1 Input Variables

In this section the set of observables used as input for the IDA algorithm is described. In total 8 observables are used for the analysis. The chosen observables are:

1. The reconstructed mass $M_{\ell\nu b}$
2. The transverse momentum of the reconstructed neutrino (p_{T})
3. $Q \cdot \eta$ as used in the cutbased search
4. The cosine of polarization angle θ of the reconstructed top candidate
5. The H_{T} value assigned to an event
6. The transverse momentum of the leading jet in the event
7. The logarithm of the $\Delta_{1,2}$ value obtained by the K_{T} jet clustering algorithm

8. The logarithm of the $\Delta_{2,3}$ value obtained by the K_{T} jet clustering algorithm

Two criteria were used to choose these variables: (1) The data is well described prior to applying the algorithm and (2) The variables a good discrimination of t-channel signal from the backgrounds. This discrimination power has been determined by subsequently adding one variable to the algorithm and comparing the estimated significance $\rho = N_{\mathrm{sig}}/\sqrt{N_{\mathrm{back}}}$. The substitution of one of these variables by the transverse momentum of the second leading jet decreased to significance for instance. The following additional variables have been investigated:

- The invariant mass of the lepton, the neutrino candidate and the non b-tagged jet.
- The W boson helicity, which is a good discriminant; unfortunately it could not be used. The expected distribution does not describe the data. This is caused by the use of a non isolated lepton sample to model QCD background contributions. This sample peaks at low values of the cosine of the helicity angle, whereas due to the isolation requirement for the leptons no data events are present.
- The transverse momentum of the second leading jet.
- The sum of the longitudinal momenta of all jets ($\Sigma p_{\mathrm{z,i}}$).
- Sphericity ($= 3/2(Q_1 + Q_2)$), here the Q_i are the 2 smallest eigenvalues of the normalized event momentum tensor, defined by $\frac{\sum_i p_i^a p_i^b}{p_i^2}$. The indices a and b run over the three spacial dimensions and the summation runs over the jets, the lepton and $\not\!\!E_T$.
- Aplanarity ($= 3/2(Q_1)$), here Q_1 is the smallest eigenvalue of the normalized event momentum tensor.
- The invariant dijet mass of the two jets.

By the use of nine variables instead of eight the significance ρ is increased by 1.5% for the combination yielding the highest ρ value.

The reconstruction of the invariant mass $M_{\ell\nu b}$ and the neutrino momentum is described in chapter 4. The polarization angle of the top candidate is reconstructed by determining the angle of the lepton and the untagged jet in the top quark rest frame. The cosine of this angle is expected to be a good discriminant with respect to the backgrounds, since the top quarks are nearly 100% polarized in the t-channel production channel. In about 2/3 of the events the polarization axis is the untagged jet, in the remaining 1/3 of events it is the beam axis.
H_{T} is defined as the scalar sum of the transverse momenta of the jets, the lepton

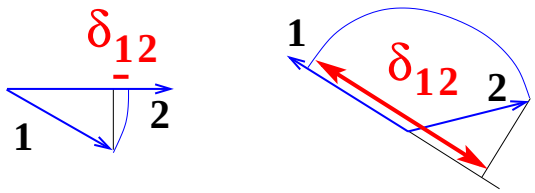

Figure 8.1: Illustration of the $\Delta_{1,2}$ calculation. Number 1 and 2 denote the jets of the event. The left hand figure shows a situation where the Δ parameter is small. In such a case it is relatively easy to merge the two jets. In contrast the right hand plot depicts a situation where the Δ parameter is large. Here the jets cannot be easily merged.

and missing transverse energy.
The $\Delta_{n,n+1}$ values are defined by the following equation:

$$\Delta_{n,n+1} = min(\delta_{i,j}) \text{ with } \delta_{i,j} = \frac{min(E_i^2, E_j^2)(1 - \cos\alpha_{ij})}{D^2} \tag{8.1}$$

Here D^2 is an arbitrary energy scale. n corresponds to the number of jets that are assigned to the event and E_i is the energy of the jet i. α_{ij} denotes the angle between the two considered jets. Figure 8.1 geometrically illustrates $\Delta_{1,2}$. This variable is a measure for the merging of 2 jets into one. For the calculation of Δ all jet objects with an transverse energy exceeding 8 GeV in the event are considered.
Since the $M_{\ell\nu b} < 220$ GeV/c^2 requirement efficiently suppresses $t\bar{t}$ background this cut is also applied to the following distributions.

Figure 8.2 depicts the $M_{\ell\nu b}$ distribution and the transverse momentum distribution for the neutrino candidate for the data (dots) and the expectation for the 1-tag subsample. The non-top contribution is made of the W+heavy flavor, the mistags, the QCD multijet and the diboson contributions weighted by the number of expected events according to the method 2 calculation. Figure 8.3 shows the comparison of CDF data to the expectation concerning the observable lepton charge times pseudo rapidity η of the untagged jet. The plot on the right hand depicts the cosine of the reconstructed polarization angle θ for the top candidate. The dip in this distribution for large values of $\cos\theta$ can be explained by the jet reconstruction. Since a clustering algorithm of cone size 0.4 is used, leptons that fall into this cone around the jet axis are assigned to this jet and not identified. Since this angle is used in the top decay frame the suppression in the outer bins is washed out. Figure 8.4 depicts the comparison of the sum of the transverse momenta assigned to an event and the transverse momentum distribution of the leading jet. Figure 8.5 shows the distributions of the logarithm of the Δ parameters obtained by the K_{T} algorithm. In general, we

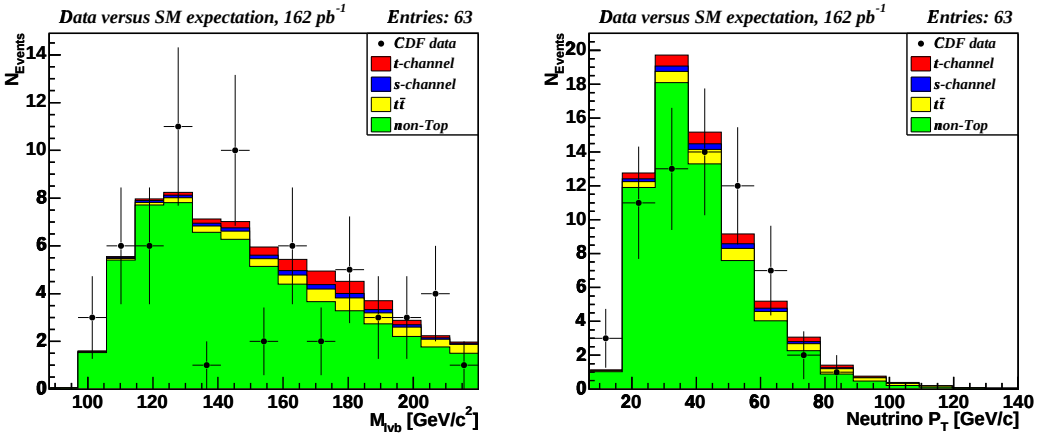

Figure 8.2: The M_{lvb} distribution (left) and the transverse momenta of the neutrino candidates (right).

conclude that the data distributions of the relevant variables are well described by our Monte Carlo model.A use of these variables in a multivariate technique is thus warranted.

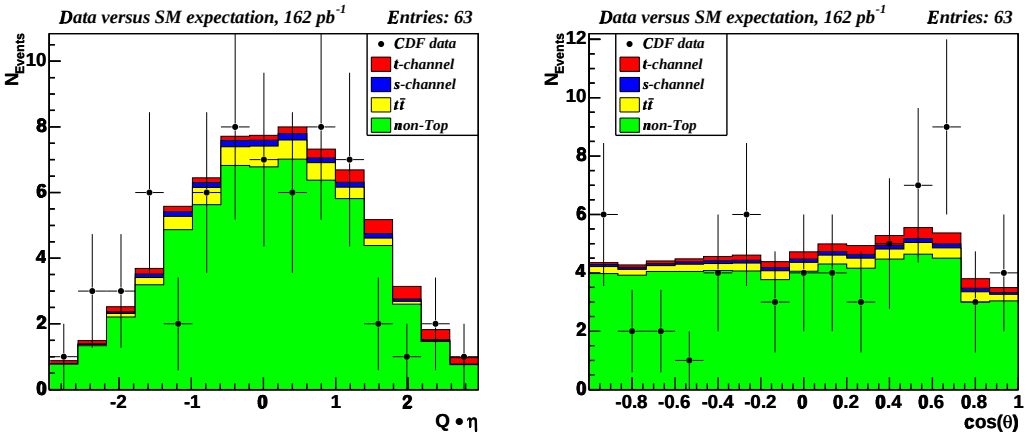

Figure 8.3: The $Q \cdot \eta$ distribution (left) and the cosine of the polarization angle distribution of the top quark candidate (right).

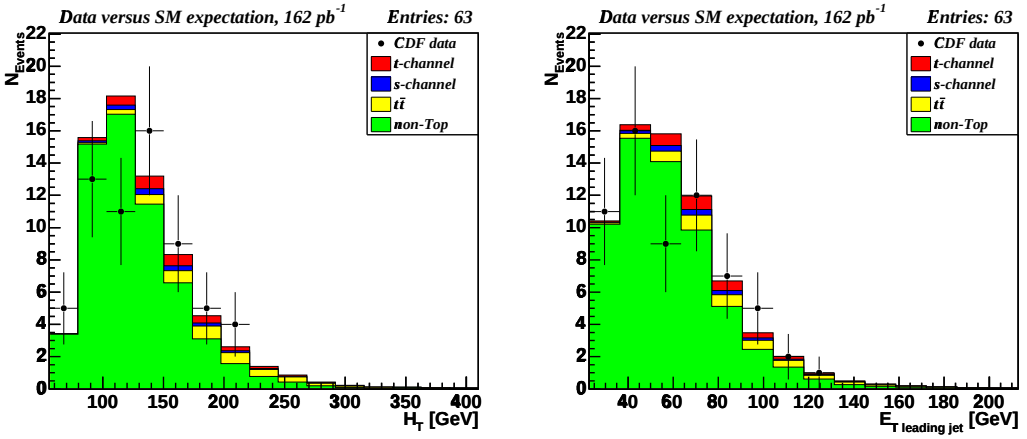

Figure 8.4: The H_T distribution (left) and the transverse momenta of the leading jet (right).

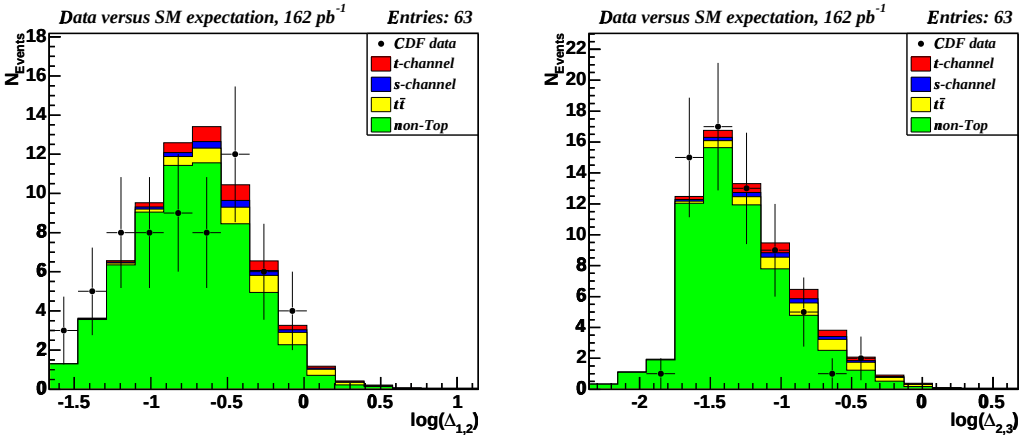

Figure 8.5: The Δ-parameter distributions calculated by the K_T algorithm.

8.1.2 Training

In order to derive the test statistic and thus calculate the coefficients for the IDA transformation a t-channel signal sample and a background sample consisting of a mixture of Monte Carlo $Wb\bar{b}$, $Wc\bar{c}$ and $W+2$jets events have been used. The $W+2$ jets sample is used to model the mistags. The contributions are weighted by their expected contribution to the 1-tag subsample. In order to suppress the $t\bar{t}$ content an $M_{\ell\nu b} < 220$ GeV/c^2 requirement has been added. This cut is very useful to suppress $t\bar{t}$ contributions without harming the signal efficiency. The reconstruction of $M_{\ell\nu b}$ is tuned for single top events. For $t\bar{t}$ a large fraction of events is found at high values for the reconstructed mass $M_{\ell\nu b}$ in comparison to the signal.
Unfortunately the Monte Carlo statistic after b-tagging is very low. Therefore, all available signal and background events have been used in the "training" state, that corresponds to calculate the transformation coefficients of the algorithm. By this procedure the efficiencies used to calculate the number of expected events are slightly biased. A systematic uncertainty will be introduced to account for this. If one uses to few Monte Carlo events to calculate the transformation, the algorithm starts to learn individual events. To avoid this overtraining effect the small bias in the efficiency calculation was preferred. Due to the small available Monte Carlo statistics the two required signal efficiencies for the two steps are different. In the first step a signal efficiency of 90% is chosen, whereas for the second step a signal of 70% is used. So the remaining Monte Carlo statistic after the first iteration is sufficient to obtain a stable result. The 70% signal efficiency for the second step has been chosen by requiring about two expected remaining t-channel events in the data sample. Cutting harder would still improve the significance ρ, but the signal yield is reduced. The probability to find no signal events in the data set is $P(0) = e^{-\mu_{\text{signal}}}$ and by reducing the signal yield μ_{signal} this probability is increased. Figure 8.6 shows the significance ρ as a function of the signal efficiency in the second step of the algorithm. Figure 8.5 shows the distributions of the logarithm of the Δ parameters obtained by the K_{T} algorithm. Table 8.2 list the Monte Carlo events after the loose $M_{\ell\nu b}$ requirement, after the first IDA iteration and the total remaining events. The events after the first iteration are the input test events for the second step. Figure 8.7 depicts the obtained distributions for the signal and background classes in both iterations. The histograms are normalized to the number of events to be expected from each source. For the t-channel process the Standard Model cross section has been scaled by a factor 5. The dashed line indicates the cut applied in each step. The separation power of the discriminant has decreased in the second step, because the events that could be clearly classified as background have been removed already in the previous step, despite that the two step method is superior to a one step approach where one cuts harder on the discriminant distribution. Such a one step scenario was studied and found to give a lower significance than the two step algorithm for the identical signal efficiency. The

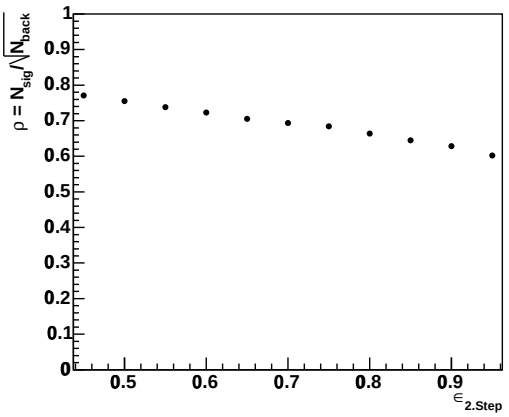

Figure 8.6: The significance ρ as a function of the signal efficiency in the second step of the algorithm.

Sample	N_{input}	$N_{1.\text{Step}}$	$N_{2.\text{Step}}$
t-channel	7193	6473	4532
$Wb\bar{b}$	3097	1200	407
$Wc\bar{c}$	883	304	82
$W + 2$jets	9706	3336	965

Table 8.2: Number of training events for the IDA algorithm. The last column list the remaining Monte Carlo events after the second iteration.

background suppression of this 2 step algorithm was not achieved. For the scenario considered here the significance ρ decreased by 5%.

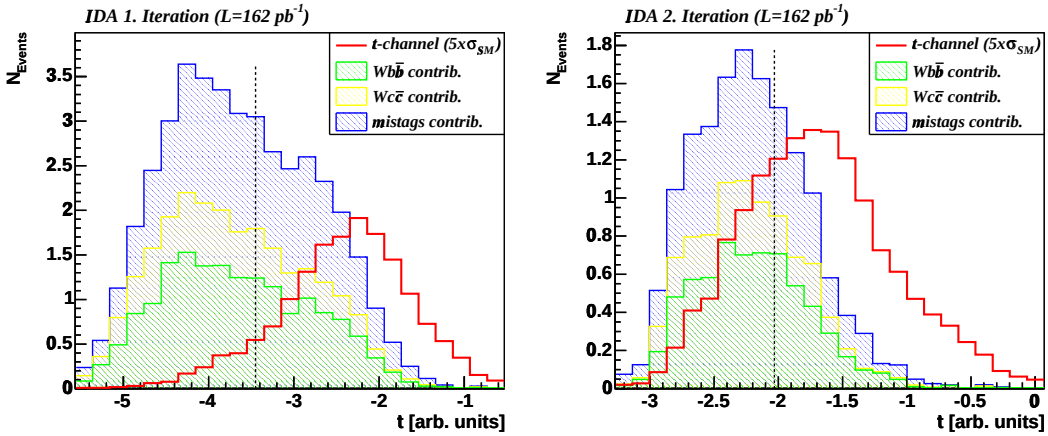

Figure 8.7: The discriminant distributions as obtained in the 2 iterations of the IDA algorithm. The stacked histogram shows the background contributions.

No.	Sample	N_{events}^{1-tag}	$\epsilon(M_{lvb})$	ϵ(IDA 1.Step)	ϵ(IDA 2.Step)	$N_{events}^{\mathrm{IDA}}$
1	t-channel	3.35	0.971	0.874	0.612	2.05
2	s-channel	1.81	0.857	0.641	0.311	0.56
3	WBB	19.18	0.871	0.338	0.115	2.20
4	WCC	8.22	0.889	0.306	0.083	0.68
5	WC1p	8.39	0.916	0.378	0.112	0.94
6	mistags	18.45	0.928	0.319	0.092	1.70
7	$t\bar{t}$	6.90	0.628	0.515	0.221	1.52
8	QCD	9.74	0.960	0.361	0.102	1.00
9	di-boson	2.18	0.882	0.358	0.069	0.15

Table 8.3: The IDA efficiencies for the Monte Carlo samples used to determine the number of expected events using a luminosity of 162 pb^{-1}. N_{events}^{1-tag} denotes the number of events expected after requiring exactly 1-b-tag. $\epsilon(M_{lvb})$ denotes the efficiency of the M_{lvb}-cut with respect to N_{events}^{1-tag}, ϵ(IDA 1.Step) lists the efficiency after the first IDA-iteration and the M_{lvb}-cut. ϵ(IDA 2.Step) summarizes the efficiency after the second iteration. The efficiencies listed are inclusively given, all of them are calculated with respect to N_{events}^{1-tag}. $N_{events}^{\mathrm{IDA}}$ shows the final number of expected events after the second iteration.

8.2 Efficiencies and Uncertainties

To estimate the efficiencies and the number of expected signal and background events the coefficients obtained by the training stage have been used to calculate the efficiencies. Table 8.3 list the measured efficiency for the various Monte Carlo samples used to determine the number of expected events for signal and backgrounds. Since some samples have already been used in this training, there is a 5% bias in the efficiencies for all samples. This uncertainty was estimated by splitting the sample in 2 independent subsample. One was used for the training , whereas the other was used to measure the efficiency. Due to the lack of statistics in the Z boson samples the $WW0p$ sample was used to model the diboson efficiency.

Table 8.2 list the jet energy scale uncertainties for the samples. To evaluate these uncertainties the method described in the previous chapter was used. Therefore a function was used to varies the jet energy $\pm 1\sigma$. The errors for the non-top contributions have been symmetrized. Unfortunately, these errors have been determined using the maximum deviation from the mean values as the estimator for the $\pm 1\sigma$ level [90]. When using a multivariate technique such as IDA, this method of estimation the error results in very large uncertainties of about 25% for the backgrounds. The last line gives the total error assigned

No.	Sample	Uncertainty [%]
1	t-channel	$^{+9.5}_{-8.6}$
2	s-channel	$^{+14.1}_{-8.8}$
3	$Wb\bar{b}$	± 18.8
4	$Wc\bar{c}$	± 22.7
5	$Wc1p$	± 20.4
6	mistags	± 26.7
7	$t\bar{t}$	$^{-5.8}_{+11.9}$
8	QCD	± 30.5
9	diboson	± 33.7
	non-top	± 23.5

Table 8.4: The jet energy scale IDA acceptance uncertainties for the various samples. The upper values correspond to a $+1\sigma$ deviation and the lower values to a -1σ deviation of the JES.

to the non-top expectation. Here the error contributions have been weighted by the number of expected events. Table 8.5 lists the considered sources and assigned uncertainties considered for the single top quark production processes. The procedure to calculate these errors is identical to the separate search. The errors assigned to $t\bar{t}$ modeling (choice of the Monte Carlo generator) are 2.3% and due to the top quark mass uncertainty 5% for the acceptance.

To calculate the number of expected non-top events scale factors have been introduced. The errors due to these scale factors are assumed to be dominated by the jet energy scale uncertainty. To account for those errors, the relative errors

No.	Source	t-channel	s-channel
1	Jet energy scale	$^{9.5}_{-8.6}$%	$^{+14.1}_{-8.8}$%
2	ISR	±5.0%	±0.6%
3	FSR	±2.0%	±8.5%
4	PDF	±3.9%	±1.0%
5	Generator	±4.5%	±3.5%
6	Top quark mass	$^{+0.8}_{-4.5}$%	-6.2%
7	ϵ_{trig}, ϵ_{ID}, luminosity	±9.8%	±9.8%

Table 8.5: Systematic acceptance uncertainties for t- and s-channel single-top signal after second IDA iteration.

No.	Sample	rel error [%]	N_{events}
3	$Wb\bar{b}$	$\pm$ 34.5	2.20 $\pm$ 0.76
4	$Wc\bar{c}$	$\pm$ 35.6	0.68 $\pm$ 0.24
5	$Wc1p$	$\pm$ 33.0	0.94 $\pm$ 0.31
6	mistags	$\pm$ 30.2	1.70 $\pm$ 0.51
8	QCD	$\pm$ 34.8	1.00 $\pm$ 0.35
9	diboson	$\pm$ 35.8	0.15 $\pm$ 0.06
	Total non-top	$\pm$ 21.7	6.66 $\pm$ 1.45

Table 8.6: Summary of the non-top contributions

obtained by the method 2 calculation and the jet energy uncertainty are added for each sample in quadrature to estimate the acceptance uncertainty. This has been done, since several kinematic variables used for the IDA are sensitive to jet energy scale uncertainty and thus the dominant error is assumed to originate from this effect. Table 8.6 summarizes the number of expected events for the non-top contributions.

Process	$N_{\text{events}}^{\text{IDA}}$	$N_{\text{events}}^{2-\text{tag}}$
t-channel	2.05±0.35	0.02±0.01
s-channel	0.56±0.10	0.32±0.05
$t\bar{t}$	1.52±0.35	0.60±0.14
non-top	6.66±1.48	2.59±0.72
Total background	8.18±1.52	3.19±0.72
Total expected	10.79±1.56	3.53±0.72
Observed	12	6

Table 8.7: Summary of the number of expected events using IDA.

8.3 Comparison of Data and Expectation

Table 8.7 list the number of expected events after application of the iterative discriminant analysis. The number of expected events and the observed events are within the 1σ error level for the 1-tag subsample. Here the 5% error due to the efficiency measurement is added in quadrature to the obtained uncertainties. The expected significance of this analysis for the t-channel only in the 1-tag subsample is 0.69. This corresponds to an improvement of about 34% with respect to the cut-based search if only the 1-tag subsample is considered.

Figure 8.8 shows the comparison of the expected discriminant distributions to the data for the 2 steps. The 12 remaining events are to be found on the right-hand side of the discriminant distribution of the second step. These events exceed a value $t = 2.03$. Figure 8.9 shows the $M_{\ell\nu b}$ and $Q \cdot \eta$ distributions after the application of IDA in the 1-tag subsample. By the use of this algorithm the distributions for signal and background are adjusted. The $M_{\ell\nu b}$ distribution for the non-top backgrounds peaks after IDA around 170 GeV/c^2. Also the $Q \cdot \eta$ distributions have a similar shape. This is expected, since the goal of this algorithm is to select regions in phase space, where the signal probability is high. Figure 8.10 depicts the transverse momentum spectrum of the second leading jet and the invariant mass distribution of the 2 jets for data and expectation. These observables are not explicitly used by the algorithm, but correlated to some input variables. For instance is the p_{T} of the second leading jet a contributor to H_{T} and $Q \cdot \eta$ is correlated to the dijet mass M_{jj}. Figure 8.11 shows the logarithm of Δ parameters obtained by the K_{T} jet clustering algorithm. All data distributions are in good agreement with the expectation.

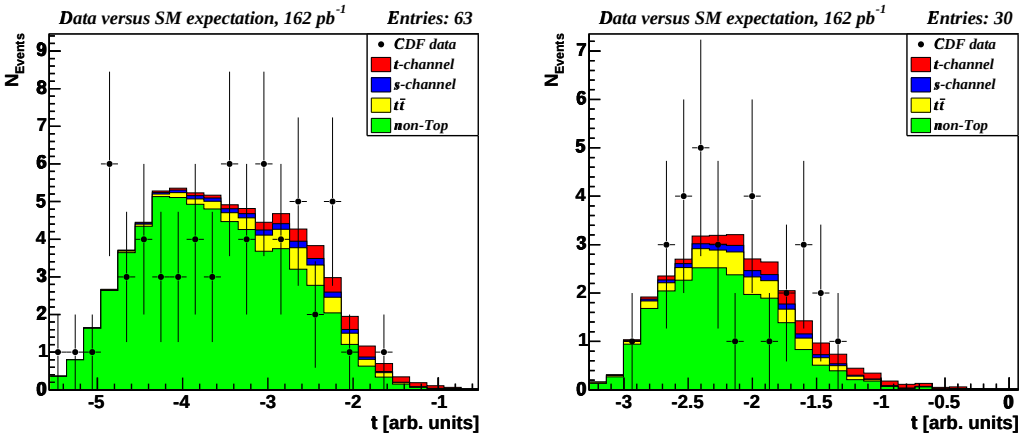

Figure 8.8: The IDA discriminant t distribution after requiring exactly 1-b-tag (left) and the discriminant distribution after the first IDA iteration (right).

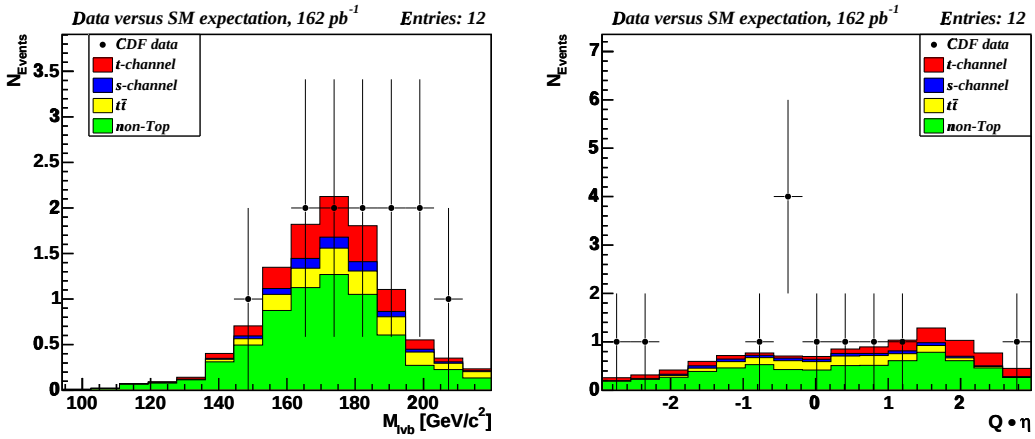

Figure 8.9: Comparison of the $M_{\ell\nu b}$ and $Q \cdot \eta$ distributions of the data and the expectation.

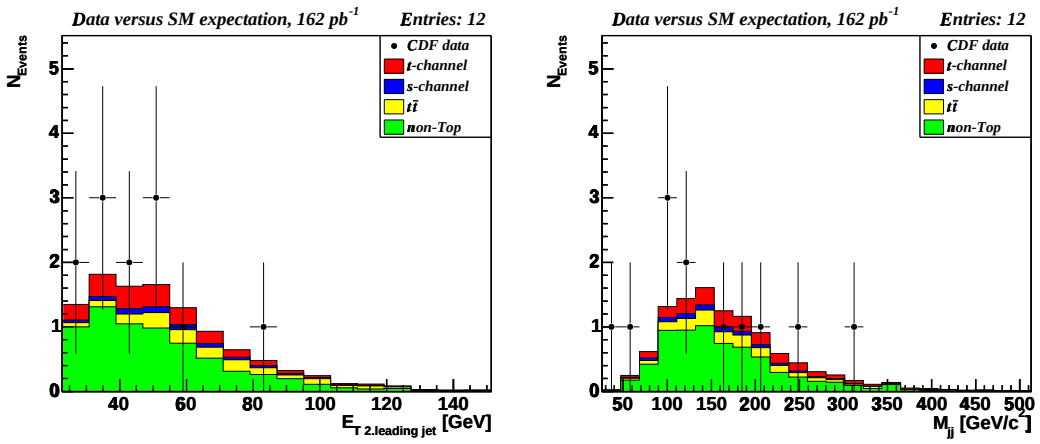

Figure 8.10: Comparison of the p_{T} spectrum of the second leading jet and the in variant dijet mass M_{jj} distribution of the data and the expectation.

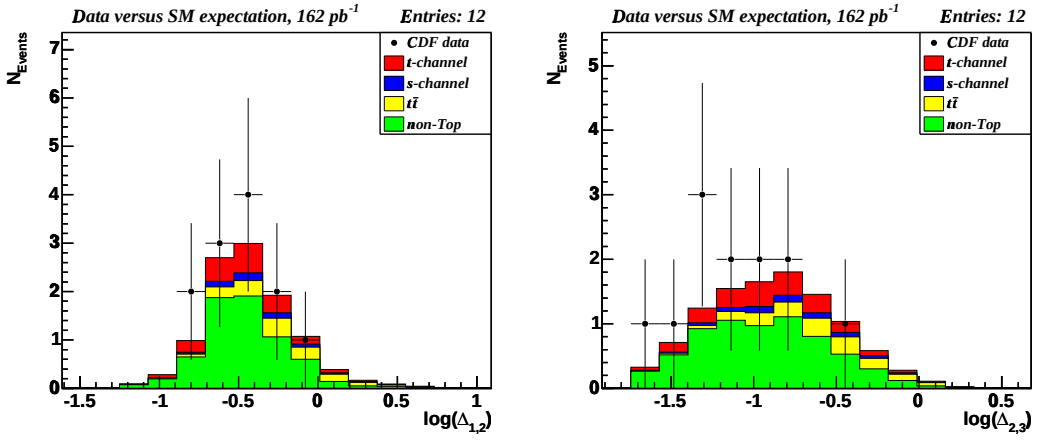

Figure 8.11: Comparison of the Δ distribution of the data and the expectation.

8.4 Results

Table 8.7 lists the number of expected events after application of the iterative discriminant analysis. The number of expected events and the observed events agree within the 1σ error level. Here the 5% error due to the efficiency measurement is added in quadrature to the obtained uncertainties.
Since the significance of the analysis is not high enough (0.69 for the t-channel), upper limits on single top production are calculated. To increase the sensitivity on the s-channel production, the 2-tag subsample is included in the calculation. The likelihood technique that was used in the cutbased search is used to derive the upper limits. Therefore a maximum likelihood function is used which contains two terms, one for the 1-tag subsample and one for the 2-tag sample. Again, the total number of events was used for the 2-tag likelihood function, whereas for the 1-tag subsample the discriminant distribution is used. Therefore 8 bins have been calculated based on the Monte Carlo data. Figure 8.12 shows the probability density function used. Due to the small number of background Monte Carlo events exceeding a value of -1.0 for the discriminant, the outer bin includes the overflow. The bin edge has been calculated by requiring 1000 t-channel Monte Carlo events to exceed this value. The lower edge of the histogram is given by the IDA cut of 2.03 in the second iteration.

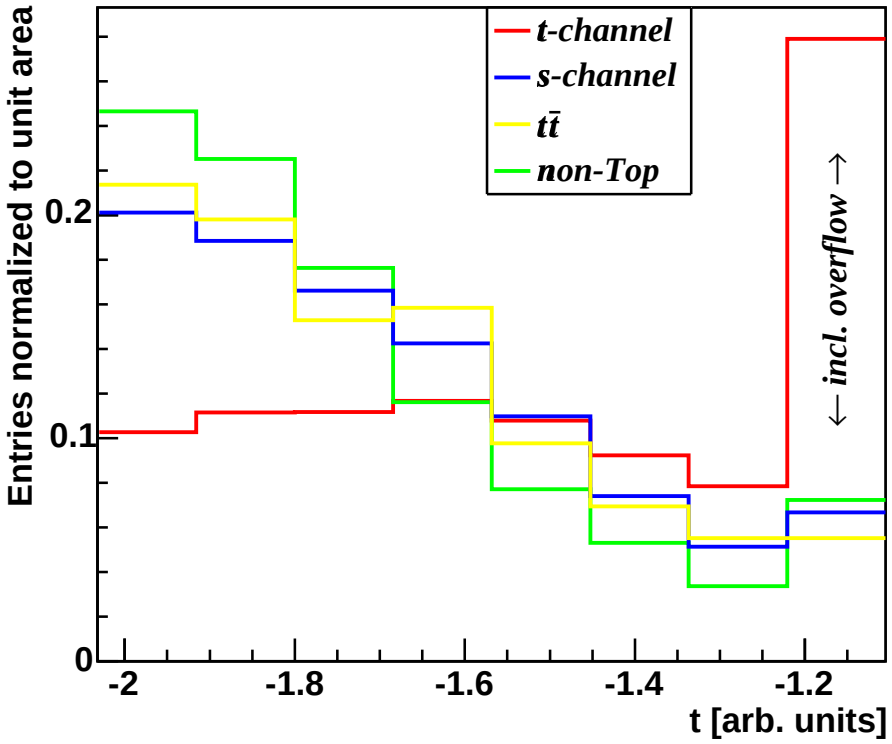

Figure 8.12: The probability density functions for the IDA search in the 1-tag subsample, the outer bin includes the overflow.

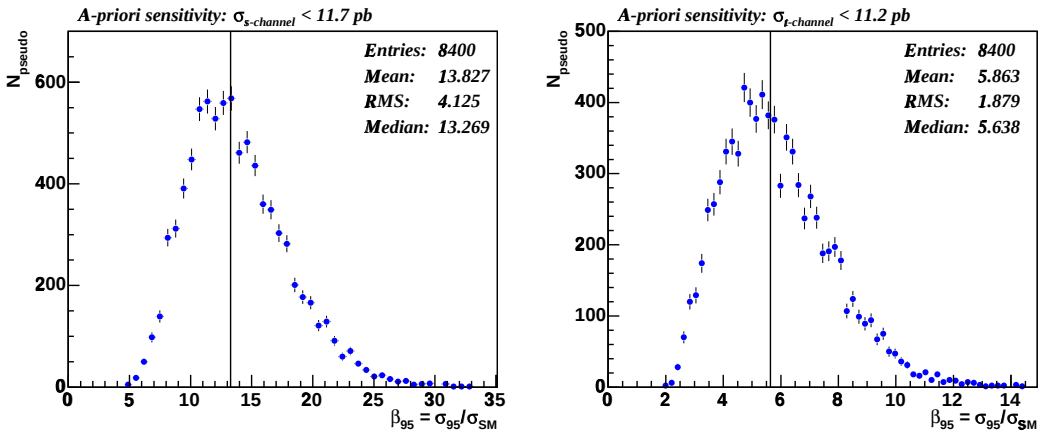

Figure 8.13: The pseudo experiment upper limits used to calculate the a-priori sensitivity.

8.4.1 A-priori sensitivity

To estimate the sensitivity the pseudo experiment technique described in the previous chapter was used. The upper limit to be expected for the t-channel is 11.2 pb when the s-channel is constrained within the given uncertainties to the expectation. For the s-channel the sensitivity is 11.7 pb. Figure 8.13 depicts the distributions of the upper limits for the s- and t-channel search in units of the Standard Model expectation obtained by 8400 pseudo experiments. The median upper limit corresponds to the expected sensitivity. If one uses a likelihood function the is only based on the total number of observed events in both subsamples the obtained sensitivities are 11.0 pb for the t-channel and 12.0 pb for the s-channel. This method corresponds to a counting experiment. These expected sensitivities are essentially identical to the ones obtained by the cut-based search, in spite of an increased significance $\rho = N_{\mathrm{sig}}/\sqrt{N_{\mathrm{back}}}$. This can be explained by the increase of the relative systematic and statistical uncertainties for signal and backgrounds. The use of a multivariate technique such as IDA is a useful tool to reduce the amount if luminosity needed to discover or rule out single top production, since the figure of merit for a discovery is the significance. These findings are in full agreement with [91]. Here a multivariate likelihood search is performed, that increases the significance, whereas the a-priori sensitivity remains essentially unchanged.

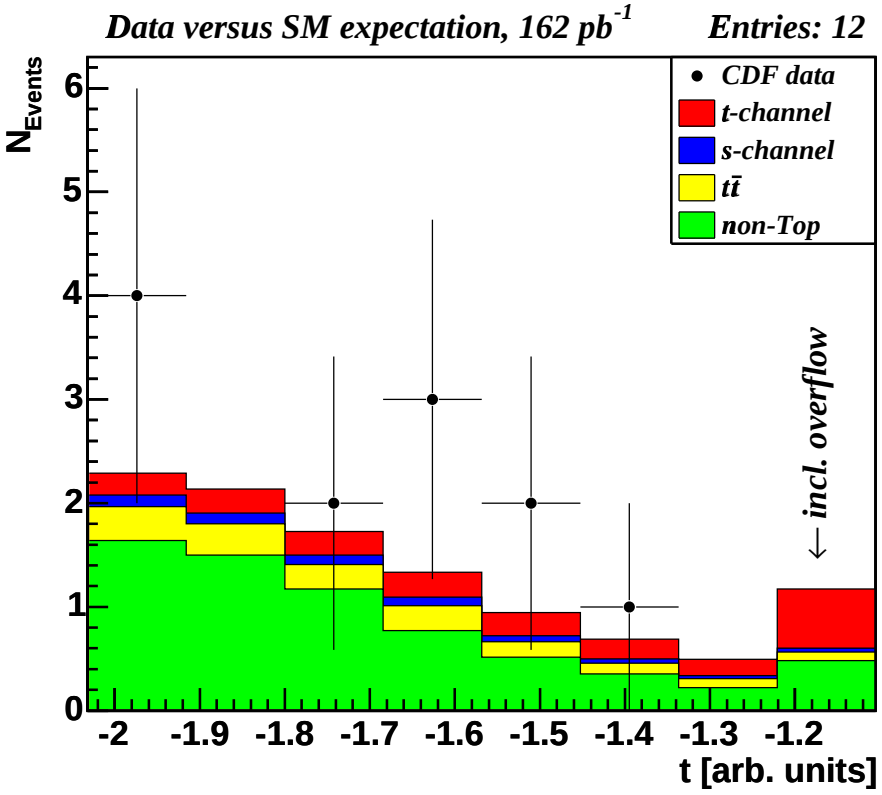

Figure 8.14: The resulting discriminant t distribution after both IDA iterations

8.4.2 A-posteriori limits

The discriminant distribution of the 12 CDF data events is shown in figure 8.14. There are no events to be found in the outer bins, where the signal probability is large.

The CDF data derived upper limit on s-channel single top production obtained by this method is 17.2 pb at 95% C.L.. The corresponding t-channel limit is 11.0 pb at 95% C.L.. These limits are obtained by integration of the posterior probability densities up to the cross section value where 95% probability are covered. In this analysis the s-channel is constrained within the errors to the expectation when the t-channel limit is calculated and vice versa. Figures 8.15 shows the a-posteriori probability densities for the s- and t-channel search. The colored area corresponds to the 95% C.L. The obtained β^{95} values, i.e the upper limit in units of the Standard Model prediction, are 19.57 for the s-channel and 5.57 for the t-channel. The probability density for the t-channel

peaks at $\beta^{\mathrm{MPV}}_{\mathrm{t-ch}} = 0.0$. This result was also found in the cutbased search. For the s-channel the posteriori probability density achieves its maximum at $\beta^{\mathrm{MPV}}_{\mathrm{s-ch}} = 6.8$ which is slightly higher in comparison to the cutbased search ($\beta^{\mathrm{MPV}}_{\mathrm{s-ch}} = 4.6$). But if this value is compared to the the range of expected limits, i.e. the width of the distribution shown in figure 8.13, such a result is not unexpected assuming Standard Model production.

The found limit for the t-channel is slightly lower than the expected median limit, since the most probable value of likelihood is at $\beta = 0.0$. The s-channel limit is higher than the expected median limit derived by pseudo experiments assuming SM production. This can be explained by the surplus of events in the 1-tag and especially in the 2-tag sample. Within the highest probability density intervals the result for the s-channel agrees with the cutbased search. If a likelihood function based on the total number of expected events in the 1-tag and 2-tag subsamples is used, the obtained limit for the s-channel is 16.8 pb and 11.5 pb for the t-channel.

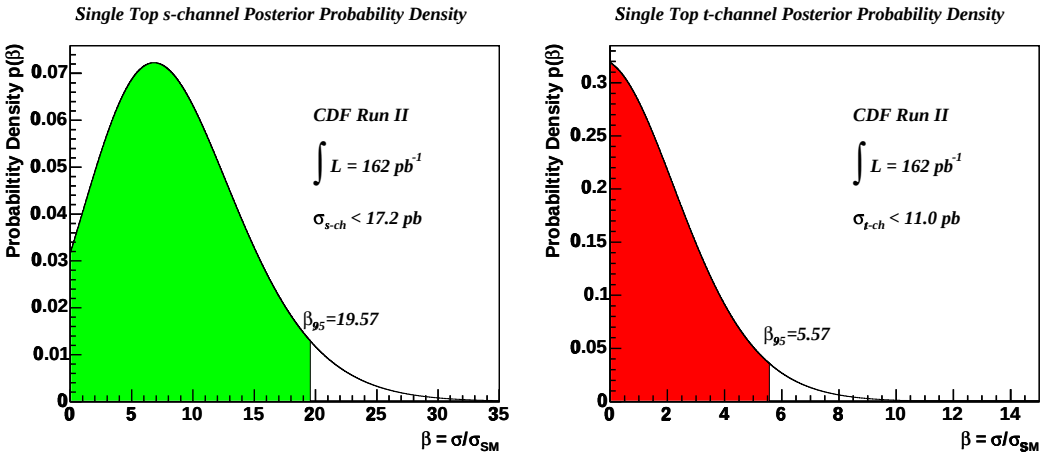

Figure 8.15: The s- and t-channel a-posteriori probability densities used to calculate the limits on s- and t-channel single top production

Table 8.8 summarizes the most probable values and the expected and observed limits.

Process	MPV ± HPD $[pb]$	expected limit $[pb]$	observed limit $[pb]$
t-channel	$0.0^{+5.3}_{-0.0}$	11.2	11.0
s-channel	$6.0^{+4.7}_{-5.0}$	11.7	17.2

Table 8.8: Summary of the upper limits at the 95% C.L. and the most probable values of the single top cross sections.

Integrated Luminosity	expected $\rho_{\mathrm{t-ch}}$ cutbased	expected $\rho_{\mathrm{t-ch}}$ IDA
162 pb^{-1}	0.51	0.69
500 pb^{-1}	0.90	1.21
1000 pb^{-1}	1.26	1.71
2000 pb^{-1}	1.79	2.42
3100 pb^{-1}	2.23	3.02
4400 pb^{-1} (base goal)	2.66	3.60
8500 pb^{-1} (design goal)	3.69	5.00

Table 8.9: Expected significance ρ for the 1-tag subsamples assuming a t-channel cross section of 1.98 pb. Here s-channel contributions are treated as backgrounds. Base goal denotes a conservative estimate for the delivered luminosity until 2009, while design goal denotes an optimistic estimate for the total delivered luminosity in Run II.

8.5 Perspectives for RunII

So far no significant evidence for electroweak single top quark production has been observed, therefore limits on this process have been calculated. The iterated discriminant analysis does not improve the limits on s- and t-channel single top quark production, but such a technique drastically decreases the amount of luminosity needed to discover this production mode. Table 8.9 list the expected significances in the 1-tag subsamples for different luminosities for a t-channel search. In such a scenario the s-channel contributions are treated as background. Here SM production for s- and t-channel have been assumed. A 3σ evidence is feasible when the integrated luminosity exceeds 3100 pb^{-1} by the use of IDA, while the cutbased scenario achieves a 2.2σ evidence. If the Tevatron will deliver an integrated luminosity of 8.5 fb^{-1}, which is the challenging design goal for Run II a 5σ discovery can be achieved.

If the s- and the t-channel production modes are combined to an inclusive single top signal, a 3σ evidence is feasible with 1.8 fb^{-1} (see table 8.10). Approximately 5 fb^{-1} integrated luminosity is necessary to achieve a 5σ discovery. The discovery of single top quark production is well in the reach of CDF in Run II.

Integrated Luminosity	expected ρ_{comb} cutbased	expected ρ_{comb} IDA
162 pb^{-1}	0.74	0.91
500 pb^{-1}	1.30	1.60
1000 pb^{-1}	1.84	2.26
1800 pb^{-1}	2.47	3.03
2000 pb^{-1}	2.60	3.19
3100 pb^{-1}	3.18	3.98
4400 pb^{-1} (base goal)	3.86	4.74
8500 pb^{-1} (design goal)	5.36	6.60

Table 8.10: Expected significance ρ for the 1-tag subsamples assuming a t-channel cross section of 1.98 pb and a s-channel production cross section of 0.88 pb. Here s-channel and t-channel contributions are combined. Base goal denotes a conservative estimate for the delivered luminosity until 2009, while design goal denotes an optimistic estimate for the total delivered luminosity in Run II.

Chapter 9

Summary and Outlook

In this thesis two searches for electroweak single top quark production with the CDF experiment have been presented, a cutbased search and an iterated discriminant analysis. Both searches find no significant evidence for electroweak single top production using a data set corresponding to an integrated luminosity of 162 pb^{-1} collected with CDF. Therefore limits on s- and t-channel single top production are determined using a likelihood technique. For the cutbased search a likelihood function based on lepton charge times pseudorapidity of the non-bottom jet was used if exactly one bottom jet was identified in the event. In case of two identified bottom jets a likelihood function based on the total number of observed events was used. The systematic uncertainties have been treated in a Bayesian approach, all sources of systematic uncertainties have been integrated out. An improved signal modeling using the MadEvent Monte Carlo program matched to NLO calculations has been used. The obtained limits for the s- and t-channel single top production cross sections are 13.6 pb and 10.1 pb, respectively. To date, these are most stringent limits published for the s- and the t-channel single top quark production modes.

In order to discover electroweak single top production it is important to isolate the signal. A multivariate technique, here an iterated discriminant analysis, was used to suppress backgrounds. This technique was applied to the subsample with exactly one identified bottom jet. The significance $\rho = N_{\text{sig}}/\sqrt{N_{\text{back}}}$ achieved by this method exceeded the significance of the cutbased search by 34% for the t-channel process. A likelihood function based on the discriminant distribution in the one bottom jet subsample and the number of total events in the two bottom tag subsample was used to calculate the upper production cross section limits for single top quark production. For the s-channel the measured limit is 17.2 pb and 11.0 pb for the t-channel production mode.

Although the limits have not been improved by the use of the iterated discriminant analysis, the amount of luminosity needed to discover single top quark production was drastically reduced. In Run II a 3σ evidence is feasible with an data set corresponding to an integrated luminosity of about 1.8 fb^{-1} if the s-

and t-channel production modes are combined. For the t-channel only, a 3σ evidence is feasible with 3.1 fb^{-1}. In contrast, for the cutbased search an integrated luminosity of about 3.0 fb^{-1} is necessary to achieve a 3σ evidence for the combined s- and t-channel signals.

Single top quark production is a challenging topic at the Tevatron. By the use of such multivariate techniques a 5σ discovery is feasible in Run II.

Appendix A

Electron and Muon Data Sets

Table A.1 lists the integrated luminosities for all processed file sets of the electron trigger samples and table A.2 for the muon triggers samples. The analyzed data corresponds to an integrated luminosity of (162 ± 10) pb^{-1} with an error on the luminosity of 6% [65] for the CEM electrons and CMUP muons. The CMX muon luminosity is 150 pb^{-1}. All good runs up to September 07, 2003 have been used. The first column in the tables lists file set identifier, the second and third column list the minimum and maximum run number to be found in these file sets and the last column list the integrated luminosity of the accepted ("good") runs for this analysis. Due to an noncommissioned CMX in the early stage of Run II the collected CMX data set is smaller than the CEM and the CMUP data sets.

Fileset	min. run no.	max. run no.	$\mathcal{L}$ of good runs $[pb^{-1}]$
GI0741.0	144573	145004	1.44906
GI0741.1	145004	145420	1.17576
GI0741.2	145420	147834	1.10679
GI0741.3	147834	148676	1.71413
GI0741.4	148676	148908	1.73136
GI0741.5	148908	149387	1.96833
GI0744.0	149387	150070	1.06238
GI0744.1	150070	150418	0
GI0744.2	150418	150805	0.557914
GI0744.3	150805	151092	0.613133
Continued on next page			

Table A.1: Luminosity of the used electron filesets

Fileset	min. run no.	max. run no.	$\mathcal{L}$ of good runs $[pb^{-1}]$
GI0744.4	151092	151483	1.33744
GI0744.5	151483	151557	0.668394
GI0747.0	138425	139787	0
GI0747.1	139787	140895	0
GI0747.2	140895	141660	0.724025
GI0747.3	141660	142689	0.813429
GI0747.4	142689	144002	0
GI0747.5	144002	144573	0
GI0749.0	151557	151843	1.39589
GI0749.1	151843	151917	1.85493
GI0749.2	151917	152270	1.34034
GI0749.3	152270	152558	1.82182
GI0749.4	152558	152617	0.894577
GI0749.5	152617	152675	0.221605
GI0750.0	152675	152810	0.84432
GI0750.1	152810	153054	0.416582
GI0750.2	153054	153075	0.390905
GI0776.0	153075	153345	0.913788
GI0776.1	153345	153411	0.812132
GI0776.2	153411	153447	0.736573
GI0776.3	153447	153694	1.03338
GI0776.4	153694	153986	0.668107
GI0943.0	153986	154111	1.02303
GI0943.1	154069	154176	0.913009
GI0943.2	154176	154452	1.38299
GI0945.0	154452	154594	0.792683
GI0945.1	154594	154654	0.207601
GI0945.2	154654	154799	0.101821
GI0949.0	154799	155114	0.695422
GI0949.1	155114	155130	1.20531
Continued on next page			

Table A.1: Luminosity of the used electron filesets

Fileset	min. run no.	max. run no.	$\mathcal{L}$ of good runs $[pb^{-1}]$
GI1239.0	155130	155318	1.63315
GI1239.1	155318	155364	1.24407
GI1239.2	155364	155768	2.04529
GI1239.3	155768	155818	2.14356
GI1239.4	155818	155918	1.95453
GI1241.0	155918	156007	2.11422
GI1241.1	156007	156100	1.91996
GI1241.2	156100	156369	2.154
GI1275.0	156369	156484	1.34265
GI1275.1	156484	156487	0.656594
GI1319.0	160823	160896	1.60258
GI1319.1	160896	161029	2.5104
GI1319.2	161029	161330	1.73234
GI1319.3	161330	161330	0.205538
GI1322.0	161330	161411	2.13219
GI1322.1	161411	161633	1.87407
GI1322.2	161633	161718	2.52958
GI1322.3	161718	161820	2.38318
GI1322.4	161820	162178	1.8268
GI1431.0	162178	162393	2.13297
GI1431.1	162393	162423	1.12124
GI1431.2	162423	162479	1.92307
GI1434.0	162479	162480	0.670685
GI1603.0	158733	159175	0
GI1603.1	159175	159260	0
GI1603.2	159260	160152	0.722469
GI1603.3	160152	160301	1.70148
GI1603.4	160301	160404	0.772884
GI1613.0	160404	160441	1.8898
GI1613.1	160441	160596	1.9362
Continued on next page			

Table A.1: Luminosity of the used electron filesets

Fileset	min. run no.	max. run no.	$\mathcal{L}$ of good runs $[pb^{-1}]$
GI1613.2	160598	160823	1.59043
GI1624.0	158644	158732	0
GI1698.0	162480	162519	2.2496
GI1698.1	162519	162664	2.35107
GI1698.2	162664	162820	2.04301
GI1698.3	162820	162838	1.86829
GI1698.4	162838	162937	2.25581
GI1698.5	162937	162989	1.27544
GI1699.0	162989	163064	2.11833
GI1699.1	163064	163113	1.06407
GI1792.0	163113	163462	1.97885
GI2197.0	152598	152636	0.580447
GI2197.1	152636	152746	0.539114
GI2197.2	152746	152967	0.81728
GI2197.3	152967	153074	0.251963
GI2197.4	153074	153327	0.882434
GI2197.5	153327	153389	1.15194
GI2198.0	153389	153447	1.10236
GI2198.1	153447	153693	0.822007
GI2198.2	153693	153987	0.76
GI1792.1	163462	164109	1.35884
GI1792.2	164109	164310	1.71245
GI1792.3	164310	164451	1.34853
GI1792.4	164451	164729	1.57529
GI2382.0	164733	165201	0.437316
GI2382.1	164819	164989	1.28995
GI2382.2	164989	165087	1.51513
GI2382.3	165087	165198	1.85668
GI2382.4	165198	165271	1.30489
GI2382.5	165271	165364	2.30421
Continued on next page			

Table A.1: Luminosity of the used electron filesets

Fileset	min. run no.	max. run no.	$\mathcal{L}$ of good runs $[pb^{-1}]$
GI2383.0	165364	165412	1.77084
GI2383.1	165412	165465	1.54805
GI2383.2	165465	165873	2.04912
GI2383.3	165873	165906	1.40124
GI2383.4	165906	166008	2.31089
GI2383.5	166008	166008	0.335618
GI2429.0	166008	166063	2.09866
GI2429.1	166063	166328	1.42859
GI2429.2	166328	166406	1.73542
GI2429.3	166406	166529	2.5552
GI2429.4	166529	166567	1.26918
GI2429.5	166567	166615	2.1404
GI2430.0	166615	166661	2.3211
GI2430.1	166661	166715	1.87801
GI2430.2	166715	166783	1.81939
GI2686.0	166783	167022	1.79865
GI2686.1	167022	167053	1.81102
GI2686.2	167053	167186	1.89998
GI2686.3	167186	167551	3.2039
GI2686.4	167325	167506	0.717043
GI2686.5	167506	167623	1.46903
GI2687.0	167551	167631	1.37395
GI2687.1	167631	167849	0.764767
GI2687.2	167849	167955	0
GI2687.3	167955	168087	0
GI2687.4	168087	168601	0
GI2687.5	168601	168889	0
GI2715.0	168889	168889	0
Continued on next page			

Table A.1: Luminosity of the used electron filesets

Fileset	min. run no.	max. run no.	$\mathcal{L}$ of good runs $[pb^{-1}]$
Sum			161.57

Table A.1: Luminosity of the used electron filesets. The first column lists the fileset name. The second column list the minimum and the third one the maximum run number. The fourth is the luminosity of the good runs in the file set.

Fileset	min. run no.	max. run no.	$\mathcal{L}$ of good runs $[pb^{-1}]$
GI0728.0	141544	141576	0.155948
GI0728.1	141576	144420	1.38151
GI0728.2	144420	147730	3.08553
GI0728.3	147730	149355	5.5602
GI0728.4	149355	150444	1.56207
GI0728.5	150444	151557	3.17689
GI0730.0	151557	152169	4.28252
GI0730.1	152169	152675	3.24664
GI0730.2	152675	152967	1.24965
GI0777.0	152970	153447	3.2133
GI0777.1	153447	153986	1.69179
GI0927.0	153986	154594	4.11171
GI0927.1	154594	154799	0.309421
GI1201.0	154799	155389	5.40603
GI1201.1	155389	156081	8.11329
GI1201.2	156081	156369	3.59018
GI1276.0	156369	156487	1.99925
GI1606.0	158733	160230	1.89886
GI1614.0	160230	160761	5.77
GI1626.0	158644	158732	0
GI1704.0	162454	162820	7.92988
GI1704.1	162820	163064	7.51786
GI1704.2	163064	163527	4.18187
GI2006.0	160761	161330	6.89249
GI2006.1	161330	161789	8.25634
GI2006.2	161789	162454	6.86885
GI2006.3	162454	162454	0.285157
GI2234.0	152598	153054	1.94809
GI2234.1	153054	153618	3.3124
GI2234.2	153618	153987	1.3081
Continued on next page			

Table A.2: Luminosity of the used muon filesets

Fileset	min. run no.	max. run no.	$\mathcal{L}$ of good runs $[pb^{-1}]$
GI2234.2	163956	164451	3.28087
GI2234.3	164451	164729	1.57529
GI2491.0	164733	165198	4.79452
GI2491.1	165198	165465	7.23254
GI2491.2	165465	166038	7.21985
GI2491.3	166038	166567	7.96407
GI2491.4	166567	166805	8.5692
GI2491.5	166805	167053	3.19938
GI2685.0	167053	167551	6.59462
GI2685.1	167551	168000	2.83405
GI2685.2	168000	168889	0
Sum			161.57

Table A.2: Luminosity of the used muon filesets. The first column lists the fileset name. The second column list the minimum and the third one the maximum run number. The fourth is the luminosity of the good runs in the file set.

Appendix B

Determination of $\epsilon_{\text{evt}}^{\text{MC}}$

The determination of the event detection efficiency is based on Monte Carlo events for the single top signals, the $t\bar{t}$ and the diboson backgrounds . All selection and identification criteria are applied to the simulated data. The number of remaining events in the 2-jet bin after application of the following requirements is calculated to derive $\epsilon_{\text{evt}}^{\text{MC}}$:

- After requiring at least one b-tagged jet in the event (N_{btag})
- After requiring exactly one b-tagged jet in the event ($N_{btag=1}$)
- After the $M_{\ell\nu b}$ cut if at least one b-tag is assigned to the event
- After the additional cut on the leading jet in E_T (N_{jet1}) and the $M_{\ell\nu b}$ cut,
- After $M_{\ell\nu b}$ cut in the 1-b-tag bin (N_{1tag})
- After the $M_{\ell\nu b}$ and E_T(jet1) cut in the 1-b-tag bin ($N_{1tag,ET}$)
- After $M_{\ell\nu b}$ cut in the 2-b-tag bin (N_{2tag}).

All these scenarios are given since based on these numbers the analysis was optimized. Using the obtained numbers for each scenario the Monte Carlo derived event detection efficiency $\epsilon_{\text{evt}}^{\text{MC}}$ is calculated.

B.1 Determination of $\epsilon_{\text{evt}}^{\text{MC}}$ for Single Top Events

Table B.1 summarizes the number of remaining single top events for each considered scenario. Table B.2 list the results of the $\epsilon_{\text{evt}}^{\text{MC}}$ calculation for single top events.

	MadEvent		TopRex		Pythia	
Process	t-chan.	s-chan.	t-chan.	s-chan.	t-chan.	s-chan.
ID	mtop0s/1s	mtop2s	rtop0s/1s	rtop2s	ttop1s	ttop0s
N_{tot}	163237	199953	138107	200107	499189	440000
N_{obsv}	157832	192931	133623	193052	482770	425541
CEM Electrons						
N_{btag}	4251	7706	3225	7354	3914	4622
$N_{\mathsf{btag=1}}$	4198	5807	3183	5586	3894	3520
$N_{\mathsf{M}\ell\nu\mathsf{b}}$	3563	5068	2644	4896	3300	3067
N_{jet1}	3442	4904	2553	4749	3212	2974
N_{1tag}	3526	3686	2622	3626	3288	2280
$N_{\mathsf{1tag,ET}}$	3407	3555	2532	3498	3200	2201
N_{2tag}	37	1382	22	1270	12	787
CMUP Muons						
N_{btag}	2394	4253	1997	4302	2437	2787
$N_{\mathsf{btag=1}}$	2363	3211	1967	3324	2412	2153
$N_{\mathsf{M}\ell\nu\mathsf{b}}$	1999	2748	1620	2887	2012	1846
N_{jet1}	1954	2661	1580	2809	1953	1795
N_{1tag}	1981	2022	1598	2171	2002	1385
$N_{\mathsf{1tag,ET}}$	1938	1952	1558	2104	1943	1344
N_{2tag}	18	726	22	716	10	461
CMX Muons						
N_{btag}	859	1579	718	1653	861	1135
$N_{\mathsf{btag=1}}$	846	1215	708	1306	857	863
$N_{\mathsf{M}\ell\nu\mathsf{b}}$	723	1050	593	1087	747	770
N_{jet1}	696	1011	579	1049	727	747
N_{1tag}	714	779	585	853	744	564
$N_{\mathsf{1tag,ET}}$	687	747	571	822	724	545
N_{2tag}	9	271	8	234	3	206

Table B.1: Number of Monte Carlo events after event selection in the 2-jets bin.

Monte Carlo Event Detection Efficiency in %						
	MadEvent		TopRex		Pythia	
Sample	t-chan.	s-chan.	t-chan.	s-chan.	t-chan.	s-chan.
CEM Electrons						
ϵ_{btag}	0.834	1.235	0.748	1.177	0.784	1.037
$\epsilon_{\mathsf{btag=1}}$	0.824	0.931	0.738	0.894	0.780	0.800
$\epsilon_{\mathsf{M}\ell\nu\mathsf{b}}$	0.699	0.812	0.613	0.784	0.653	0.688
ϵ_{jet1}	0.676	0.786	0.592	0.760	0.635	0.668
ϵ_{1tag}	0.692	0.591	0.608	0.581	0.651	0.512
$\epsilon_{\mathsf{1tag,ET}}$	0.669	0.570	0.587	0.560	0.633	0.494
ϵ_{2tag}	0.007	0.221	0.005	0.203	0.002	0.177
CMUP Muons						
ϵ_{btag}	0.470	0.681	0.463	0.689	0.488	0.626
$\epsilon_{\mathsf{btag=1}}$	0.464	0.515	0.456	0.532	0.483	0.489
$\epsilon_{\mathsf{M}\ell\nu\mathsf{b}}$	0.392	0.440	0.376	0.462	0.398	0.414
ϵ_{jet1}	0.384	0.426	0.367	0.450	0.386	0.403
ϵ_{1tag}	0.389	0.324	0.371	0.348	0.396	0.311
$\epsilon_{\mathsf{1tag,ET}}$	0.380	0.313	0.361	0.337	0.384	0.302
ϵ_{2tag}	0.004	0.116	0.005	0.115	0.002	0.103
CMX Muons						
ϵ_{btag}	0.169	0.253	0.167	0.265	0.172	0.255
$\epsilon_{\mathsf{btag=1}}$	0.166	0.195	0.164	0.209	0.172	0.196
$\epsilon_{\mathsf{M}\ell\nu\mathsf{b}}$	0.142	0.168	0.138	0.174	0.148	0.173
ϵ_{jet1}	0.137	0.162	0.134	0.168	0.144	0.168
ϵ_{1tag}	0.140	0.125	0.136	0.137	0.147	0.127
$\epsilon_{\mathsf{1tag,ET}}$	0.135	0.120	0.132	0.132	0.143	0.122
ϵ_{2tag}	0.002	0.043	0.002	0.037	0.001	0.046

Table B.2: $\epsilon_{\mathsf{evt}}^{\mathsf{MC}} \cdot \epsilon_{\mathsf{BR}}$ for single top Monte Carlo samples. The statistical error on the efficiencies is 0.01% or less.

B.2 Determination of $\epsilon_{\mathrm{evt}}^{\mathrm{MC}}$ for $t\bar{t}$ Events

	$t\bar{t}$ samples			
Process	ttbar Pythia	Herwig	Herwig, 170	Herwig, 180
ID	ttopei	ttopli	ttoppk	ttopsk
N_{tot}	398037	378471	206958	208000
N_{obsv}	384875	365743	199998	200976
CEM Electrons				
N_{btag}	2197	2074	1151	1150
$N_{\mathsf{btag=1}}$	1784	1667	947	907
$N_{\mathsf{M}\ell\nu\mathsf{b}}$	1020	996	591	513
N_{jet1}	994	969	572	501
N_{1tag}	825	801	478	403
$N_{\mathsf{1tag,ET}}$	801	777	460	393
N_{2tag}	195	195	113	110
CMUP Muons				
N_{btag}	1292	1263	695	706
$N_{\mathsf{btag=1}}$	1028	1023	564	573
$N_{\mathsf{M}\ell\nu\mathsf{b}}$	644	613	356	320
N_{jet1}	627	593	344	314
N_{1tag}	509	496	288	259
$N_{\mathsf{1tag,ET}}$	494	479	277	253
N_{2tag}	135	117	68	61
CMX Muons				
N_{btag}	497	497	252	262
$N_{\mathsf{btag=1}}$	392	398	202	213
$N_{\mathsf{M}\ell\nu\mathsf{b}}$	237	262	126	121
N_{jet1}	233	258	121	118
N_{1tag}	187	207	99	99
$N_{\mathsf{1tag,ET}}$	184	203	94	96
N_{2tag}	50	55	27	22

Table B.3: Number of Monte Carlo events after event selection in the 2-jets bin.

Table B.3 summarizes the number of remaining $t\bar{t}$ events for each considered scenario. Table B.4 list the results of the $\epsilon_{\mathrm{evt}}^{\mathrm{MC}}$ calculation for $t\bar{t}$ events.

Monte Carlo Event Detection Efficiency in %				
	$t\bar{t}$ samples			
Sample	ttbar Pythia	Herwig	Herwig, 170	Herwig, 180
CEM Electrons				
$\epsilon_{\rm btag}$	0.55	0.55	0.56	0.55
$\epsilon_{\rm btag=1}$	0.45	0.44	0.46	0.44
$\epsilon_{\rm M\ell\nu b}$	0.26	0.26	0.29	0.25
$\epsilon_{\rm jet1}$	0.25	0.26	0.28	0.24
$\epsilon_{\rm 1tag}$	0.21	0.21	0.23	0.19
$\epsilon_{\rm 1tag,ET}$	0.20	0.21	0.22	0.19
$\epsilon_{\rm 2tag}$	0.05	0.05	0.05	0.05
CMUP Muons				
$\epsilon_{\rm btag}$	0.32	0.33	0.34	0.34
$\epsilon_{\rm btag=1}$	0.26	0.27	0.27	0.28
$\epsilon_{\rm M\ell\nu b}$	0.16	0.16	0.17	0.15
$\epsilon_{\rm jet1}$	0.16	0.16	0.17	0.15
$\epsilon_{\rm 1tag}$	0.13	0.13	0.14	0.12
$\epsilon_{\rm 1tag,ET}$	0.12	0.13	0.13	0.12
$\epsilon_{\rm 2tag}$	0.03	0.03	0.03	0.03
CMX Muons				
$\epsilon_{\rm btag}$	0.12	0.13	0.12	0.13
$\epsilon_{\rm btag=1}$	0.10	0.11	0.10	0.10
$\epsilon_{\rm M\ell\nu b}$	0.06	0.07	0.06	0.06
$\epsilon_{\rm jet1}$	0.06	0.07	0.06	0.06
$\epsilon_{\rm 1tag}$	0.05	0.05	0.05	0.05
$\epsilon_{\rm 1tag,ET}$	0.05	0.05	0.05	0.05
$\epsilon_{\rm 2tag}$	0.01	0.01	0.01	0.01

Table B.4: $\epsilon_{\rm evt}^{\rm MC} \cdot \epsilon_{\rm BR}$ for $t\bar{t}$ Monte Carlo samples. The statistical error on the efficiencies is 0.01% or less.

B.3 Determination of $\epsilon_{\mathrm{evt}}^{\mathrm{MC}}$ for Diboson Events

Process	WW0p	WZ0p	ZZ0p
ID	atop4x	atop0y	atop0z
N_{tot}	944969	191011	223606
N_{obsv}	913775	184934	216547
CEM Electrons			
N_{btag}	1170	230	29
$N_{\mathsf{btag=1}}$	1164	189	28
$N_{\mathsf{M}\ell\nu\mathsf{b}}$	496	118	12
N_{jet1}	447	107	12
N_{1tag}	494	96	11
$N_{\mathsf{1tag,ET}}$	445	86	11
N_{2tag}	2	22	1
CMUP Muons			
N_{btag}	663	143	53
$N_{\mathsf{btag=1}}$	662	123	43
$N_{\mathsf{M}\ell\nu\mathsf{b}}$	273	63	24
N_{jet1}	256	58	21
N_{1tag}	273	57	17
$N_{\mathsf{1tag,ET}}$	256	52	14
N_{2tag}	1	6	7
CMX Muons			
N_{btag}	307	69	17
$N_{\mathsf{btag=1}}$	304	55	15
$N_{\mathsf{M}\ell\nu\mathsf{b}}$	134	32	8
N_{jet1}	120	28	8
N_{1tag}	132	28	7
$N_{\mathsf{1tag,ET}}$	119	24	7
N_{2tag}	2	4	1

Table B.5: Number of Monte Carlo events after event selection in the 2-jets bin.

Table B.5 summarizes the number of remaining diboson events for each considered scenario. Table B.6 list the results of the $\epsilon_{\mathrm{evt}}^{\mathrm{MC}}$ calculation for diboson events.

Monte Carlo Event Detection Efficiency in %			
Sample	WW0p	WZ0p	ZZ0p
CEM Electrons			
ϵ_{btag}	0.04	0.12	0.01
$\epsilon_{\mathsf{btag=1}}$	0.04	0.10	0.01
$\epsilon_{\mathsf{M}\ell\nu\mathsf{b}}$	0.02	0.06	0.01
ϵ_{jet1}	0.02	0.06	0.01
ϵ_{1tag}	0.02	0.05	0.00
$\epsilon_{\mathsf{1tag,ET}}$	0.02	0.05	0.00
ϵ_{2tag}	0.00	0.01	0.00
CMUP Muons			
ϵ_{btag}	0.02	0.07	0.02
$\epsilon_{\mathsf{btag=1}}$	0.02	0.06	0.02
$\epsilon_{\mathsf{M}\ell\nu\mathsf{b}}$	0.01	0.03	0.01
ϵ_{jet1}	0.01	0.03	0.01
ϵ_{1tag}	0.01	0.03	0.01
$\epsilon_{\mathsf{1tag,ET}}$	0.01	0.03	0.01
ϵ_{2tag}	0.00	0.00	0.00
CMX Muons			
ϵ_{btag}	0.01	0.04	0.01
$\epsilon_{\mathsf{btag=1}}$	0.01	0.03	0.01
$\epsilon_{\mathsf{M}\ell\nu\mathsf{b}}$	0.00	0.02	0.00
ϵ_{jet1}	0.00	0.01	0.00
ϵ_{1tag}	0.00	0.01	0.00
$\epsilon_{\mathsf{1tag,ET}}$	0.00	0.01	0.00
ϵ_{2tag}	0.00	0.00	0.00

Table B.6: $\epsilon_{\rm evt}^{\rm MC} \cdot \epsilon_{\rm BR}$ for diboson Monte Carlo samples. The statistical error on the efficiencies is 0.01% or less.

Bibliography

[1] T. Han, M. Hosch, K. Whisnant, B.-L. Young, and X. Zhang, "Single top quark production via fcnc couplings at hadron colliders," *Phys. Rev.* **D58** (1998) 073008, `hep-ph/9806486`.

[2] S. L. Glashow, "Partial symmetries of weak interactions," *Nucl. Phys.* **22** (1961) 579–588.

[3] S. Weinberg, "A model of leptons," *Phys. Rev. Lett.* **19** (1967) 1264–1266.

[4] A. Salam, "Weak and electromagnetic interactions,". Originally printed in *Svartholm: Elementary Particle Theory, Proceedings Of The Nobel Symposium Held 1968 At Lerum, Sweden*, Stockholm 1968, 367-377.

[5] S. Eidelman *et. al.*, "Review of Particle Physics," *Physics Letters B* **592** (2004) 1+.

[6] **Particle Data Group** Collaboration, K. Hagiwara *et. al.*, "Review of particle physics," *Phys. Rev.* **D66** (2002) 010001.

[7] M. Kobayashi and T. Maskawa, "CP Violation in the Renormalizable Theory of Weak Interaction," *Prog. Theor. Phys.* **49** (1973) 652–657.

[8] N. Cabbibo, "Unitary symmetry and leptonic decays," *Phys. Rev. Lett.* **10** (1963) 531–533.

[9] P. W. Higgs, "Broken symmetries and the masses of gauge bosons," *Phys. Rev. Lett.* **13** (1964) 508–509.

[10] **CDF** Collaboration, F. Abe *et. al.*, "Evidence for top quark production in $\bar{p}p$ collisions at $\sqrt{s} = 1.8$ TeV," *Phys. Rev.* **D50** (1994) 2966–3026.

[11] **D0** Collaboration, S. Abachi *et. al.*, "Observation of the top quark," *Phys. Rev. Lett.* **74** (1995) 2632–2637, `hep-ex/9503003`.

[12] **CDF** Collaboration, F. Abe *et. al.*, "Observation of top quark production in $\bar{p}p$ collisions," *Phys. Rev. Lett.* **74** (1995) 2626–2631, `hep-ex/9503002`.

[13] N. Kidonakis and R. Vogt, "Next-to-next-to-leading order soft-gluon corrections in top quark hadroproduction," *Phys. Rev.* **D68** (2003) 114014, hep-ph/0308222.

[14] M. Cacciari, S. Frixione, M. L. Mangano, P. Nason, and G. Ridolfi, "The t anti-t cross-section at 1.8-tev and 1.96-tev: A study of the systematics due to parton densities and scale dependence," *JHEP* **04** (2004) 068, hep-ph/0303085.

[15] J. Pumplin *et. al.*, "New generation of parton distributions with uncertainties from global qcd analysis," *JHEP* **07** (2002) 012, hep-ph/0201195.

[16] T. Stelzer, Z. Sullivan, and S. Willenbrock, "Single top quark production at hadron colliders," *Phys. Rev.* **D58** (1998) 094021, hep-ph/9807340.

[17] Z. Sullivan, "Understanding single-top-quark production and jets at hadron colliders," *Phys. Rev.* **D70** (2004) 114012, hep-ph/0408049.

[18] B. W. Harris, E. Laenen, L. Phaf, Z. Sullivan, and S. Weinzierl, "The fully differential single top quark cross section in next-to-leading order QCD," *Phys. Rev.* **D66** (2002) 054024, hep-ph/0207055.

[19] D. O. Carlson and C. P. Yuan, "Studying the top quark via the w - gluon fusion process," *Phys. Lett.* **B306** (1993) 386–390.

[20] A. P. Heinson, A. S. Belyaev, and E. E. Boos, "Single top quarks at the fermilab tevatron," *Phys. Rev.* **D56** (1997) 3114–3128, hep-ph/9612424.

[21] **D0** Collaboration, B. Abbott *et. al.*, "Search for electroweak production of single top quarks in p anti-p collisions," *Phys. Rev.* **D63** (2001) 031101, hep-ex/0008024.

[22] **D0** Collaboration, V. M. Abazov *et. al.*, "Search for single top quark production at d0 using neural networks," *Phys. Lett.* **B517** (2001) 282–294, hep-ex/0106059.

[23] **CDF** Collaboration, D. Acosta *et. al.*, "Search for single top quark production in p anti-p collisions at s**(1/2) = 1.8-tev," *Phys. Rev.* **D65** (2002) 091102, hep-ex/0110067.

[24] **CDF** Collaboration, D. Acosta *et. al.*, "Optimized search for single top quark production at the fermilab tevatron," *Phys. Rev.* **D69** (2004) 052003.

[25] P. H. Garbincius, "Tevatron collider operations and plans," hep-ex/0406013.

[26] Fermilab Beams Division, "Run II Handbook,". http://www-bd.fnal.gov/runII/index.html.

[27] **CDF-II** Collaboration, R. Blair *et. al.*, "The CDF-II detector: Technical design report,". FERMILAB-PUB-96-390-E.

[28] **CDF** Collaboration, F. Abe *et. al.*, "The CDF Detector: An Overview," *Nucl. Instr. Meth.* **A271** (1988) 387–403.

[29] **CDF** Collaboration, F. Abe *et. al.*, "Measurement of the W-boson mass," *Phys. Rev.* **D52** (1995) 4784–4827.

[30] **CDF-II** Collaboration, F. Abe *et. al.*, "Proposal for Enhancement of the CDF II Detector: An Inner Silicon Layer and A Time of Flight Detector,". FERMILAB-PROPOSAL-909.

[31] **CDF** Collaboration, T. K. Nelson, "The CDF-II silicon tracking system," *Nucl. Instrum. Meth.* **A485** (2002) 1–5.

[32] S. Cihangir *et. al.*, "SVX': The New CDF silicon vertex detector," *Nucl. Instrum. Meth.* **A360** (1995) 137–140.

[33] F.Hartmann and Th.Müller and M.Schilling and A.Heiss and D.Knoblauch and H.Wenzel, "Evaluation of the ISL prototype detectors,". CDF Note-4627.

[34] **CDF** Collaboration, D. Acosta *et. al.*, "Measurement of the j/psi meson and b-hadron production cross sections in p anti-p collisions at s**(1/2) = 1960- gev," *Phys. Rev.* **D71** (2005) 032001, `hep-ex/0412071`.

[35] **CDF** Collaboration, K. Burkett, "Design and construction of the CDF central outer tracker," *Nucl. Instrum. Meth.* **A461** (2001) 62–64.

[36] **CDF** Collaboration, M. G. Albrow *et. al.*, "The CDF plug upgrade electromagnetic calorimeter: Test beam results," *Nucl. Instrum. Meth.* **A480** (2002) 524–546.

[37] E. J. Thomson *et. al.*, "Online track processor for the cdf upgrade," *IEEE Trans. Nucl. Sci.* **49** (2002) 1063–1070.

[38] **CDF** Collaboration, H. Wenzel *et. al.*, "Online Monitoring and Module Maintenance for CDF in the upcoming Fermilab Tevatron Run II," in *Computing in High Energy and Nuclear Physics (CHEP 2000)*, pp. 335–340. 2000.

[39] H. Stadie, "CDF Online Monitoring." Talk at *ROOT2001 International HENP ROOT Users Workshop*, http://www-root.fnal.gov/root2001/presentations/session5/consumer.pdf.

[40] **CDF** Collaboration, K. Maeshima *et. al.*, "Online Monitoring for the CDF Run II Experiment," in *2003 Conference for Computing in High-Energy and Nuclear Physics (CHEP 03)*. 2003.

[41] R. Brun and F. Rademakers. Root system homepage http://root.cern.ch.

[42] **CDF** Collaboration, J. Antos *et. al.*, "The CDF Run 2 offline computer farms," in *CHEP'01: Computing In High-Energy and Nuclear Physics*, pp. 53–56. 2001.

[43] H. Wenzel, "Tracking in the SVX,". CDF Note-1790.

[44] A. Mukherjee, "CTC and VTX Tracking,". CDF Note-5490.

[45] P. Azzi, G. Busetto, P. Gatti, and A. Ribon, "Histogram Tracking in the COT,". CDF Note-5562.

[46] K. Bloom and W.-M. Yao, ""Outside-In" Silicon Tracking at CDF,". CDF Note-5991.

[47] S. Menzemer, *Spurrekonstruktion im Silizium-Vertexdetektor des CDF-II-Experiments*. PhD thesis, Institut für Experimentelle Kernphysik, Universität Karlsruhe, 2003.

[48] F. Bedeschi *et. al.*, "A Primary Vertex Finding Package,". CDF Note-1789.

[49] H. Stadie *et. al.*, "The Beam Position in Run II,". CDF Note-6327.

[50] Run II Alignment group http://www-cdf.fnal.gov/internal/upgrades/align/alignment.html.

[51] M. Martens and P. Bagley, "Luminosity Distribution During Collider Run II,". http://www-ap.fnal.gov/∼martens/luminosity/beam_size.html.

[52] H. Wenzel, "The Primary Interaction Vertex,". CDF Note-4066.

[53] S. Lai *et. al.*, "An Updated Measurement of the Beam Width at CDF,". CDF Note-6492.

[54] S. Lai *et. al.*, "An Evaluation of the Beam With at CDF,". CDF Note-6311.

[55] W. Wagner, "An Estimate of the Average Beam With at CDF,". CDF Note-6104.

[56] G. C. Blazey *et. al.*, "Run II jet physics," in *Physics at Run II: QCD and Weak Boson Physics Workshop*, pp. 47–77. 1999. `hep-ex/0005012`.

[57] **D0** Collaboration, V. M. Abazov *et. al.*, "The inclusive jet cross-section in p anti-p collisions at s**(1/2) = 1.8-tev using the k(t) algorithm," *Phys. Lett.* **B525** (2002) 211–218, hep-ex/0109041.

[58] J.-F. Arguin *et. al.*, "Generic Jet Energy Corrections for Run II,". CDF Note-6280.

[59] **CDF** Collaboration, T. Affolder *et. al.*, "Measurement of the t anti-t production cross section in p anti-p collisions at s**(1/2) = 1.8-tev," *Phys. Rev.* **D64** (2001) 032002, hep-ex/0101036.

[60] **CDF** Collaboration, D. Acosta *et. al.*, "Measurement of the t anti-t production cross section in p anti-p collisions at s**(1/2) = 1.96-tev using lepton + jets events with secondary vertex b-tagging," hep-ex/0410041.

[61] R. Brun and F. Carminati, "Cern programming library, long writeup,". W5013.

[62] **CDF** Collaboration, T. Affolder *et. al.*, "Cdf central outer tracker," *Nucl. Instrum. Meth.* **A526** (2004) 249–299.

[63] G. Grindhammer, M. Rudowicz, and S. Peters, "The fast simulation of electromagnetic and hadronic showers," *Nucl. Instrum. Meth.* **A290** (1990) 469.

[64] E. Gerchtein and M. Paulini, "Cdf detector simulation framework and performance," *ECONF* **C0303241** (2003) TUMT005, physics/0306031.

[65] S. Klimenko, J. Konigsberg, and T. Liss, "Averaging of the inelastic cross-section measured by the CDF and the E811 experiments,". CDF Note-6314.

[66] F. Maltoni and T. Stelzer, "Madevent: Automatic event generation with madgraph," *JHEP* **02** (2003) 027, hep-ph/0208156.

[67] T. Sjostrand, L. Lonnblad, and S. Mrenna, "Pythia 6.2: Physics and manual," hep-ph/0108264.

[68] S. R. Slabospitsky and L. Sonnenschein, "Toprex generator (version 3.25): Short manual," *Comput. Phys. Commun.* **148** (2002) 87–102, hep-ph/0201292.

[69] E. T. *et al.*, "Top and electroweak event classification module for cdf run ii,". CDF Note-5947.

[70] C. C. *et al.*, "MadEvent Signal Samples used in the Run II Single Top Search,". CDF Note-7020.

[71] H. B. *et al.*, "$t\bar{t}$ Event Selection and Detection Efficiency for Winter 2003 Lepton + Jets Analyses,". CDF Note-6084.

[72] A. Taffard, "Run II Cosmic Ray Tagger Performances,". CDF Note-6255.

[73] L. T. Y.-K. Kim, J. Nielsen and G. Veramendi, "Trigger Efficiencies for High P_T Electrons,". CDF Note-6234.

[74] S. L. M. Coca, E. Halkiadakis, "Central Electron Identification Efficiencies for the 200$\mathbf{pb^{-}1}$ Run 2 Dataset,". CDF Note-6580.

[75] V. Martin and L. Cerrito, "Muon Cuts and Efficiencies for 4.11 Analyses,". CDF Note-6825.

[76] W. Sakumoto and A. Hocker, "Event $|Z_{vtx}| \leq 60$ cm Cut Efficiency for Run II,". CDF Note-6331.

[77] T. W. H. Bachacou, W. Yao, "Efficiency of SecVtx B-Tag Used for 2004 Winter Conferences,". CDF Note-6904.

[78] D. A. et al., "Measurement of the $p\bar{p} \rightarrow t\bar{t}$ cross section in the ℓ+jets SECVTX tagged sample,". CDF Note-6329.

[79] P. Nason, S. Dawson, and R. K. Ellis, "The one particle inclusive differential cross-section for heavy quark production in hadronic collisions," *Nucl. Phys.* **B327** (1989) 49–92.

[80] W. Beenakker, H. Kuijf, W. L. van Neerven, and J. Smith, "Qcd corrections to heavy quark production in p anti-p collisions," *Phys. Rev.* **D40** (1989) 54–82.

[81] E. L. Berger and H. Contopanagos, "Threshold resummation of the total cross section for heavy quark production in hadronic collisions," *Phys. Rev.* **D57** (1998) 253–264, `hep-ph/9706206`.

[82] R. Bonciani, S. Catani, M. L. Mangano, and P. Nason, "Nll resummation of the heavy-quark hadroproduction cross- section," *Nucl. Phys.* **B529** (1998) 424–450, `hep-ph/9801375`.

[83] J. M. Campbell and R. K. Ellis, "An update on vector boson pair production at hadron colliders," *Phys. Rev.* **D60** (1999) 113006, `hep-ph/9905386`.

[84] J. N. H. Bachacou and W.-M. Yao, "Optimized Measurement of the $t\bar{t}$ Production Cross Section in the SECVTX Tagged Sample,". CDF Note-6902.

[85] V. Blobel and E. Lohrmann, "Statistische und numerische Methoden der Datenanalyse,". ISBN 3-519-03243-0, B.G. Teubner.

[86] C. Ciobanu *et. al.*, "Likelihood Function for Single Top Search with 162 pb^{-1},". CDF Note-7106.

[87] R. Fisher, "The Use of Multiple Measurements in Taxonomic Problems," *Annals of Eugenics* **7** (1936) 179–188.

[88] T. G. M. Malmgren and K. E. Johansson, "An iterative discriminant analysis method to search for the higgs particle at lep-2," *Nucl. Instrum. Meth.* **A403** (1998) 481–489.

[89] **CDF** Collaboration, D. Acosta *et. al.*, "Search for electroweak single top quark production in p anti-p collisions at s**(1/2) = 1.96-tev," *Phys. Rev.* **D71** (2005) 012005, `hep-ex/0410058`.

[90] J.-F. A. *et al.*, "Systematic Uncertainties Associated with Jet Corrections for Winter 2003 Conferences,". CDF Note-6419.

[91] S. Budd *et. al.*, "A Multivariate Likelihood Search for Single Top,". CDF Note-7493.

Acknowledgements

I wish to sincerely thank my supervisor Prof. Dr. Thomas Müller for his support and guidance throughout the time I spent at the *Institut für Experimentelle Kernphysik* and Prof. Dr. Michael Feindt for co-supervising this thesis.

I thank Dr. Wolfgang Wagner his support and advice throughout the years I spent in Karlsruhe and Chicago. I really enjoyed working with him on single top. Thanks for carefully reading this manuscript and for the encouraging atmosphere in our office.

This thesis would has been impossible without the assistance of the members of the *Institut für Experimentelle Kernphysik* in Karlsruhe and the members of the CDF Collaboration in Chicago. I wish to thank my fellow graduate student colleges for all the discussions about physics and beyond. It was really a great time I had here.

Support for this work was provided by the Land Baden-Württemberg and the "Graduiertenkolleg Hochenergie und Teilchenastrophysik" by graduate scholarships.

I wish to thank my friends for enduring my pessimism and my blue moods.

Finally I wish to thank my family for supporting me over all those years.